MEASURING AND MODELING THE LONG-TERM SENSITIZATION BEHAVIOR OF Al 5XXX ALLOYS

by

Gaosong Yi

A dissertation submitted to the faculty of
The University of Utah
in partial fulfillment of the requirements for the degree of

Doctor of Philosophy

Department of Metallurgical Engineering

The University of Utah

May 2017

The University of Utah Graduate School

STATEMENT OF DISSERTATION APPROVAL

The dissertation of **Gaosong Yi**

has been approved by the following supervisory committee members:

Michael L. Free	, Chair	**11/02/2016** Date Approved
Zhigang Zak Fang	, Member	**11/02/2016** Date Approved
Michael Simpson	, Member	**11/02/2016** Date Approved
David Cullen	, Member	**11/02/2016** Date Approved
Ryan Steele	, Member	**11/02/2016** Date Approved

and by **Manoranjan Misra** , Chair/Dean of

the Department/College/School of **Metallurgical Engineering**

and by David B. Kieda, Dean of The Graduate School.

ABSTRACT

Al 5xxx alloys are widely used in marine and offshore structures for their excellent balance of weight, strength, ductility, weldability, and corrosion resistance. However, they can become sensitized when exposed to elevated temperature for a long time, which is caused by the precipitation of intergranular β phase. β phase is anodic to Al matrix and can be selectively dissolved by corrosive solutions, such as sea water, and cause intergranular corrosion and stress corrosion cracking.

In the present study, Al 5xxx alloys (Al 5083, Al 5456, Al 5050, Al 5052, and Al 5154) were aged at constant temperatures (40, 50, 60, 70°C) and cyclic temperatures (40-45, 30-70, 50-70°C) for as long as 57.5 months. The microstructure was investigated using electron backscatter diffraction (EBSD), scanning transmission electron microscopy (STEM), energy-dispersive X-ray spectroscopy (EDS), atom probe tomography (APT), and small angle neutron scattering (SANS). Experimental results reveal that a phase transformation process from GP zones to β'/β phases occurs for precipitates formed in both Al 5083 H131 and H116 aged at 70°C. The size of intergranular and intragranular β phase increase with aging time.

In addition, a model based on local equilibrium of chemical potential and multiclass precipitates number evolution was adopted to predict the multiphase precipitation process in the Al-Mg binary system. The overall trend of precipitate radius and number density predicted by the model match well with experimental results. Moreover, the particle size

distribution (PSD) of different Mg-rich precipitates demonstrates their different stages of precipitation.

A classical nucleation-growth-coarsening theory for the description of intergranular precipitation is formulated, which adopts a collector plate mechanism, an equivalent average Mg concentration at the grain boundary, and a new coarsening expression. Three coarsening mechanisms, the modified LSW (Lifschitz-Slyozov-Wagner), the Kirchner mechanism, and a combination of these two mechanisms, are compared. Modeling results reveal that the Kirchner mechanism will break down when continuity ($\sqrt{N\pi R^2}$) is close to 1. According to the new model, the coarsening mechanism still accounts for a small fraction (only 10%) in the final growth rate after aging at 70℃ for 40 months, which is confirmed by the precipitate size distribution data. Thickness and continuity results predicted by the new model agree well with experimental results obtained from scanning transmission electron microscopy (STEM) images of Al 5083 H131 alloys aged at 70℃ for different times. In addition, the new model is also applied to a high-temperature 180℃ situation, where precipitate coarsening is observed.

ASTM G-67 Nitric Acid Mass Loss Test (NAMLT) results of Al 5050 H32, 5052 H32, 5154 H32, 5083 H116, 5083 H131, and 5456 H116 alloys were obtained to evaluate the Degree of Sensitization (DoS). A linear relationship between continuity and mass loss was adopted to predict the mass loss of Al 5083 H116 and H131 aged at constant and cyclical temperature, and the modeling results agree well with experimental mass loss data.

TABLE OF CONTENTS

LIST OF TABLES

LIST OF FIGURES

ACKNOWLEDGEMENTS

The work presented in this dissertation was conducted in the Department of Metallurgical Engineering, The University of Utah, under the supervision of Dr. Michael L. Free. The author is very grateful to the Office of Naval Research for providing the funding.

First of all, I would like to express my sincere gratitude to my advisor, Dr. Michael L. Free, for providing me the opportunity to work on this wonderful project. I am thankful to him for his great guidance, fruitful discussions, and valuable suggestions which helped a lot to solve the academic problems encountered during the research. Moreover, thanks to him for teaching me how to be a nice person in the past four years, and I could not have imagined having a better advisor and mentor for my Ph.D study.

I would like to express my gratitude to Dr. David Cullen, Dr. Zhigang (Zak) Fang, Dr. Michael Simpson, and Dr. Ryan P. Steele for their valuable guidance and helpful suggestions on different aspects of my research work.

Thanks for the help of my lab mates Dr. Soumya Kar, Dr. Yakun Zhu, Alexander Derrick, and Erik Sundberg, who have been working on this project together with me.

Microscopy results of this research were conducted at the Center for Nanophase Materials Sciences, which is a DOE Office of Science User Facility. This work utilizes the Oak Ridge National Laboratory's High Flux Isotope Reactor, which is sponsored by the

Scientific User Facilities Division, Office of Basic Energy Sciences, U.S. Department of Energy. APT was conducted at ORNL's Center for Nanophase Materials Sciences (CNMS), which is a U.S. DOE Office of Science User Facility. This work made use of University of Utah USTAR shared facilities support, in part, by the MRSEC Program of NSF under Award No. DMR-1121252. Great thanks should be extended to Dr. David Cullen, Dr. Jonathan D Poplawsky, and Dr. Ken Littrell for their help on STEM, APT, and SANS experiments as well as the subsequent data processing.

Thanks to Dr. Brian van Devener, Paulo Perez, and Randy Polson at The University of Utah, and Dr. Jeff Farrer and Paul Minson at Brigham Young University for their support and discussion on TEM sample preparation and imaging work

Thanks also to everyone in Dr. Free's research group for their help, encouragement, and discussions during my Ph.D study.

Last but not least, thanks to my parents, sisters, girlfriend, and some other family members for the love, encouragement, and support during the past years.

CHAPTER 1

INTRODUCTION

Al 5xxx alloys, such as Al 5083 and Al 5456, have a good combination of strength, ductility, weldability, and corrosion resistance, therefore they have been increasingly used for structures of vehicles and ships throughout the United States Navy. [1,2] In addition, they are also widely used for the commercial ship and automobile manufacturing industries, because the replacement of steel using Al alloys decreases the weight of structures, thereby increasing speed, range, and fuel economy.[3]

The precipitation of a second phase is widely used in some Al alloys (like Al 6xxx [4] and 7xxx [5] alloys) to enhance their mechanical properties [6,7] such as strength, hardness, and creep resistance. However, the appearance of the second phase can also result in detrimental effects to the performance of the alloy. For instance, the intergranular corrosion (IGC) and stress corrosion cracking (SCC) [8–10] of Al 5xxx alloy caused by the precipitation of β phase (Al_3Mg_2) at grain boundaries.[11] According to previous research, Al alloys containing more than 3 wt.% Mg can become unstable with time at moderately elevated service temperature due to the precipitation of Mg-rich β phase (Al_3Mg_2) at grain boundaries.[12] β phase has a corrosion potential of around -1.29V (SCE), and it is anodic to Al matrix, which has a corrosion potential of -0.73V (SCE).[13] Therefore, intergranular

β phase will be selectively dissolved when exposed to corrosive environments, such as sea water. [8,11]

A substantial volume of research has been conducted on the precipitation behavior of Al-Mg alloys. For example, Searles *et al*. aged Al 5083 alloy at 150℃ for different times, and their results indicated that the fractional coverage of β phase increased with aging time when aging time was shorter than 189 hours.[8,14] While the thin β phase film started to coarsen and became discontinuous if aging time was longer than 189 hours. Goswami *et al*. investigated Al 5083 H131 alloy aged at 175℃ for 10 days, and β phase was observed on pre-existing Al_6Mn-type pre-existing particles. [15] In addition, pipe diffusion through dislocations was applied to explain the fast growth of intergranular β phase. Sato and Kamio characterized precipitates formed in Al-14 wt.% Mg alloy aged at different temperatures (from room temperature to 90℃), and they found that GP zones and β" (Al_3Mg) phase cannot form in the matrix when aging temperature is higher than 90 ℃. [16] However, these studies were conducted either at high temperatures (>100℃) or for Al-Mg alloys of high Mg concentrations (>10 wt.% Mg), which is very different from the real exposure environment of Navy ships and the normal compositional range of Al 5xxx alloys.

In the present study, Al 5xxx alloys (Al 5083 H131, H116, H321, and Al 5456 H116) were aged at low constant temperatures (40, 50, 60, and 70℃) as well as cyclic temperatures (30-45, 30-70, 30-45, and 30-50℃) which were selected based on the real temperature profiles measured from samples on the deck of a US navy ship traveling from San Diego to Panama City through the Panama Canal.[17] Moreover, the aging time for some of the samples is as long as 4.5 years. The objectives of this study are listed as follows:

(1) Characterize the sensitized samples using instruments, such as scanning transmission electron microscopy, energy dispersed X-ray spectroscopy, atom probe tomography, and small angle neutron scattering, to identify the type of different Mg-rich precipitates as well as their size and volume fraction;

(2) Develop an intergranular β phase precipitation model to predict the nucleation, growth, and coarsening of β phase formed in Al 5xxx alloys aged at different temperatures;

(3) Conduct intergranular corrosion tests for Al 5xxx alloys (Al 5083 H131, H116, H321 and Al 5456 H116) aged at different temperatures for different times to estimate their sensitization degrees;

(4) Correlate the distribution of intergranular β phase (the continuity) with the ASTM G67 mass loss, and propose a primary model to predict the mass loss of Al 5xxx alloys aged at different temperatures for different times.

CHAPTER 2

LITERATURE REVIEW

2.1 Introduction

Aluminum is the most-used nonferrous metal, with an annual consumption of 25 million tons. [18] The wide application of Al and Al alloys can be attributed to their advantageous properties, such as lightness, thermal conductivity, electrical conductivity, suitability for surface treatments, corrosion resistance, diversity of semiproducts, functional advantages of extruded and cast semiproducts, and ease of recycling. [18]

2.2 Classification of Al alloys

Al alloys are usually divided into two major categories: wrought Al alloy and casting Al alloy. Wrought Al alloy indicates alloys produced in ingot or billet form and further processed by techniques such as rolling, extruding, forging, drawing, or other metalworking to produce semiproducts. Casting Al alloys refers to alloys that are used in parts cast to final or near-final shape, and no further working or processing is needed. [19]

2.2.1 Wrought Al alloys

For wrought alloys, the Aluminum Association has a four-digit system to identify different families. The first digit defines the major alloy element, the second digit defines variations in the original basic alloy, and the third and fourth digits designate the specific alloy within the series. [19] The detail classification [20] of wrought Al alloys are shown as follows:

- 1xxx series alloys are unalloyed (pure) Al with a composition of Al≥99%, and the primary application of 1xxx alloys is in the electrical and chemical industries.
- 2xxx series alloys are based on copper as the main alloy element, and notably, magnesium is also added. 2xxx alloys are widely used in aircraft-related industries.
- 3xxx series alloys have manganese as the principal alloy element, and the general application of this alloy is architecture.
- 4xxx series alloys have silicon as the main alloy element, and they are widely used for welding rods and brazing sheets.
- 5xxx series alloys have magnesium as the principal alloy element, and are used in boat hulls, gangplanks, and other products exposed to marine environments.
- 6xxx series alloys have magnesium and silicon as the principal elements, which are widely used in architectural extrusions.
- 7xxx series alloys are based on zinc, and some other elements such as copper, magnesium, chromium, and zirconium may be added. 7xxx alloys are used for aircraft structural components and other high-strength applications.
- 8xxx series alloys includes tin, iron, and lithium compositions, which are less frequently used.

Among the above alloys, 2xxx, 6xxx, and 7xxx series are heat-treatable Al alloys, which can be strengthened by heating and then quenching, or rapid cooling; while 1xxx, 3xxx, 4xxx, and 5xxx series alloys are non-heat-treatable Al alloys, and hardening effects of these alloys are induced by their alloy elements. Moreover, further strengthening of non-heat-treatable alloy can be achieved by cold working. [19]

2.2.1 Al 5xxx alloys

Table 2.1 displays the composition of Al 5083 and Al 5456 alloys. [19,21] The addition of Mg to Al markedly increases the strength of Al without reducing the ductility. Mn plays the same role as Mg. As a matter of fact, increasing amounts of either Mg or Mn intensify the difficulty of fabrication and increase the tendency towards cracking during hot rolling, and the presence of trace Na will further intensify the effect. [19] The addition of Mn works in two different ways: (1) it makes the precipitation of Mg phase more general throughout the structure; (2) it reduces the amount of Mg addition needed to achieve the same amount of strength, which will in turn ensure the stability of the system. [19] Al 5xxx alloys are exceptionally tough and can absorb a lot of energy during fracture. Moreover, Al 5xxx alloys are readily welded by commercial procedures. [20]

Al 5xxx alloys are widely used in offshore structures, warships, and marine platforms for their high corrosion resistance; [1] whereas, Al 5xxx alloys of Mg concentration higher than 3% are not recommended for service in which prolonged elevated temperature may be encountered, because of the decomposition of Al-Mg supersaturated solutions and the formation of anodic phases at the grain boundary, which leads to intergranular corrosion and stress corrosion cracking. [11,14]

2.2.3 Different tempers of Al 5xxx alloys

The basic tempers for Al alloys [20] are classified as follow:

- **F**, as-fabricated, which means no special control over thermal conditions and strain-hardening processes employed to achieve specific properties.
- **O**, annealed, applied to wrought Al alloys that are annealed to obtain the lower strength temper for further workability.
- **H**, strain-hardened, for wrought product only, and products strengthened by strain hardening, with or without supplementary thermal treatment to produce some reduction in strength.
- **W**, solution heat-treated, applied to alloys that age spontaneously at room temperature over a duration of months or years after solution heat-treatment.
- **T**, solution heat-treated, applied to alloys decomposed within a few weeks after solution heat treatment.

Al 5xxx alloys are strength-hardened alloys, and H tempers are used for these alloys. The first number following the letter (H) indicates the specific sequence of basic operations: (1) H1 means strain-hardened only, and no supplementary thermal treatments were applied to the alloys; (2) H2 means strain-hardened and partially annealed, and this applied to products that are strain-hardened more than the desired amount, and the final amount was achieved by partial annealing; (3) H3 means strain-hardened and stabilized, which applied to alloys that strain hardened and whose mechanical properties are stabilized by a low-temperature thermal treatment. The second digit after H stands for the degree of strain hardening. The numeral 8 indicates tempers with ultimate tensile strength equivalent to that achieved by about 75% cold reduction following full annealing. And numerals 1 to 7

stand for tempers between 0 and 8. [20] The temper 9 designates a temper whose minimum ultimate tensile strength is 10 MPa or more, higher than that of the temper 8. The correspondence mechanical properties of Al 5083 and Al 5456 alloys are listed in Table. 2.2. [19]

2.3 Al-Mg binary phase diagram

In Al 5xxx alloy, the principal alloy element is Mg, and the precipitates formed at the grain boundary are Mg-rich precipitates. Thus, it is necessary to refer to the binary Al-Mg phase diagram, which provides the information on saturated Mg concentration at different temperatures. Fig. 2.1 shows the phase diagram of the Al-Mg binary system based on experimental results and calculations. [22] In the present study, Al 5083 and Al 5456 alloys are investigated, and Mg concentration of these two alloys are listed in Table 2.1. Fig. 2.1 reveals that, at 100℃, the saturated concentration of Mg within the matrix is around 1.5 wt.%, which is much lower than the Mg concentration in Al 5083 and Al 5456 alloys. Henceforth, when exposed to elevated temperature for a long time, extra Mg will diffuse out of the matrix and preferentially nucleate at heterogeneous sites such as dislocations, pre-existing particles, and grain boundaries.[15,23] The equilibrium form of Mg-rich precipitates at low temperature (lower than 400℃) is β phase, which has a stoichiometry of Al_3Mg_2, [24] while metastable phases of β will form before the precipitation of β phase, which will be discussed in the next section.

2.4 Precipitation of β phase in Al-Mg alloy

2.4.1 Precipitation sequences in Al-Mg alloy

The decomposition of Al-Mg binary alloy has been investigated by many research groups. Small angle neutron scattering (SANS) is a powerful technique to provide information such as size and number density of precipitates in a bulk sample of centimeter scale [25]. Roth and Raynal [26] aged two types of Al-Mg (7% and 11.5% Mg) alloys at different temperatures (room temperature for 1 year and 40℃ for 3 months plus room temperature for 9 months). SANS results of these samples indicated that Mg-rich (20-25%) zones are able to form in Al-11.5% Mg alloys. Further research [27] by the same authors revealed that GP zones of 19Å in radius were identified in the Al-11.5% Mg alloy aged at 0℃ for 9 months, and Mg concentration in the GP zone was estimated to be 19%. Gault *et al*.[28] investigated the precipitation in polycrystalline and single-crystalline Al-Mg alloys by means of ultrasonic velocity testing, and their results revealed that the formation of GP zones in low temperatures caused an increase of ultrasonic velocities. In contrast, the β' and β phase formed at high temperatures decrease the ultrasonic velocities. Moreover, TEM and ultrasonic measurements indicated that two modes of GP zone exist. A calorimetric study was conducted by Nozato and Ishihara [29] to examine the precipitation process in Al-Mg (7.6-12.5 at.%) alloys, and a four-stage precipitation process was proposed to explain the specific heat versus temperature results below 50℃. The temperature limits for the formation of GP zones and β" phase can be affected by the concentration of Mg. [29] GP zones were reported to form in the as-quenched Al-10.5 at.% Mg alloy annealed at 450℃. In addition, the formation of β' and β phase was associated with a micro hardness change during the aging process. [29]

Kojima *et al.*[30] investigated Al-10 %Mg casting alloys aged in a natural environment for more than 13 years. Their results revealed that the elongation of the solution treated (430℃ for 10 hours and 490℃ for 8 hours) sample is more than 20%, while the elongation of the natural aged sample (room temperature for 13 years) decreased to only 1-2 % due to the precipitation of Mg-rich precipitate. TEM results indicated that the formation of GP zones will cause Ashby-Brown contrast, and the size of GP zones is around 10 nm. The structure of GP zones, (which turns out to be *β*" phase) is $L1_2$, with Al and Mg atoms alternatively aligning in three-dimensional periodicity along the [100] direction. After heating at 150℃ for 500 s, GP zones are reverted completely. Al-Mg alloys (5 wt.% and 10 wt.%) were aged at temperature ranges from -30 to 100℃ by Sato *et al*., [31] and the aged samples were investigated using mechanical tests, electrical resistivity measurements, and high-resolution TEM. An apparent increase in micro hardness was observed in the Al-10wt.% Mg alloy sample, while no change in micro hardness occurred to the Al-5wt.% Mg alloy sample. Both alloys showed an increase in electrical resistivity at the beginning of aging. TEM results demonstrate that GP zone of modulated structure developed into GP zones having the $L1_2$ structure in Al-10wt.% Mg alloy. No GP zones were found in the Al-5wt.% Mg alloy. The limit temperature for GP zone formation was reported to be 25 and 46℃ for Al-5wt.% Mg and Al-10wt.% Mg alloy, respectively, based on electrical resistivity measurements.

Osamura and Ogura [32] aged three types of Al-Mg (5.1at.%, 10.8at.%, and 14.8at.% Mg) alloy at different temperatures (from 30℃ to 180℃), and electrical resistivity measurements and differential scanning calorimetric (DSC) measurements were conducted to investigate the precipitation behavior of Mg-rich precipitate. Based on their research,

GP zones were believed to form at the early stage of aging, while β" phase grew remarkably fast at the late stage of aging. In addition, they proposed a metastable phase diagram for the Al-Mg binary system aged at low temperatures. Sato and Kamio [16] investigated Al-Mg alloys (10wt.%, 14wt.%, 20.1at.%, and 30at.% Mg) aged at different temperatures (room temperature, 60, 80, and 90℃) for as long as 153 months, and their DSC and HRTEM results confirm the presence of GP zones and β" phase. From the results of these studies, the equilibrium precipitation sequence [32] in Al-Mg alloy is established as first, the supersaturated solid solution-GP zone- β"- β'- β phase, where GP zones (short-range ordered Al_3Mg) have a modulated structure [31] under the TEM, and they have the same structure as the Al matrix. However, the Mg concentration in GP zones is much higher than that of the matrix. β" phase (short-range ordered Al_3Mg, a=0.408 nm) has an $L1_2$ structure in which Al and Mg atoms are alternatively aligned along the [100] directions. [32] The superlattice reflections of the ordered structure in the selected area diffraction pattern (SADP) make it very easy to identify, as shown in Fig. 2.2. [33] β' phase, Al_3Mg_2, is reported to have a hexagonal (a=1.002nm, c=1.636 nm) structure and is semicoherent with the matrix. [34] As shown in Fig. 2.3, the shape of β' phase turns out to be needle-like or rod-like, with size ranging from a few hundred nanometer to several microns , and it lies along the <110> direction. The equilibrium β phase, Al_3Mg_2, is of fcc structure (a=2.824nm) with a unit cell containing 1186 atoms. [35] Fig. 2.4 displays a rod-like β phase formed in Al 5083 alloy, and the corresponding SADP is also provided. [36] However, the precipitation sequence can be slightly changed if aging temperature or Mg content is different. Nozato and Ishihara [29] reported that GP zone and β" will not form in the matrix if the aging temperature is higher than 90℃. Sato and Kamio [16] found that β" phase will form directly

in the matrix of Al-Mg alloy of Mg content higher than 20 at.%, which is consistent with the results of Osamura and Ogura [32].

2.4.2 Precipitation at the grain boundary of Al 5083 alloy

Because of the critical role in intergranular corrosion (IGC), intergranular β phase in Al 5xxx alloys has been extensively characterized and modeled. Goswami *et al.* [36] aged Al 5083 alloy sample at 175℃ for 10 days, and β phase particle of thickness 50-190nm were observed to form at the grain boundary. Dislocation-assisted pipe diffusion effects were applied to explain the enhanced growth rate of β phase. Further research [15] by the same research group was conducted by aging Al 5083 alloy at 100℃ for as long as 3 months, and their results show that β phase starts to nucleate at the grain boundary after 14 days, and the grain boundary was fully covered by β phase after aging time increased to 45 days. Zhu *et al.* [23] reported that intergranular β phase is able to form at 70℃ as long as sufficient aging time (12 months) is given. Their results revealed that intergranular β phase formed at the grain boundary of Al 5083 H131 aged at 175 ℃ for 15 days is much thicker than that of the sample aged at 70℃ for 12 months. *In situ* TEM results by D'Antuono *et al.* [37] shows that β phase is more easily precipitated on low-angle grain boundaries, while contrary conclusions were reported by Zhao *et al.* [38] and Yan *et al.* [39]. Grain boundaries of plane orientation {110} and {100} are believed to be immune to the precipitation of β phase. [38,39] In addition, coincident site lattice (CSL) grain boundaries can also affect the precipitation of intergranular β phase. [39]

2.4.3 Effects of alloy elements on the precipitation of Al-Mg alloys

Micro-alloying is an effective way to improve the microstructures, mechanical properties, and corrosion resistance of Al-Mg alloys. For example, Carroll *et al.* [40] reported that Zn addition to sensitized Al 5083 alloy led to the formation of a discontinuous intergranular τ-phase ($Mg_{32}(Al,Zn)_{49}$), which precluded the formation of intergranular *β* phase. Further research by Meng *et al.* [41] shows that Zn addition also helped to keep the precipitate inside the grain matrix and decrease the corrosion potential of the matrix. Sc combined with Zr served as a potent grain refiner for casting Al-Mg alloys. [42] In addition, fine $AlSc_3$ precipitates are able to inhibit the recrystallization of deformed Al-Mg alloys annealed at high temperature, and obtain a suitable strengthening effect. [43] Cu was found to improve the yield strength of Al-Mg-Cu alloy aged at 180℃. [44] Moreover, Guinier-Preston-Bagaryatasky (GPB) zones are believed to play a critical role in hardening during early stage aging, while S" phase contributes to the precipitation hardening in later stages. [45] Even though addition of Cu helps to improve the corrosion resistance of Al-Mg alloy, the mechanism behind this is still unknown. [44] The effect of trace addition of Ag on the precipitation behavior of Al-Mg alloy was investigated by Kubota *et al*., [46] and their results indicate that Ag facilitates the nucleation of intragranular *β*" phase.

2.4.4 Effects of cold working on the precipitation of Al-Mg alloys

The effect of mechanical treatment on the properties of Al 5xxx alloys has been investigated by many research groups. Tran and Riba [47] processed the surface of sensitized Al 5456 H116 using an ultrasonic impact treatment (UIT) method, and scanning electron microscope (SEM) results revealed that a deformed layer of thickness ranging

from 10 to 18 μm formed on the surface. Voids and tearing were observed in the deformation layer, and there is a delamination layer between the UIT surface and the matrix. Nanograins ranging in size from 2 to 200 nm were found in the deformation layer, and β phase became discontinuous in this layer. Zhang *et al.* [48] performed cold rolling, cryorolling, equal channel angular pressing (ECAP), and high-pressure torsion on the same Al 5083 alloy samples, and microhardness of the processed samples was increased. In addition, EBSD results indicated that the fraction of high-angle grain boundaries (HAGB) increases with the number of ECAP passes, while cryorolling leads to a lower fraction of HAGB compared with the original sample. By combining ASTM G67 mass loss results with grain size and the fraction of HAGB, they concluded that the fraction of HAGB plays a more critical role for ASTM G67 mass loss results when grain size is smaller than 1μm. [48]

2.5 Modeling of intergranular precipitation

2.5.1 Zener's model

Zener [49] proposed that precipitate thickening was only controlled by solute diffusion within the grain matrix, and that precipitates formed a continuous film at the grain boundary through the whole aging process. Therefore, based on a mass balance of solute, the thickness of precipitate can be calculated using the concentration of solute at different places within the grain matrix. Since this method assumes a continuous film at the grain boundary, the thickness of precipitates is much smaller than experimental results involving discontinuous precipitates. Goswami and Holtz [15,36] adopted the model developed by Zener to estimate the thickness of β phase formed at the grain boundary of Al 5xxx alloy.

2.5.2 The collector plate model

Aaron and Aaronson [50] first developed a model for grain boundary precipitation. By realizing the rapid lengthening and thickening rates of allotriomorphs cannot be explained by a volume diffusion mechanism [51] alone, they accounted for the role of grain boundary short circuit diffusion using a collector plate mechanism. In their model, thickening of θ phase ($CuAl_2$) was controlled by diffusion of Cu at the interface of α:θ, and lengthening was controlled by diffusion from the bulk to the grain boundary and then to the advancing edge of θ phase. Their theory was successfully applied to Cu-Al alloys.

Based on the theory of diffusion along grain boundaries developed by Fisher [52] and Shewmon, [53] and the theory of the surface morphology change resulting from diffusion developed by Mullins [54] and Nichols and Mullins, [55] Brailsford and Aaron [56] put forward a theory to solve simultaneously the lengthening and thickening rate of θ phase at the grain boundary of Cu-Al alloys. In their research, an equation was used to describe the shape of θ phase, and a corresponding mass balance of Cu was taken into account. The model was solved numerically, and the results agreed well with experimental observation.

Faulkner and Caislery [57] combined the approaches of Aaron and Aaronson for grain boundary precipitation in Nimonic PE16. In order to avoid the complicated mathematical approach of solving lengthening and thickening simultaneously, they assumed a constant aspect ratio throughout the early stage of growth, which led to a rough assessment of overall size of precipitates as a function of time and temperature.

Carolan and Faulkner [58] modified the previous collector plate mechanism-based theory and applied it to the precipitation of $M_{23}C_6$ precipitation at the grain boundary of austenitic steel. They adopted a time-dependent collector plate and took into account

different precipitation morphologies such as cap, faceted, disc, and conical shapes. The model accurately predicted the growth of $M_{23}C_6$ of different shapes.

Faulkner and Jiang [59] developed a combined model, in which they took into consideration the solute segregation, nucleation of grain boundary precipitates, and their growth and coarsening, and the model realistically predicted the influence of heat treatment on the behavior of grain boundary precipitation. They further modified the model [60,61] by determining the influence of heat treatment on the width of precipitate-free zones and the growth rate and dispersion of the precipitates at the grain boundaries as well as the critical time for coarsening initiation and the size and dispersion of precipitates during coarsening. Hass [62] applied this model to predict growth of grain boundary precipitate in Al 6xxx and 7xxx alloys.

2.5.3 Speight and Hyot's model

Considering the effects of incubation times and frequency factors, Zeldovich [63] and Russell [64,65] developed a method for treating nucleation kinetics at grain boundaries. After Slyozov's work [66] on the coarsening of precipitates situated at grain boundaries, Kirchner [67] derived an expression for the steady-state coarsening of intergranular precipitates using the same method as Wagner, [68] and Speight's growth equation [69] was also employed in this model. In order to develop a more rigorous theory to describe the volume fraction dependence of the coarsening rate constant and the distribution of particle size, Ardell [70] modified Speight's precipitate growth law [69] by considering $\ln(r'/r)$ as a variable. Moreover, he used an expression for the mean-free distance between two nearest precipitates derived by Bansal and Ardell, [71] and related it to the volume fraction of

precipitates. The model was solved using the same method employed by Lifshitz and Slyozov. [72] Their results revealed that the average particle size increases in proportion to the one-fourth power of time at high-angle grain boundaries when aging time is long enough. Furthermore, they also considered the coarsening that happened at low-angle grain boundaries.

Hoyt [73] developed a new precipitate growth rate, instead of adopting Speight's growth law. He assumed that solute atoms diffused along the grain boundary as well as through the bulk material during the coarsening stage. The model was solved by employing an asymptotic method attributed to Marqusee and Ross, [74] and the result showed that the average precipitate size varies in proportion to the one-third power of time, and the bulk and grain boundary diffusivity of solute atoms influences the coarsening rate constant. However, there is a high risk that the solute atom conservation equation will break down if the solute flux between the grain boundary and matrix is too high, which can be easily caused by choosing the wrong magnitude of solute diffusivity in the grain matrix.

2.5.4 Molecular dynamic, phase field, and kinetic Monte Carlo model

Recently, molecular dynamic (MD), [75,76] phase field model (PFM), [77,78] and kinetic Monte Carlo (KMC) [79,80] methods have been widely used to simulate the precipitation behavior at grain boundaries. These methods can provide detailed information, such as equilibrium shape, concentration gradient, and size distribution of the precipitates. By taking into account the diffusion of solute atoms along the interfaces, Amirouche and Plapp [81] found the steady-state growth rate of the growing precipitate front was highly influenced by the relative magnitudes of the solute diffusion coefficients at different places

(grain bulk, boundary, and the matrix-precipitate interface). In addition, they also found the hypothesis of local equilibrium at interfaces was invalid for the discontinuous precipitation situation. Clouet *et al*. [82] employed a KMC method developed by Soisson [83] to simulate the precipitation behavior within the grain matrix and at the grain boundary. Their results showed that the KMC method is very useful to predict the heterogeneous nucleation behavior in multicomponent alloys. MD, PFM, and KMC are powerful tools for simulation at the nanoscale.

2.6 Modeling of intragranular precipitation

2.6.1 The Classical nucleation, growth, and coarsening theory

For heat-treatable alloy, the precipitation of a second phase in the matrix is usually used to enhance the mechanical property, such as strength, hardness, and creep resistance. [84] Various kinds of models have been applied to simulate the precipitation process. Among all the existing models, the classical nucleation and growth theories provide an easy and reliable method to predict the evolution of chemical composition, size distribution, volume fraction, and number density of precipitates. In addition, the solute concentration in the matrix can also be obtained based on the mass conservation of solute atoms. Based on different stages of the precipitation process, the classical nucleation and growth theory can be divided into three different stages, which are nucleation, growth, and coarsening. [85]

During the nucleation stage, clusters of radii larger than the critical radius will nucleate in the matrix of the alloy. The expression used to describe the nucleation rate was proposed by Volmer and Weber, [86] improved by Becker and Doring [87] and Zeldovich, [63]

and further modified by Kampmann and Wagner, [88] and the final form is written as follows:

$$\frac{dN}{dt} = NZ\beta^* \exp\left(-\frac{\Delta G^*}{kT}\right)\exp\left(-\frac{\tau_0}{t}\right) \tag{2.1}$$

where N is the number of available nucleation sites, Z is the Zeldovich factor

$$Z = \frac{v_{at}^P}{2\pi R^{*2}}\sqrt{\frac{\gamma}{kT}} \tag{2.2}$$

where, γ is the interfacial energy matrix-precipitate, v_{at}^P is the atomic volume, and R^* is the critical radius. β^* is the condensation rate of the solute atoms to a cluster of critical radius R^*, [64] which equals to

$$\beta^* = \frac{4\pi R^{*2} DX}{a_0^4} \tag{2.3}$$

where D is the diffuse on coefficient of the solute atom, C is the solute concentration in the matrix, and a_0 is the lattice parameter. ΔG^* is the energy required for nucleation of precipitates of critical radius R^*. The critical radius can be calculated from the relative bulk Gibbs free energy change and interfacial energy change caused by the nucleation process. The incubation time, τ_0, is given as:

$$\tau_0 = \frac{4}{2\pi\beta^* Z^2} \tag{2.4}$$

Once the nuclei form, the precipitate will start to grow. In binary Al alloy, the growth of precipitate is usually controlled by the diffusion of solute atoms. For spherical precipitates, if the solute is dilute, the precipitate growth rate [49] can be expressed as follows:

$$\left.\frac{dR}{dt}\right|_g = \frac{D}{R}\frac{X - X_i}{X_P - X_i} \tag{2.5}$$

where X_i is the solute concentration at the precipitate-matrix interface and X_P is the solute concentration of the precipitate.

The Gibbs-Thomson effect [89–91] caused by the interface curvature of precipitates has a large effect on the interfacial solute concentration X_i. The Gibbs-Thomson expression is given as follows:

$$X_R = X_\infty \exp\left(\frac{2\gamma v_a^p}{kTR}\right) \tag{2.6}$$

where X_∞ is the precipitate concentration of infinite radius. During the late stage of precipitation, the matrix will become deplete of solute atoms, when the total volume of precipitate will not change any more. However, precipitates of small radius will dissolve (see Eq.(2.5)), and the larger ones continue to grow at the expense of these small ones.

The above stage is called the coarsening stage. Lifshitz and Slyozov [72] and Wagner [92] simultaneously investigate this phenomenon and obtained the precipitate growth rate during the coarsening stage as follows:

$$\left.\frac{dR}{dt}\right|_c = \frac{4}{27}\frac{X_i}{X_P - X_i}\frac{R_0 D}{R^2} \tag{2.7}$$

where R_0 equals to $(2\gamma v_a^p)/(kT)$. While in the real precipitation process, the nucleation, growth, and coarsening stages usually overlap with each other. Therefore, the final growth rate and number changing rate will be modified to take account of the overlap effect of these three stages.

The classical nucleation and growth model has been widely used to predict the precipitation behavior in Al 2xxx, Al 6xxx, and Al 7xxx alloys, and the results agree well with the experimental results. [93] Moreover, the precipitation model can be coupled with other models to predict the mechanical property of alloys. For example, Deschamps and Brechet combined the classical nucleation and growth model with a structural hardening model to predict the yield strength of Al-Zn-Mg alloy. [94] Bardel *et al*. coupled the nucleation and growth model with a work-hardening model, which enabled them to predict the isotropic and kinematic hardening behavior. [95]

Myhr and Grong [96] developed a multiclass approach based on the classical growth theory and a control volume method to simulate the precipitation behavior in Al-Mg-Si alloy. Perez *et al.* [85] compared the mean radius method with the multiclass methods (including the Euler-like and Lagrange-like method) and found that the multiclass method is essential in modeling some complex multistep heat treatment processes. In both the

Euler-like and Lagrange-like approach, the new-forming precipitates were put into the class of radius R^*, and the precipitate growth rate was used to describe the radius evolution versus aging time.

The multiclass model has been applied to predict the precipitation behavior in Al 3xxx alloy and Fe-based alloy. In order to simulate the evolution of multiple precipitates in a multiphase multicomponent system, a model [97] was developed based on the thermodynamic extremum principle [98], and it has been successfully applied to complex precipitation processes in Al alloy [99] and Fe alloy [100]. Chen *et al*. [101] develop a precipitate growth rate equation for precipitation in multicomponent systems by considering the cross-diffusion and high supersaturation. This method was further improved by Rettig and Singer [102] to describe the precipitation process for multicomponent, multiphase, and multiparticle scenarios. A similar method was adopted by Rougier *et al*. [103] to simulate γ' phase precipitation in Ni-based alloy.

2.6.2 Phase field model

Phase field method is another powerful way to simulate the development of microstructure in Al alloys. Unlike the classical nucleation and growth theory, which assumed a sharp interface between the precipitates and the matrix, the interface in the phase field method is assumed to be of a certain thickness, and within the interface, the precipitate transforms gradually to matrix. The detailed governing equations of PFM can be found in Ref. [104].

One advantages of PFM is that it can predict the morphology of the precipitate. Han *et al*. [105] simulate the precipitation of multivariant β-$Mg_{17}Al_{12}$ phase during the aging of

Mg-Al alloy, and in their model they considered the interface anisotropy and the elastic strain energy. In addition, a special meshing method was adopted to deal with the precipitate orientation and elastic strain energy calculation. Their modeling results revealed that the simulated precipitates have a lath shape with lozenge-shaped ends if the effects of interface anisotropy and the elastic strain energy were both considered. Furthermore, PFM can be employed to obtain the three-dimensional morphology and stress filed around the precipitate. Gao *et al*. [106] simulated the precipitation process in Mg-Y-Nd alloy aged at 150-250℃ for different times using PFM, and they found that the equilibrium shape of β_1 phase is a disk with certain habit plane with the matrix. Moreover, they investigated the elastic interaction energy between a nucleating β' phase and the stress field surrounding a β_1 disk, which leads to the finding that both the normal and shear components of the coherency stress tensor are concentrated near the rim of the β_1 disk where the nucleation and growth of β' phase are most favored by the elastic interaction.

2.6.3 Kinetic Monte Carlo

Kinetic Monte Carlo (KMC) is another useful method to simulate precipitates formed in Al alloys. Even though KMC simulation is limited to small samples, of tens of nanometers, it can provide detailed information of size and structure of early stage precipitates. The KMC approach is based on the principal that the diffusion of solute atoms is a random process which can be simulated by the generation of random numbers and the lattice structure of the material. Review on KMC can be found in Ref. [107] and [108].

Slabanja and Wahnstrom [79] combined the KMC with the first principle method to simulate the precipitation process in Al-Mg alloy aged at high and low temperatures. Their

results demonstrate that small $L1_2$ ordered clusters or modulated structures are observed in the sample aged at low temperature, and these clusters became larger and more well-defined for longer aging time; while in the high temperature aged sample, highly ordered and well-defined clusters are observed.

Sha and Gerezo [109] employed the KMC approach to simulate the GPI zone formation in Al-Zn-Mg-Cu (7050) alloy aged at 121℃ for 1500 min. The modeling reveals that GPI zones have formed during the aging process, and cluster coalescence is the major mechanism for the growth of large clusters, which is in good agreement with experimental observations. The number density, size, and chemistry of GPI zones obtained from the simulation agrees well with 3D APT experimental results.

In addition, as KMC is relatively accurate for predicting the nucleation density of solute cluster, and it can be coupled with PFM to predict precipitation for a large sample size. Molnar *et al.* [110] aged Fe-Cu alloy at 700℃, and KMC approach was applied to simulate the early nucleation and growth stage. The PFM was subsequently used to simulate the coarsening of precipitates, and the modeling results closely follow the LSW temporal law in the same regime. However, the coarsening rate increases with the increasing volume fraction of precipitates.

2.7 Corrosion of Al and Al 5xxx alloys

2.7.1 Electrochemistry of Al

The standard electrode potential of Al is -1.66V, which is highly negative, indicating Al should be very unstable in a moist environment. [18] However, Al has been reported to have excellent corrosion resistance, which can be attributed to the formation of a thin oxide

film (several nm thick) on the surface. The thin oxide film is very stable in natural environments, and can reform immediately when damaged. [111] The structure of the oxide film can be affected by the composition of the material, the crystal structure of the material, and the micro defects of the material.

The Pourbaix diagram of Al is shown in Fig. 2.5. [17,18] In the pH range of 3.9-8.6, a passive oxide film will form on the surface of Al, while in a more acidic or basic environment, Al will dissolve. The corresponding reactions [18,111] are listed as follows:

In the passive regime, the film formation reaction can be expressed as

$$2Al + 3H_2O \rightarrow Al_2O_3 + 6H^+ + 6e^- \quad (2.8)$$

In the acidic regime, the dissolution of Al matrix is expressed as

$$2Al + 6H^+ \rightarrow 2Al^{3+} + 3H_2 \quad (2.9)$$

and the dissolution of the passive film is expressed as

$$Al_2O_3 + 6H^+ \rightarrow 2Al^{3+} + 3H_2O \quad (2.10)$$

In the alkaline environment, the dissolution of Al matrix is written as

$$Al + 2H_2O \rightarrow AlO_2^- + 4H^+ + 3e^- \quad (2.11)$$

and the dissolution of the passivation film in basic environment is written as

$$Al_2O_3 + H_2O \rightarrow 2AlO_2^- + 2H^+ \quad (2.12)$$

Pure Aluminum is not strong, and it does not find any major applications in the industry. Therefore, alloying elements, such as Cu, Si, Mn, Mg, are added to improve the mechanical properties. [19] As mentioned above, the main alloying elements in Al 5xxx alloys are Mg and Mn. [19] The corrosion properties of Al 5xxx alloys have been extensively investigated recently, which will be reviewed in the next section. The corrosion of Al 5xxx alloy can often be classified as pitting corrosion, exfoliation corrosion, intergranular corrosion, and stress corrosion cracking.

2.7.2 Pitting of Al 5xxx alloys

Pitting corrosion is a kind of localized corrosion, which is characterized by the formation of irregularly shaped cavities on the surface of the metal. [111,112] As shown in Fig. 2.6, [18] Al is prone to pitting in media with a pH close to neutral, such as sea water, moist air, and natural water films. Pitting is usually more dangerous than uniform corrosion, since it is difficult to detect. The initiation of pitting starts from the localized breaks in the passive film caused by absorbing chloride ions. [111] Most of the pits will stop after a few days because of repassivation. Only a small fraction of the pits will continue to grow. In these pits, the dissolution of Al and hydrolysis of Al^{3+} will happen, which will decrease the pH of the solution in the pit. Moreover, in order to keep the electroneutrality of the solution, chloride ions will diffuse into the pit, which will make the solution more conductive and

aggressive. If the anode is stable, the above process will keep proceeding and dig a cavity on the surface of the Al alloys. [111,112]

Trueba and Trasatti [113] investigated the pitting corrosion behavior of Al 5083 H111 and Al 5754 H111 in neutral NaCl solution using single-cycle polarization. Electrochemical parameters, such as pitting potential, repassivation potential, and pit transition potential were determined in deaerated and naturally aerated NaCl solutions. Their results revealed that the potential difference of pitting and transition can be used to predict the propensity towards localized pitting corrosion of Al alloys in a specific corrosive environment. Guan *et al*. [114] investigated the pitting behavior of Al-5wt.%Mg alloy aged at 150℃ for different times, and their results demonstrated that metastable pitting was closely associated with nanoscale β phase, the size of which increases with aging time. Moreover, the current transient caused by dissolution of β phase has been recorded in sensitized samples. In addition, their results showed that wavelet analysis can be used to differentiate the metastable pitting behavior with the overlapped current transients and the small microstructural changes for samples aged for a long time.

Pitting corrosion has been reported to happen preferentially around intermetallic particles in Al alloys. The corrosion potential of pre-existing particles and matrix of Al alloys has been investigated by Birbilis and Buchheit, [115] and are listed in Table 2.3. The intermetallic particles are usually noble compared to Al matrix. Therefore, a galvanic cell will form when a pre-existing particle and matrix are exposed to water. The larger the potential difference of these two phases, the easier it is for pitting corrosion to occur. Furthermore, when Al alloys are exposed to elevated temperature, precipitates, such as β phase in Al 5xxx alloys, will form in the matrix, on pre-existing particles, and at grain

boundaries. These precipitates may have lower electrochemical potential than the matrix, and they will preferentially be etched during pitting. For example, the corrosion potential of Al_3Mg_2 and Mg_2Si are -1.12 V (SCE) and -1.36 V(SCE), respectively, which are lower than that of the matrix (-0.68 V_{SCE}).

2.7.3 Exfoliation of Al 5xxx alloys

Exfoliation corrosion is a type of selective corrosion that propagates along a large number of planes in the same direction of rolling and extrusions, and the corrosion products will accumulate at the grain boundary and exert pressure between the grains, which will finally result in a lifting and leafing effect. Exfoliation corrosion has been observed in Al 2xxx, 5xxx, and 7xxx series alloys exhibiting a long-grained structure parallel to the direction of rolling. [18]

Sun *et al.* [116] investigated the exfoliation corrosion of extruded Al 2024 alloy by comparing the corrosion behavior of this alloy exposed to industrial, coastal-industrial, and laboratory-accelerated testing environments. Their results revealed that the coastal atmosphere leads to more severe corrosion than the industrial environment. The thinner coarse grain structure suffered more severe corrosion than the thicker coarse-grain structure after 20 years' of exposure. A small amount of S and a relatively larger amount of Al and O are found in the corrosion products. Furthermore, the existence of SO_4^{2-} is believed to hinder the exfoliation corrosion of Al 2xxx alloy.

Chen and Lai [117] investigated the reversing sensitization of naturally exfoliated Al 5456 H116 alloy. In their study, Al 5456 H116 alloy that was in service for around 20 years was heat treated to 250℃ for different times, and the microstructure results obtained from

SEM revealed that precipitates at the grain boundary had become discontinuous. In addition, the ASTM G67 mass loss test also decreased from 65 mg/cm^2 to 5 mg/cm^2 after being exposed at 250℃. Based on the experimental results, they concluded that by exposing the sensitized sample at 250℃ for 10 to 30 minutes, the exfoliation corrosion can be significantly reduced without affecting the mechanical behavior.

2.7.4 Intergranular corrosion of Al 5xxx alloys

Intergranular corrosion (IGC) is a selective dissolution of grain boundary area of crystalline materials which is anodic to the matrix. In Al 5083 and Al 5456 alloys, Mg is supersaturated at room temperature, and will diffuse to the grain boundary to form Mg-rich precipitates when exposed to elevated temperature for a relatively long time. [11] The Mg-rich phase, which is also called β phase, has a more negative corrosion potential than the matrix and will be selectively dissolved in sea water. [8,115]

The initiation of IGC occurs at exposed metal surface where the passivation film or the near-surface deformation layer (NSDL) is broken. [118] The pre-existing particle, such as Al_6Mn, plays a critical role in the chemical breakdown of the oxide layer, while the NSDL can be removed by rapid cathodic dissolution. The anodic dissolution of β phase generates metal cations, and the hydrolysis of cations as well as absorption of chloride ions that will subsequently facilitate the dissolution of β phase. [119] The chain of pits finally leads to a network of corroded grain boundaries, while the stable penetration of IGC is affected by the chemistry and the potential distribution of fissure tip. If the migration and diffusion of cations and anions provides a suitable chemistry environment, and the potential distribution inside the fissure is appropriate, stable IGC propagation will be expected. On

the contrary, once the chemistry and the potential distribution do not support fissure tip dissolution, IGC propagation will stop. [119]

The degree of sensitization (DoS) of Al 5xxx alloys can be quantified using the nitric acid mass loss test (NAMLT) as stated in ASTM G67. [17] The β phase dissolves two orders of magnitude faster than Al matrix in the 70 vol.% nitric acid at 30°C. The selected dissolving of intergranular β phase network causes the fall-off of grains and the mass loss of the sample bulk. Based on ASTM G67, the IGC susceptibility of Al 5xxx alloys can be classified as resistant (DoS<15 mg/cm^2), intermediate (DoS<25 mg/cm^2), and susceptible (DoS>25 mg/cm^2). [17] In addition, a phosphoric acid etching method is also used to quantify the IGC susceptibility of Al 5xxx alloys. The concentration of phosphoric acid varies from 10 vol.% to 40 vol.%, according to previous research. [12] However, the size of β phase obtained from the etched microstructure is much larger than the results obtained from TEM. Therefore, less aggressive etchants such as ammonium persulfate and liquid Ga were adopted to evaluate the IGC behavior of Al 5xxx alloys. [120]

The IGC susceptibility of Al 5xxx alloys is defined by the difference between the breakdown potentials of the anodic grain boundary zones and the alloy matrix. [119] In neutral chloride solutions, the breakdown potential of Al 5xxx alloys is associated with the spreading of IGC to nearby β phase and the onset breakdown potential of β phase. Jain *et al.* [121] built an electrochemical framework to describe the range of potential over which Al 5083 is susceptible to IGC in solutions of different NaCl concentrations. Their work demonstrates that IGC will spread on the sample surface if an applied potential is located between the breakdown potential of sensitized Al 5083 alloys and the breakdown potential of β phase. This finding was substantiated by the corrosion experiments of highly sensitized

Al 5083 H131 in 0.6M NaCl solution with different applied potentials. In this research, a large area of IGC spreading was only observed at the highest applied potential (-0.73 V_{SCE}) situation. However, this electrochemical framework only works for the IGC spreading on the surface, and the propagation of IGC in the bulk needs to consider the local chemistry and potential of the fissure tips. [119]

2.7.5 Stress corrosion cracking of Al 5xxx alloys

Stress corrosion cracking (SCC) is the brittle failure at relatively low constant tensile stress of an alloy exposed to a corrosive environment. Based on the definition, a critical environment, a susceptible alloy, and some component of tensile stress are three important conditions for the initiation of SCC.[121] Even though these three factors are not usually present together, time and service conditions may conspire to produce the necessary combinations that result in the final failures. SCC is normally associated with static tensile stress, which is different from the cyclic tensile stress for corrosion fatigue. [122]

Extensive experimental and theoretical research has been conducted to investigate the mechanism of SCC, and several mechanisms have been proposed to explain SCC, such as hydrogen embrittlement, absorption-induced cleavage, surface mobility, film rupture, and film-induced cleavage. [123] Among these mechanisms, hydrogen embrittlement has been widely accepted to be the control mechanism for Al-Mg alloy. The hydrogen embrittlement mechanism is based on the assumption that hydrogen atoms are able to weaken interatomic bonds in the plane strain region at the crack tip (see Fig. 2.7). [123]

Searles *et al.* [8] investigated the SCC behavior of Al 5083 alloy by means of an electrochemistry method, constant-extension-rate testing, and TEM analysis. Their results

demonstrate that β phase is more active than the matrix, and it can spontaneously passivate up to -0.94 V_{SCE}. The breakdown potential of β phase is not sensitive to variation in solution pH. The ductility measured by constant extension rate testing can be largely affected by the extent of β phase precipitation at grain boundaries. When aged at 150°C, the total strain to failure in 3.5 pct NaCl increases first and then decreases, and the minimum value is achieved at 189 hours. Furthermore, when the polarization potential is located in the passive regime of β phase, the SCC resistance for the sensitized samples is restored. Jones *et al.* [10] investigated the SCC of Al 5083 alloy aged at 175°C for different times. According to their results, the precipitation of intergranular β phase increased SCC by a factor of 350. They also found that H atoms played a critical role in the crack growth of Al 5083 alloy. H was reduced by the dissolution of anodic β phase, and the cracks propagated along the grain boundaries where β phase was totally dissolved in Al 5083 H321. More information of SCC of Al 5xxx alloys can be found in Ref. [123].

Table 2.1 Composition (wt.%) of Al 5083 and Al 5456 alloys.

	Al	Mg	Mn	Fe	Cr	Si	Zn	Ti	Cu
Al 5083	Bal.	4.0-4.9	0.4-1.0	0.4	0.05-0.25	0.4-0.7	0.25	0.15	0.1
Al 5456	Bal.	4.7-5.5	0.5-1.0	0.4	0.05-0.2	0.25	0.25	0.2	0.1

Table. 2.2 Typical mechanical properties of Al 5083 and Al 5456 wrought alloys.

Properties	Al 5083			Al 5456	
	O	H321, H116	H131	H321, H116	H112
Density/ g/cm^3	2.66	2.66	2.66	2.66	2.66
Ultimate tensile strength/(MPa)	290	315	310	350	310
Tensile yield strength/(MPa)	145	230	255	255	165
Elongation	22	16	8	16	22
Hardness(500 kg, 10 mm ball)/HB				90	
Ultimate shearing strength /MPa	170			205	
Fatigue endurance (5×10^8cycles)/MPa		160			
Modulus of elasticity/GPa	71	71	71	71	71

Table 2.3 Corrosion potentials for intermetallic compounds common in aluminum alloys.

Stoichiometry	Corrosion potential (mV_{SCE}) in NaCl solutions		
	0.01 M	0.1M	0.6M
Al_6Mn	-839	-779	-913
Mg_2Si	-1355	-1538	-1536
Al_3Mg_2	-1124	-1013	-1162
$Al_{12}Mn_3Si$	-890	-810	-858
Al_3Fe	-493	-539	-566
Al	-679	-823	-849
Mg	-1601	-1586	-1688

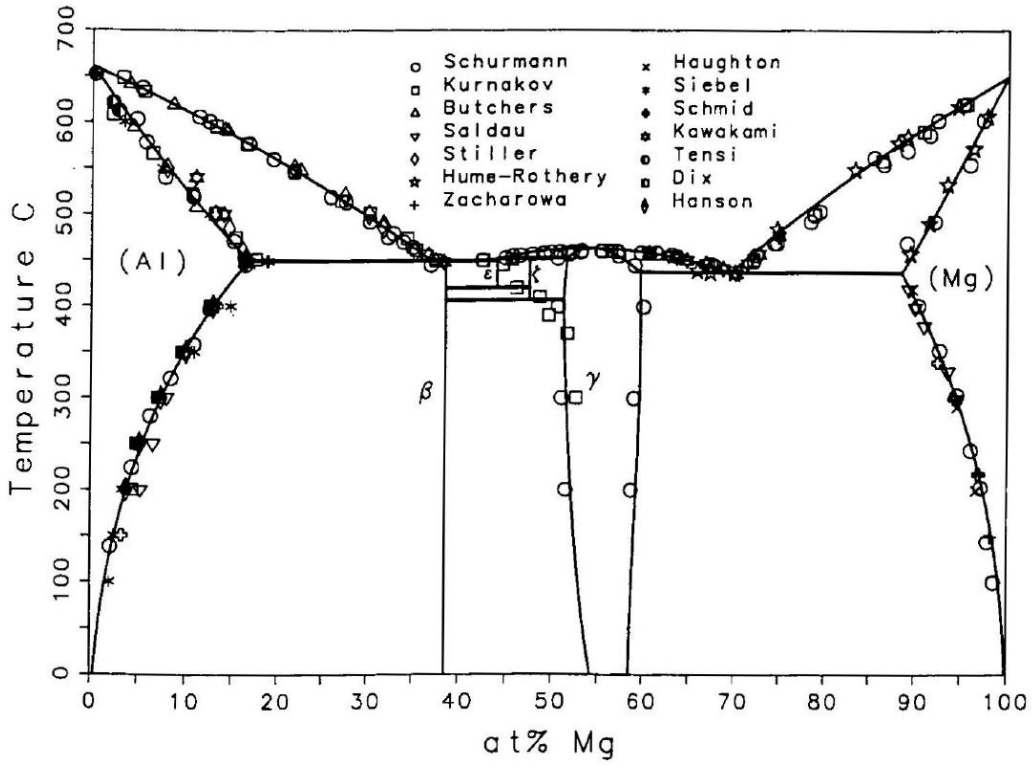

Figure 2.1 Al-Mg binary phase diagram.

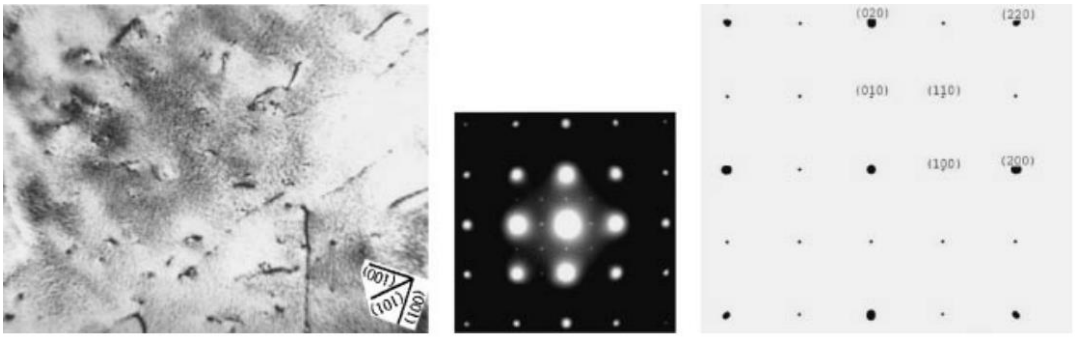

Figure 2.2 TEM image of β" phase (Al_3Mg, $L1_2$), and the corresponding selected area diffraction pattern.

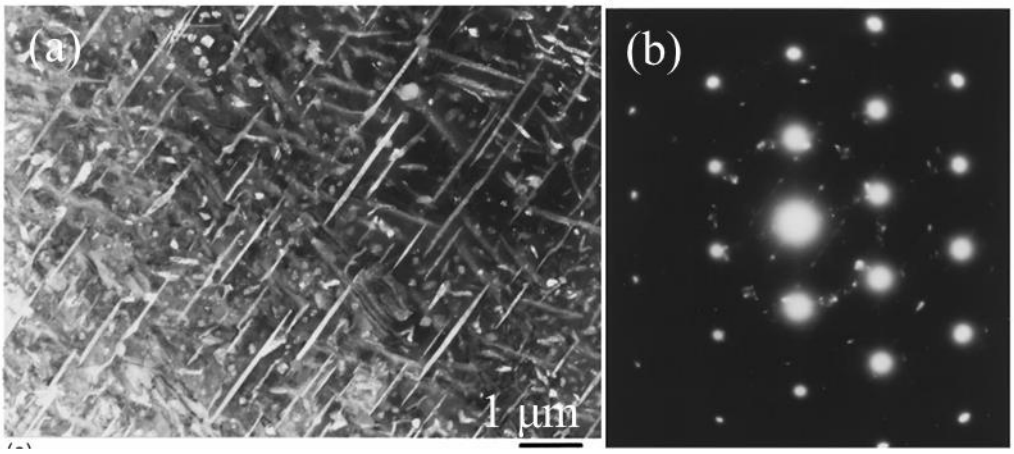

Figure 2.3 TEM results for an Al-Mg (16 at.%) binary alloy sample (a) TEM image of *β*' phase (Al_3Mg_2, hcp), and (b) the selected area diffraction pattern of (a).

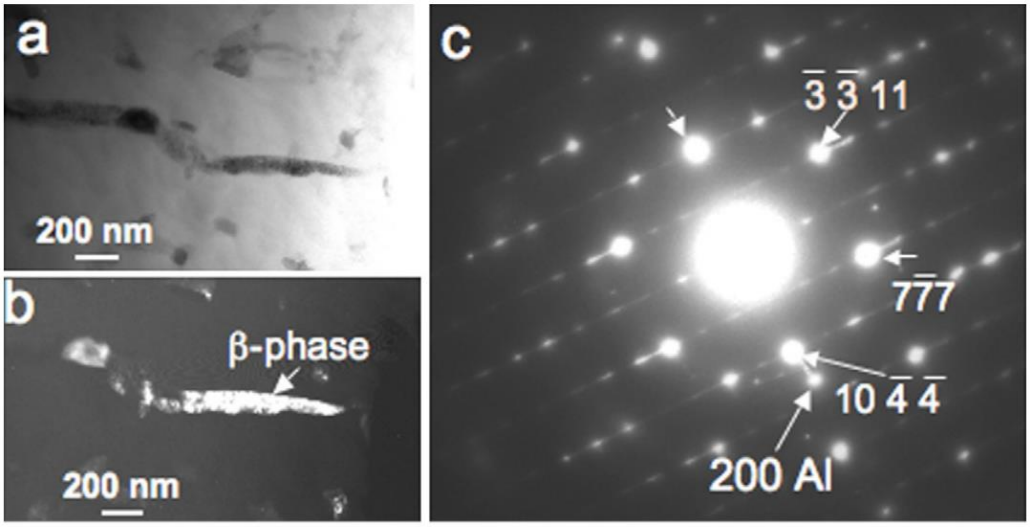

Figure 2.4 TEM results of Al 5083 H131 aged at 175℃ for 10 days (a) DF, (b) BF-STEM image of *β* phase, and (c) selected area diffraction pattern of *β* phase.

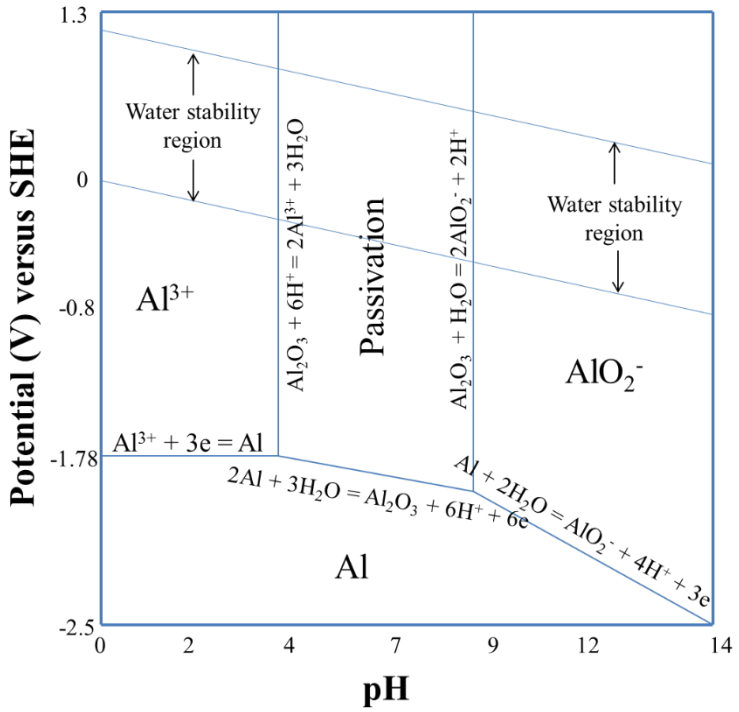

Figure 2.5 Potential versus pH diagram for aluminum (activity of Al = 10^{-6}).

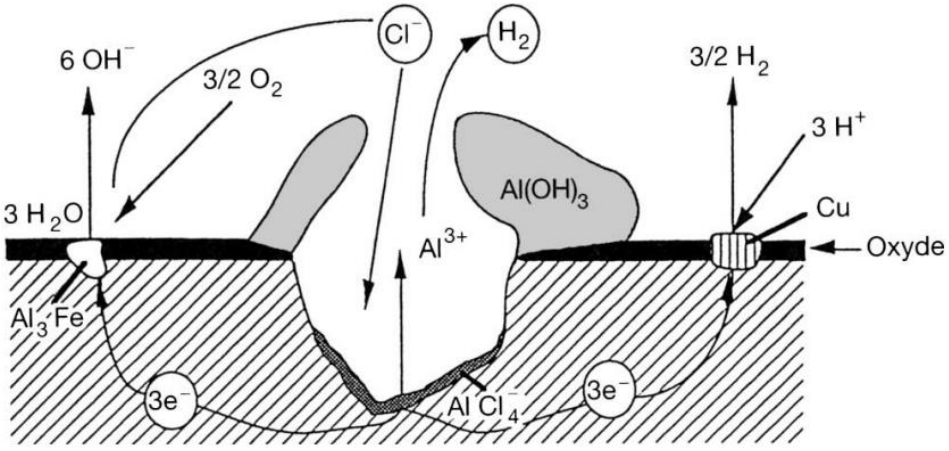

Figure 2.6 Schematic diagram for mechanism of pitting corrosion of Al.

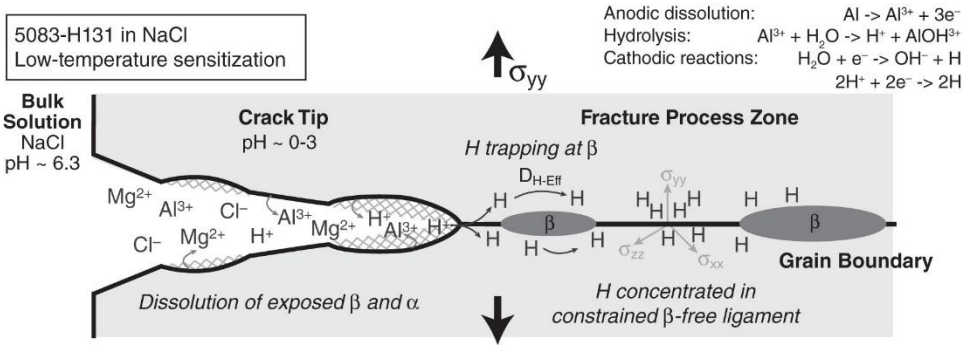

Figure 2.7 Schematic diagram for role of H played in the intergranular stress corrosion cracking of Al 5083 H131 alloy.

CHAPTER 3

EXPERIMENTAL PROCEDURES

3.1 Materials

3.1.1 As-received alloys

Seven types of commercial alloys were investigated in the present study. Al 5083 alloys of temper H131 and H116 were supplied by Alcoa Inc., Al 5083 H321 and Al 5456 H116 were supplied by Pierce Aluminum Inc., and Al 5050, 5052, and 5154 of H32 temper were supplied by CHALCO. As stated above, Mg concentration plays a critical role in the sensitization of Al 5xxx alloy. In this study, Mg concentration in Al 5083 alloys is 4.85 wt.%, and in Al 5456 is 5.2 wt.%. The Mg content is 1.5±0.4 wt.% in 5050-H32, 2.5±0.3 wt.% in 5052-H32, and 3.5±0.4wt.% in 5154-H32. In addition, a sample cutting from a real navy ship in service for more than 10 years is also characterized in this research.

3.1.2 Sample cutting

The as-received milled plates were cut into different sizes based on the requirements of different tests. For ASTM G67 tests, the samples were cut along the rolling direction as shown in Fig. 3.1. [17] The final size of the test coupon is 51 mm (in length direction)×7 mm (in transverse direction)×26 mm (in short transverse direction). An extra 1mm in all

dimensions was added to account for the subsequent polishing. The sample size for SEM and TEM characterization is 10 mm×10mm×10mm, and the sample size for SANS test is 17 mm (in length direction)×17mm (in short transverse direction)×5mm (in transverse direction).

3.1.3 Sample heat treatment

In order to mimic the natural sensitization process of Al 5xxx alloys, Al alloy samples (including ASTM G67 test samples, SEM & TEM samples, and SANS samples) were put into ovens of constant and cyclic temperatures. The aging temperatures were determined from the real temperature profile of a naval ship that started from San Diego, CA and traveled to Panama City, FL via the Panama Canal. Fig. 3.2 shows the detailed temperature profile provided by the Naval Surface Warfare Center (NSWC). [17] During the measuring period, the temperature of the samples mounted on the deck (including vertical and horizontal samples) ranges from 40℉ (4.5℃) to 150℉ (65.5℃). However, temperatures below 40℃ have little effect on the sensitization of Al 5xxx alloys. Therefore, the constant temperatures for the aging experiments were set to be 40, 50, 60, and 70℃. Four ovens (VWR digital mini incubator) were used to carry out the constant aging experiments, as shown in Fig. 3.3. The temperatures of the ovens were monitored using thermometers.

In order to simulate the temperature change during an entire day, cyclic aging experiments were also set up. The highest temperature during a whole day appeared during the 4 hours in the middle of the day, and the hottest temperature during this period is around 40℃ for spring. Thus, cyclic aging experiments with a temperature range 40-45℃ and a period of 6 hours were conducted to simulate the sensitization behavior of Al 5xxx in spring.

However, the highest temperature of the ship between January and April was 65.5℃ in the tropical areas. It is reasonable to expect even higher temperature during the summer in some regions. Thus, a temperature range of 50-70℃ was adopted to model the extreme peak temperature for the ship, and the period of the short-cycle experiments is also 6 hours. Furthermore, in order to simulate the temperature of a ship serviced in both cold and tropical regions, extra long-cycle experiments of temperature ranging from 30-70℃ and a period of 12 hours were also conducted. Fig. 3.4 shows the real temperature, the fitting temperature, and the temperature in the oven for the long-cycle 30-70℃ aging experiments.

The cyclic temperatures were controlled using a feedback circuit operated by LabView. The preset temperature profile was programmed using LabView on the control computer, the temperature of the oven was measured using a thermocouple, and the temperature signal was then transferred to an electronic signal using specific equipment (NI USBTCO-1, National Instrument). [17] By comparing the preset temperature with the temperature of the oven, the controller switches on and off the power of the oven, which ensures the temperature profile is cyclic versus time. The tolerance of the controller is 0.5℃. The overall cyclic aging temperatures are shown in Fig. 3.5. The as-quenched samples for SANS experiments were obtained by solutionizing the alloys at 450℃ for 3 hours and quenching them in water immediately.

3.2 Sample preparation

3.2.1 Samples for SEM/EBSD

SEM samples aged at different temperatures (both constant and cyclic) for different times were mounted using epoxy, where the epoxy to hardener ratio is 10:4. To achieve

enough hardness for polishing, the epoxy resin and hardener needs to be mixed sufficiently before pouring into the mold where the sample is located. In addition, another 24 hours are needed for the mixture to become solid. The polishing step started with SiC polishing papers (P240 and P600). Then UltraPol polishing cloth with 9 μm suspension of alumina and Trident polishing cloth with 3 μm suspension alumina were used in sequential order. The samples were finished by ChemoMet with 50 nm colloidal silica suspension for 4 hours. The surface of the sample was cleaned using a cotton ball and dried using compressed air every time before moving to the next step. In order to reveal the grain boundary under SEM, the sample was immersed into 70 vol.% HNO_3 at 30℃ for 1 min.

3.2.2 Samples for S/TEM

STEM samples were prepared by first cutting a 3 mm-disc using a disc punch. The discs were then ground and polished to a thickness of less than 10 μm by a dimple grinder. An argon ion mill operating at 5 keV with an incidence angle of 15 deg was used to thin the sample to achieve electron transparency. Final cleaning was performed at 1keV with an incidence angle of 10 deg using the same ion mill.

3.2.3 Samples for atom probe tomography

APT needle-shaped samples were prepared by top-down and cross-sectional FIB lift-out methods [124] using a FEI Nova 200 dual beam SEM/focused ion beam (FIB). The lift-out section was subsequently mounted on a microtip array post that was annularly milled (30 kV) and cleaned with a 5-kV ion beam to make needle-shaped specimens suitable for field evaporation.

3.2.4 Samples for small angle neutron scattering

The size of the SANS sample is 12×12×1 mm. Both sides of the sample surface (10×10 mm) were ground using SiC polishing paper, and finished with 1200 grit. The as-quenched (AQ) sample was aged at 450℃ for 3 hours, and quenched in cold water.

3.2.5 Samples for atom force microscopy

AFM was able to obtain the tomography of a sample in nanoscale, therefore an extra step was needed to get rid of the scratches introduced during the polishing steps. The sample was first processed in the same procedure of the SEM EBSD sample, and a SEM ion mill was subsequently used to further improve the surface condition. The parameters for the ion mill process are listed in Table. 3.1.

3.2.6 Samples for ASTM G67 mass loss test

The susceptibility of the Al 5xxx alloys mentioned above to IGC was investigated following the ASTM G67 mass loss test protocol. The sensitized samples were polished (finished using 240/P280 SiC polishing paper) and then soaked in NaOH solution (5wt.%, 80℃) for 1 minute, followed by a water rinse and drying by compressed air. Subsequently, the dried samples were immersed in nitric acid (70 wt.%) at room temperature for 30 seconds.

3.3 Characterization techniques

3.3.1 SEM and EBSD

The microstructure of Al 5xxx samples was obtained using an FEI NovaNano SEM equipped with a field emission gun. The high voltage is 30 kV, and the spot size is 4.0. The electron backscatter diffraction (EBSD) results were collected using a FEI Quanta 600 SEM equipped with a field emission gun electron source (FEG) and an EBSD detector. To obtain the geometrical necessary dislocation (GND) density, a scanning step size of 0.5 μm was adopted. The acquired EBSD datasets were processed using the TSL-OIMTM software (EDAX Inc., USA).

3.3.2 S/TEM

A Hitachi HF-3300 scanning electron transmission microscopy (S/TEM) (300 kV) equipped with a Bruker SDD-EDS detector, a JEOL JEM-2200FS (200 kV) probe-corrected STEM equipped with a Bruker X-Flash detector, a JEOL 2800 STEM/TEM equipped with an ultrafast EDS system (dual high counts SDD-EDS detectors), and an FEI Talos F200X S/TEM were used to characterize the microstructure of the Al 5083 and 5456 alloy. The acquired EDS results were processed using the NSS 3.2 software (Thermo Fisher Scientific Inc.) to obtain maps, line scan results, and quantification results.

3.3.3 Small angle neutron scattering

SANS is a powerful technique which is able to provide microstructural information, in a nondestructive way, on structural inhomogeneities and compositional fluctuation present in alloys. In this study, SANS was performed at Oak Ridge National Laboratory

(ORNL) High Flux Isotope Reactor (HFIR) General Purpose Small Angle Neutron Scattering (GP-SANS) instrument. [125] The wavelength (obtained by a mechanical velocity selector) of the incident neutron beam is λ=0.472 nm with a spread of 15%. The data were collected using the 1 m square 8 mm diameter linear gas tube helium detector array, which was offset from the center in the y-axis (0.665m) in order to measure a larger scattering vector (q) range. The scattering vector magnitude equals ($4\pi\sin\varphi/\lambda$), where 2φ is the scattering angle. The overall range of q is from 0.007 $Å^{-1}$ to 0.7 $Å^{-1}$. The data were measured at two sample-to-detector distances (1.129m and 7.829m), where the shorter sample to detector distance (1.129m) is suitable to measure precipitates of small size (around 1 nm). The data collection times were 1800 s, and all SANS measurements were conducted at room temperature.

The SANS raw data were reduced to absolute scattering intensities $d\Sigma(q)/d\Omega$ after correction for transmission, background, and thickness using the package of routines developed at HIFR operating in the Wavemetrics Igor Pro software environment. Data obtained in the q range of 0.05~0.7 $Å^{-1}$ were scaled to the match the data acquired from the q range of 0.007~0.1 $Å^{-1}$ to generate the combined curves.

Based on the two-phase model of isolated particles in a homogeneous matrix, [25] the SANS cross-section was calculated as

$$\frac{d\Sigma}{d\Omega}(q) = \int_0^\infty (\Delta\eta)^2 n(R) V^2(R) \left|F(q,R)\right|^2 dR \qquad (3.1)$$

where $\Delta\eta$ is the difference in scattering length densities of precipitate and matrix, $n(R)dR$ stands for the number density of precipitates between R and $R+dR$, $V(R)$ is the volume of

precipitates, and $F(q, R)$ is the form factor. Moreover, the item, $k_c q^{-4}$, is added in consideration of the effect of sharp interfaces between larger inhomogeneities and matrix. A background, c, caused by scattering of compositional fluctuations is also added.

For random orientated precipitates, $F(q, R)$ for ellipsoids can be calculated as follow [25]:

$$\left|F(q,R)\right|^2 = \int_0^{\pi/2} \left[F_s(q, R\sqrt{\cos^2\theta + u^2 \sin^2\theta})\right]^2 \cos\theta d\theta \tag{3.2}$$

with

$$F_s(q,R) = 3\frac{\sin(qR) - qR\cos(qR)}{(qR)^3} \tag{3.3}$$

where $F_s(q, R)$ is the form factor for spherical particles of radius R. The particle size distribution, $n(R)$, is described by log-normal distribution functions:

$$n(R) = \frac{n_0}{\sqrt{2\pi}\sigma R} \exp\left(-\frac{\left(\ln(R/R_a)\right)^2}{2\sigma^2}\right) \tag{3.4}$$

where n_0 is the number density, σ is the width of the distribution, and R_a is the average radius of the precipitate. The volume fraction of precipitates can be calculated as:

$$f_V = \int_0^\infty n(R)V(R)dR = \int_0^\infty \frac{4}{3}\pi n(R)uR^3 dR \quad (3.5)$$

3.3.4 Atom probe tomography

Atom probe tomography (APT) analyses were performed using CAMECA Instruments LEAP 4000 XHR (see Fig. 3.7). The LEAP was operated in voltage-pulse mode with a specimen temperature of 50 K, a pulse repetition rate of 200 kHz, a 20% pulse fraction, and a 0.3% to 5% detection rate. The resulting data were reconstructed and analyzed using commercial CAMECA IVAS software.

Fig. 3.8 shows the main components and the principle of operation of atom probe tomography. [126] Atoms are ionized and field-evaporated from the apex of the cryogenically cooled (20-70 K) needle-shaped specimen by a high-voltage pulse superimposed on a standing voltage. The elemental identities of these ions are determined from the mass-to-charge ratios. The mass/charge ratio can be calculated from the acceleration voltage V, ion flight time t, and the sample-detector distance d, as (constVt^2/d^2). The x and y coordinates of each field-evaporated atom are derived from the highly magnified impact position, x_1 and y_1, on the position-sensitive single atom detector. The z coordinate is determined by the order in which the atom was detected. The final 3D images of the internal structure of materials were reconstructed from thousands of slices, each containing a few atoms with known elemental identity and coordinate information. [127]

3.3.5 Atomic force microscopy

The surface tomography of the sample was examined using the JPK NanoWizard atomic force microscope operating in contact and intermittent contact modes. Fig. 3.9 is a

schematic diagram of AFM imaging mechanism. [128] The basic idea of AFM operation is that the local attractive or repulsive force between the tip and the sample is converted into a bending, or deflection of the cantilever. The detection system uses a laser beam that is reflected from the back of the cantilever onto a quadrant photodiode detector. The optical lever principle makes it possible to measure the deflection of a cantilever, which is subsequently used to reconstruct the tomography of the sample. [129]

Based on different force between the tip and the sample, AFM can work in different modes, such as the force modulation mode, contact mode, intermittent contact mode, and noncontact mode. For the contact mode, the tip never leaves the surface, which is very helpful for high resolution imaging. Even though the vertical force can be controlled in this mode, the lateral force as the tip moves over the surface may cause detrimental effects on the sample. While for the intermittent mode, the tip does not contact the sample for most of the time, which can effectively decrease the harmful effect of lateral forces. This mode is good for imaging relatively rough surfaces. [130]

3.4 Thickness and continuity of β phase detection

The average thickness and continuity of β phase was obtained from STEM images. The shape of β phase is usually allotriomorphic. The thickness of β phase was measured using Gatan Digital Micrograph software, which was able to give an accuracy in the nanoscale range. The thickness of one precipitate was obtained by measuring the maximum thickness of the precipitate. The final thickness of the sample was obtained by calculating the average value of all measurements. The continuity results of β phase were obtained using a different method. A series of equal-spaced (two to three times of thickness for

intergranular precipitates) parallel lines were drawn in the vertical direction using Gatan Digital Micrograph, and the number of lines intersect with β phase was counted as N_β. For certain STEM images, the continuity result was obtained as N_β/N_{tot}, where N_{tot} is the total number of lines in the STEM image.[17] The average continuity of multiple images (usually >30) was the final continuity result.

3.5 Intergranular corrosion evaluation

3.5.1 ASTM G67 mass loss tests

ASTM G67 mass loss test, which is also called nitric acid mass loss test (NAMLT), is a standard method for measuring the susceptibility to intergranular corrosion of Al 5xxx alloys. The NAMLT method involved immersing the prepared specimens (aged at different temperatures for different times) in concentrated HNO_3 at 30℃ (water bath) for 24 hours, and determining the mass loss per unit area. The experiments were repeated once.

3.5.2 Nitric acid and phosphoric acid etching experiments

In order to investigate the corrosion resistant properties of different grain boundaries, an Al 5083 H131 sample was etched in 70 vol.% HNO_3 at 30℃ for 1, 3, and 5 min. SEM was used to obtain images of different grain boundaries etched form different times. The etching experiments for AFM examination were performed on two Al 5083 H131 alloy samples aged at 70℃ for 30 months. Both HNO_3 (70 vol.%) and H_3PO_4 (10 vol.%) were used to etch the sample surface. The etching time for nitric acid was 15 seconds, and the etching time for phosphoric acid was 2 minutes.

Table 3.1 Parameters of Fischione ion mill used for AFM sample preparation

Parameters	Value
Chamber pressure	7-10 Torr
Beam energy	5 keV
Beam current	10 mA
Beam angle	9 deg
Etching time	30 min

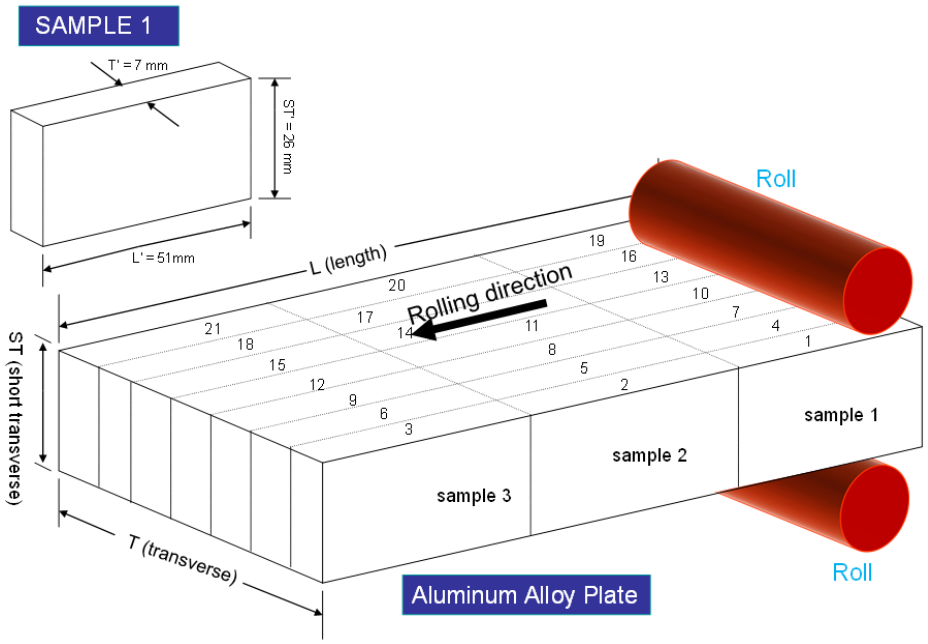

Figure 3.1 Schematic diagram showing the as-received Al 5083 alloy plates and samples for ASTM G67 mass loss tests.

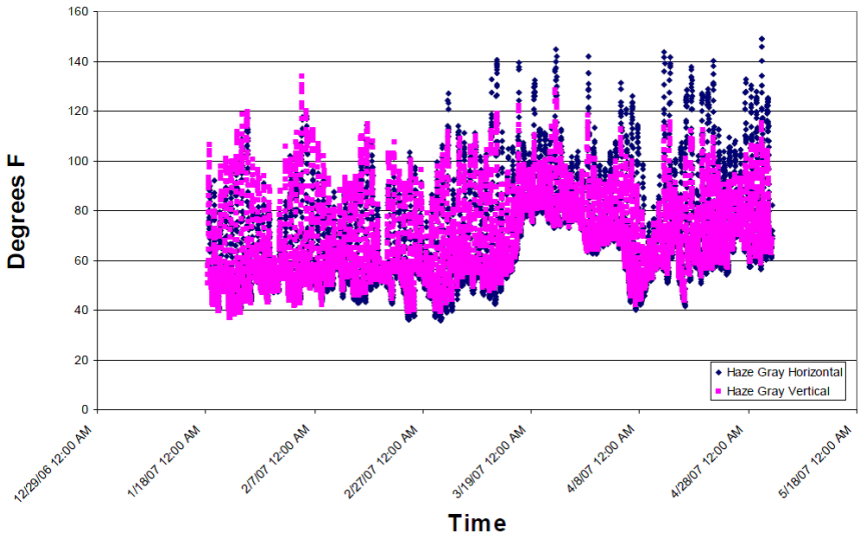

Figure 3.2 Deck temperature of a real US navy ship in sea atmosphere.

Figure 3.3 Ovens used for constant and cyclic aging experiments.

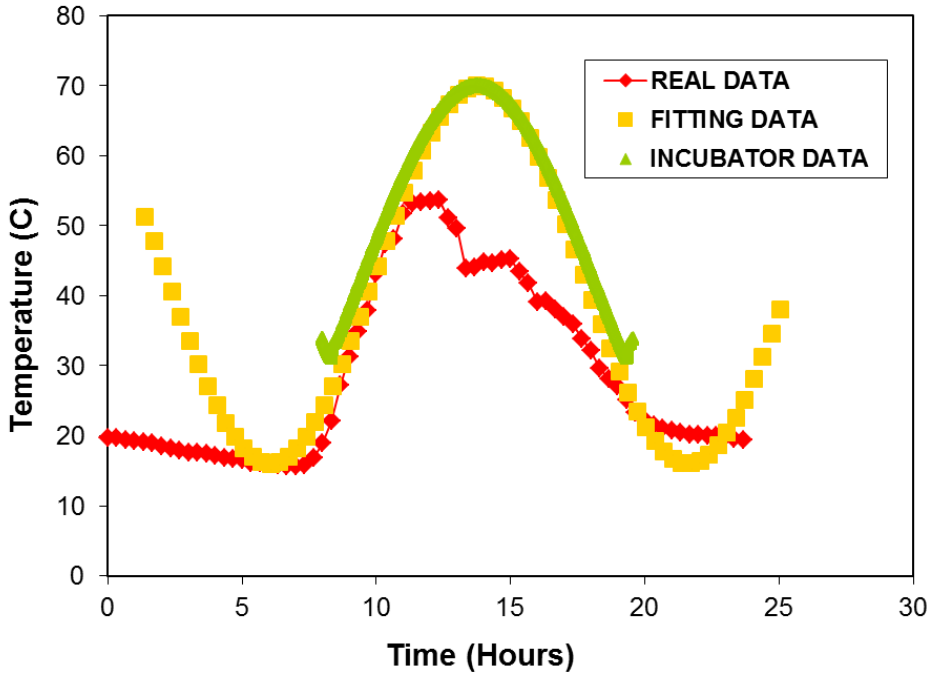

Figure 3.4 Real temperature of the deck and the corresponding fitting temperature, and the temperature in the oven for the 30-70℃ long-cycle aging experiments.

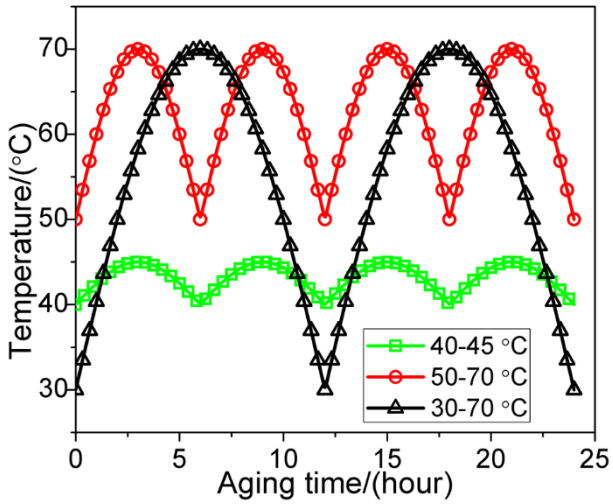

Figure 3.5 The short-cycle and long-cycle time-temperature relationships for the long-term aging experiments simulating daily cyclic outdoor thermal exposure to sunlight (the period is 6 hours for the 40-45, 50-70℃ aging experiments, and 12 hours for the 30-70℃ aging experiments).

Figure 3.6 Two tanks for the detectors of general purpose small angle neutron scattering beam lines.

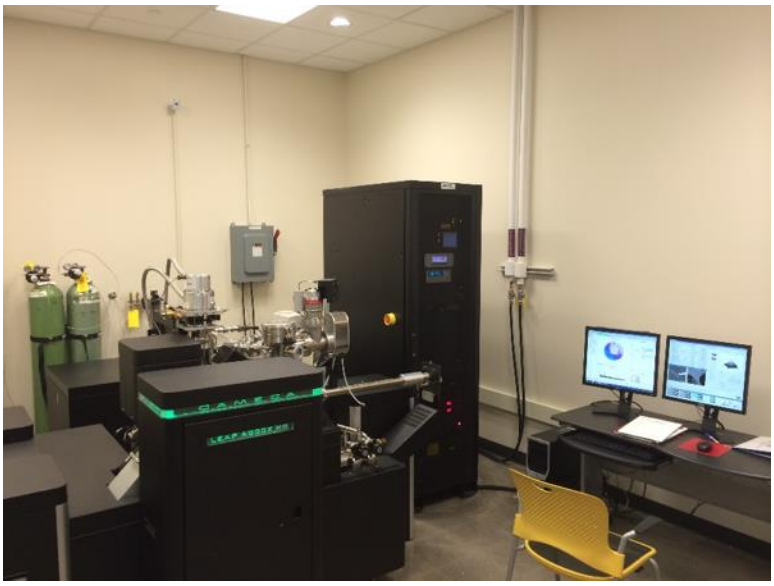

Figure 3.7 Image of the CAMECA Instruments LEAP 4000 XHR.

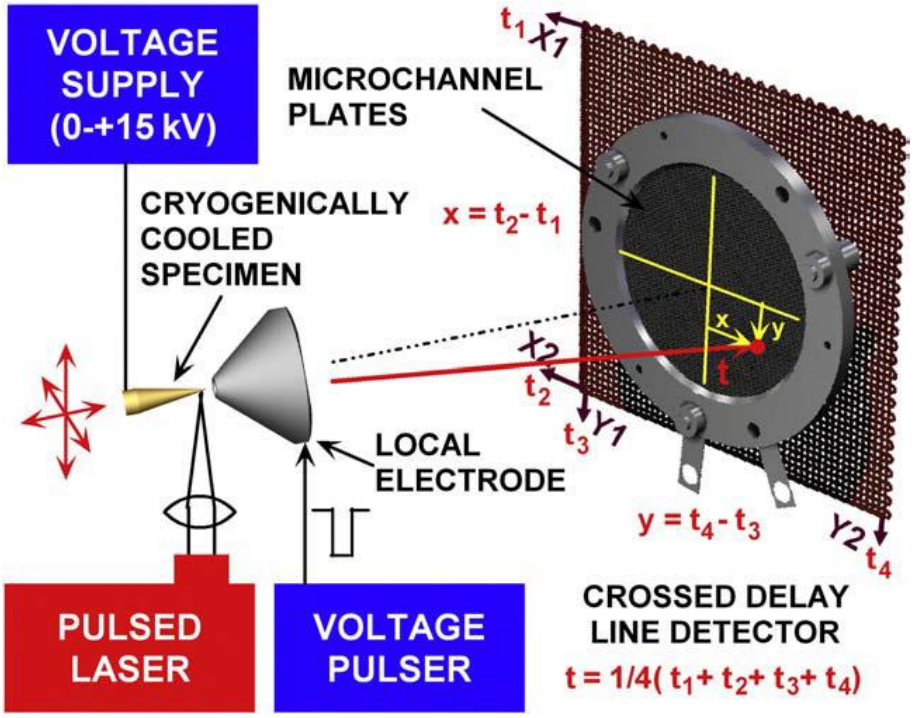

Figure 3.8 Schematic diagram of main components and the principle of operation for atom probe tomography.

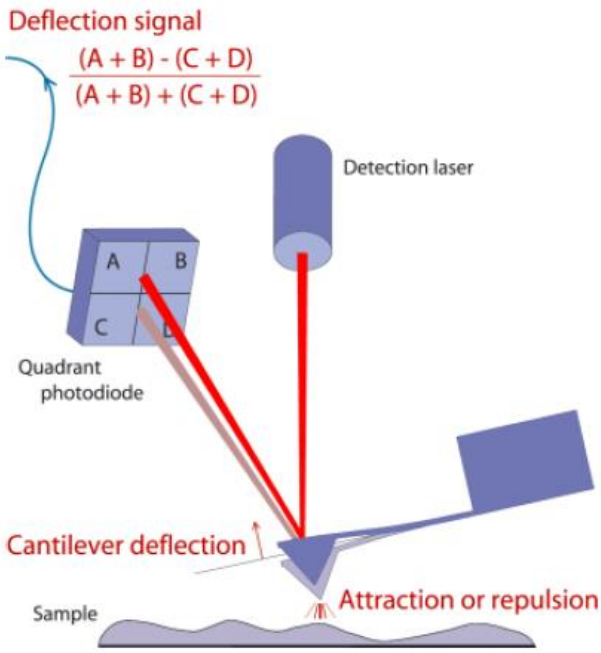

Figure 3.9 Schematic diagram for the imaging mechanism of atomic force microscopy.

CHAPTER 4

MICROSTRUCTURE CHARACTERIZATION OF Al 5XXX ALLOYS

4.1 EBSD results of Al 5xxx alloys

Fig. 4.1(a) and (b) show the inverse pole figure maps of Al 5083 H131 and Al 5083 H116, respectively. Most grains of Al 5083 H131 exhibited a lamellar structure which was elongated along the rolling direction (RD) (see Fig. 4.1(a)). The average width of the grain along the normal direction (ND) is about 16 μm, and the average aspect ratio of the grain is ~25. Furthermore, some subgrain boundaries (highlighted by an arrow in Fig. 4.1(a)) have already formed in the elongated grain matrix of Al 5083 H131. As shown in Fig. 4.1(b), some coarse grains of Al 5083 H116 are also elongated along the RD, and the size of the largest grain is about 700 μm in length and 200 μm in width. In addition, some equiaxed grains are also observed in Al 5083 H116, as highlighted in Fig. 4.1(b). Most coarse grains in Al 5083 H116 share the orientation of (101). Fig. 4.1(c) demonstrates the grain size (in diameter) distribution of Al 5083 H131 and H116. The average diameter of Al 5083 H131 is 9.1 μm, which is smaller than that (17 μm) of Al 5083 H116. The grain boundary misorientation angle results are presented in Fig. 4.1(d). The fraction of low-angle grain boundary (LAGB, $2^{\circ}<\theta<15^{\circ}$, θ is the grain boundary misorientation angle) for Al 5083 H131 is 0.84, which is slightly larger than that (0.77) of Al 5083 H116.

Fig. 4.2 (a) and (b) shows the geometrically necessary dislocation (GND) density mapping results for (a) Al 5083 H131 and (b) H116. Compared with the grain matrix, the grain boundary regions (highlighted by arrows) have a relatively higher GND density in both alloys, which is consistent with a previous study found in Ref. [131]. The average GND density for Al 5083 H131 and H116 are 5.33×10^{13} m^{-2} and 3.28×10^{13} m^{-2}, respectively.

The typical EBSD result of as-received Al 5456 H116 is shown in Fig. 4.3(a). All grains are elongated along the rolling direction, and the average aspect ratio of the grains is 0.12. Fig. 4.3(b) shows the grain width ranges from 5 μm to 68 μm, and the average grain width is 13.3 μm. The grain boundary misorientation result is shown in Fig. 4.3(c), which reveals that most (~58%) of the grain boundaries are low-angle grain boundaries. Based on our previous research, [132,133] Al 5456 H116 has smaller grain width, more high-angle grain boundaries, and higher mass loss compared with Al 5083 H116 aged at the same temperature for the same time.

4.2 AFM results of Al 5xxx alloys

Fig. 4.4 (a) and (b) are the vertical trace images of grain boundaries (as highlighted by arrows) in Al 5083 H131 aged at 70℃ for 30 months. The distance between two grain boundaries in Fig. 4.4(b) is around 3μm, which is constant with our transmission electron microscopy (TEM) results. [23] Furthermore, pre-existing particles of ellipsoid shape are also observed within the grain matrix. The size of pre-existing particles is around several hundred nm. Fig. 4.4(c) is the height trace image of the area within the dash frame in Fig. 4.4(b). A line scan is conducted across the grain boundary. The height distribution

information reveals that the grain boundary area is 4nm lower than the matrix on both sides, indicating Mg-rich precipitates are more easily etched away by the Argon ion mill. The thickness extracted from the height distribution data is 95nm, as shown in Fig. 4.4(c), which is larger than the value reported by Zhu.[23] The possible explanation is that dislocations induce pipe diffusion effects that facilitate the diffusion process. Moreover, the aging time is longer than that in Ref. [23]. Fig. 4.4(d) is the 3D image of Fig. 4.4(c), and the tomography of this area reveals that the pre-existing particle at the grain boundary is of the highest height.

Fig. 4.5 (a) and (b) are vertical and horizontal trace images of two grain boundaries in Al 5456 H116 aged for 18 months at 50℃. The thickness of the grain boundary is around 10 nm, which is much smaller than the value in Fig. 4.4(c). Discontinuous precipitates were observed in Fig. 4.5 (a), (b) and (c). Small intragranular precipitates, as indicated in Fig 4.5. (b) and (c), were found to form in the Al 5456 H116 sample, and the size of the precipitates is around 5 nm. Intragranular Mg-rich phases, such as GP zones, β'', and β' phase, have been observed to form within the matrix of Al 5456 H116 aged at 70℃ for 30 months. Therefore, these intragranular precipitates identified by the AFM could be the prime phase of β.

Fig. 4.6 is the AFM image of a grain boundary in Al 5083 H131 aged at 70℃ for 30 months using the tapping mode. Compared with the contact mode, the tapping mode is able to obtain more accurate tomography information of a surface, and save AFM tips as well. The length of the grain boundary if Fig. 4.6 (a) is 30 μm, and the line scan along the grain boundary (marked by number "1" in Fig. 4.6(a)) reveals that the height of the grain boundary is different, indicating the etching rate of β phase by ion mill could be different

even for the same grain boundary. In addition, another line scan across the matrix of Al 5083 H131 aged at 70℃ for 30 months (indicated by number "2") shows that there are two pits of 2 nm in depth. The pits could also be caused from Mg-rich phase etched away by ion mill. Fig. 4.6(b) is the 3D image of Fig. 4.6(a), which clearly shows the tomography of the matrix, the grain boundary area, and the pre-existing particles.

4.3 STEM results of Al 5xxx alloys

4.3.1 STEM results of intragranular Mg-rich precipitates formed in Al 5xxx alloys

The bright field (BF) STEM images of as-received Al 5083 H131 and H116 are shown in Fig. 4.7 (a) and (c). In the matrix of H131 and H116, rod-like and plate-like pre-existing particles (indicated by "×") are observed, which could be Al_6(Mn,Cr,Fe)-type pre-existing particles as reported [15,23] previously. Dislocation networks (highlighted by arrows) are also found in the matrix of both alloys. Two high-resolution TEM images of Al 5083 H131 and H116 are shown in Fig. 4.7 (b) and (d), and the inserted fast Fourier transform (FFT) patterns reveal no precipitates in the matrix.

Fig. 4.8 (a) is the BF-STEM image of Al 5083 H131 aged at 70℃ for 1.5 months. No obvious difference can be observed compared with the as-received H131 sample (Fig. 4.7(a)). Additional EDS maps (Fig. 4.8(b)) reveal that precipitates have already formed on pre-existing particles. The thin lamellar precipitate formed on the end of the needle-shaped pre-existing particle (rich in Mn and Fe) is rich in Mg and Si (indicated by arrows), which could be an Mg_2Si-type [134,135] precipitate. The plate-shaped pre-existing particle (rich in Cr, indicated by a dash cycle) worked as a heterogeneous nucleation site for the globular Mg-rich precipitate (13.5 at.% Mg). EDS maps of the 9 months' sample (Fig. 4.8(d))

demonstrate that larger Mg-rich precipitates have formed on the Al_6(Mn,Fe,Cr)-type pre-existing particles. Furthermore, some tiny Mg-rich precipitates (highlighted by arrows in Fig.4.8 (d)) also nucleate without the help of pre-existing particles. When aging time increases to 18 months, precipitates with a darker contrast than the matrix can be observed in the dark field (DF) image (Fig. 4.8(e)) (highlighted by arrows). The nucleation sites for these precipitates are subgrain boundaries, and EDS maps (Fig. 4.8(f)) illustrate that these precipitates are rich in Mg. Fig. 4.8(g) shows the DF image of the 30 months' sample. The size of these intragranular precipitates is even larger, and no subgrain boundaries or pre-existing particles are found to associate with the nucleation of these Mg-rich (Fig. 4.8(f)) precipitates. In addition, no Si-rich precipitates are identified in the 9, 18, and 30 months' samples. The average aspect ratio of precipitates is 0.3 (see Table 4.1). The average size of Mg-rich precipitates of different aging times is determined from STEM images and EDS mapping results, Table 4.1.

Fig. 4.9 (a) and (b) are the STEM BF image and the corresponding EDS maps of Al 5083 H116 aged at 70℃ for 3 months. Mg-rich precipitates are only detected on the end of an Al_6Mn-type pre-existing particle. Large teeth-like Al_6(Mn,Fe,Cr)-type and (Mn,Fe,Cr,Si)-rich (highlighted by arrows) [136] pre-existing particles were found in Al 5083 H116 aged at 70℃ for 9 months, as shown in Fig. 4.9 (c) and (d). In addition, only one Mg-rich precipitate (indicated by a cycle) is observed near the pre-existing particles. While in the 18 months' sample (Fig. 4.9(e) and (f)), more precipitates were found to form on pre-existing particles and grain boundaries, as well as within the matrix. Moreover, intragranular Mg-rich precipitates were found on dislocations, as highlighted by arrows in Fig. 4.9(e). The size of the intergranular precipitates is obviously larger than that of the

intragranular ones, which could be attributed to the "collector plate" effect of grain boundaries; see Ref. [137]. Even larger (see Table 4.1) Mg-rich precipitates are found in the 30 months' sample, as shown in Fig. 4.9(g) and (h). The size and aspect ratio results of precipitates formed in Al 5083 H116 are summarized in Table 4.1. Fig. 4.10 shows the precipitate size distribution of Al 5083 H116 aged at 70℃ for 18 months. The experimental results fit very well (R_{square}=0.9966) using a cumulative log-normal distribution.

The STEM images and EDS maps of Al 5083 H116 aged at 50℃ for different times are shown in in Fig. 4.11. Mg-rich precipitates were not able to be identified in the 9 months' sample (see Fig. 4.11 (a) and (b)), but Mg-rich precipitates were observed on pre-existing particles in the 24 months' sample, as shown in Fig. 4.11 (c) and (d) (indicated by a dash cycle). After aging at 50℃ for 41 months (see Fig. 4.11 (e) and (f)), the size of Mg-rich precipitates formed in Al 5083 H116 is only 13.5 nm (Table 4.1).

Mg concentration, as shown by previous studies, [23,137] plays an important role in the sensitization behavior of Al-Mg alloys. STEM-EDS measurements give average Mg concentrations in Al 5456 H116 of 5.2wt.%, which is within the normal range (4.7-5.5 wt.%) of commercial Al 5456. [21] For Al 5456 H116 aged at 70℃ for 1.5 months, a thin layer (3nm) of Mg-rich precipitate (see Appendix A.1 for EDS line scan results) was observed to form at matrix-pre-existing particle interfaces as shown by the inserted image in Fig. 4.12 (a). The particle in Fig. 4.12(a) (highlighted by a yellow arrow) is rich in Mn and Fe (see Appendix A.1 for EDS line scan results), which is an Al_6(Mn)-type pre-existing particle, as reported in previous research. [23,36] Fig. 4.12 (b) and (c) are BF-STEM images of Al 5456 H116 aged at 70℃ for 9 and 18 months, respectively. Mg-rich precipitates (indicated by arrows) are found to form on pre-existing particles as shown by inserted EDS

mapping results of Mg. In addition, no Mg-rich precipitates were observed within the matrix of Al 5456 samples aged for 1.5, 9, and 18 months. Fig. 4.12(d) is the BF STEM image of Al 5456 aged at 70℃ for 30 months, where it is shown that thicker Mg-rich precipitates form on pre-existing particles. Moreover, continuous Mg-rich precipitate is found to form at the grain boundary, and the thickness of the intergranular precipitate is about 14 nm.

For Al 5456 H116 aged at 70℃ for 30 months, some fine-scale precipitates are also observed within the Al matrix as shown in Fig. 4.13(a). Most of the precipitates are elliptical and randomly distributed. Fig. 4.13(b) shows the size distribution of intragranular Mg-rich precipitates within the grain matrix of Al 5456 H116 aged at 70℃ for 30 months. The total size distribution fits a log-normal distribution as shown by the inserted image of cumulative fitting result (R-square=0.996) in Fig. 4.13(b), and the average precipitate size is 16.4 nm (in radius), which is much larger than the reported size of GP zones [27] (1.9 nm, Al-11.5%Mg, aged at 0℃ for 9 months) and β" phase [31] (4 nm, Al -10 wt.% Mg aged at room temperature for 550 hours) formed in Al-Mg alloy. Additionally, as shown in Fig. 4.13(a), the distance between these precipitates is larger than 50 nm, which is also larger than the reported distance between GP zones (12.5 nm in Ref. [16] and 5.6 nm in Ref. [138]). Both of the reported values of size and inter-distance of GP zones and *β*" phases are smaller than our measurement of Mg-rich precipitates (including GP zone, *β*", and *β*' phase), which was attributed to the coarsening process of *β* phase as stated by T. Sato *et al*. [16].

Fig. 4.14(a) shows the TEM image of four intragranular precipitates, and Fig. 4.14(b) is the high-resolution TEM image of precipitate 2, as shown in the square frame in Fig.

4.14(a). The fast Fourier transformation (FFT) results of Al matrix and the area in the square frame in Fig. 4.14(b) are inserted in Fig. 4.14(a) and (c), respectively. Two different sets of reflections, one from the precipitate (highlighted by cycles), and the other one from the matrix surrounding the precipitate ((200), indicated by an arrow) are identified for the area in the square frame of Fig. 4.14(b). It turns out that the precipitate has the same structure of Al matrix. EDS mapping (see Appendix.A.2) and line scan (inserted image in Fig.14(c)) results reveal that the precipitate is rich in Mg. In Al-Mg alloy, GP zones are reported to form as a result of the aggregation of Mg atoms and have the same structure of Al matrix, and based on the FFT and EDS line scan results, precipitate 2 in Fig. 4.14(a) could be a GP zone. As highlighted by two solid lines in Fig. 4.14(b), a misorientation angle, 23.2°, is observed between the (111) direction of Al matrix and the (200) direction of the matrix surrounded the Mg-rich precipitates. Because of the different lattice spacing of the (111) and (200) direction, a dislocation is found at the interface of these two matrix locations of different orientations (as indicated by the mismatch of lattice numbers in Fig. 4.14(b)). Fig. 4.14(c) is the inverse FFT (IFFT) (mask was applied to keep the reflections of the precipitate and Al matrix) result of the area within the frame in Fig. 4.14(b), and two dislocations, as highlighted by the symbol "⊥", are observed. Fig. 4.14(d) is the TEM image of another precipitate. Fig. 4.14(e) shows a high-resolution image of the area in Fig. 4.14(d), and the FFT results of Al matrix and the precipitate (indicated by a frame in Fig. 4.14(e)) are shown in Fig. 4.14(f). FFT result indicates that the precipitate has the same structure as Al matrix except one extra refection (highlighted by an arrow), which could be caused by extra misoriented planes. Therefore, the precipitate in Fig. 4.14(e) could also be a GP zone.

Fig. 4.15(a) and (b) are the high-angle annular dark field (HAADF) STEM images and the corresponding EDS mapping results of a grain boundary obtained using a JEM 2800. For comparison, the same grain boundary was re-examined by FEI Talos F200X S/TEM, and the HAADF and EDS mapping results are shown in Fig. 4.15(d) and (e). Mg-rich precipitates were observed to form at the grain boundary as well as on Al_6(Mn-Fe-Cr) type [23,36] pre-existing particles as revealed by EDS mapping results in Fig. 4.15(b) and (d). EDS line scan results show Mg concentrations of precipitates formed at the grain boundary and pre-existing particles (as highlighted by arrows in Fig. 4.15(a)) is close to 37 wt.% (see Fig. 4.15(c) and (f)), indicating β phase [23] particles have already formed at these places. In addition, EDS mapping reveals that 5 Mg-rich precipitates (as indicated by numbers) nucleate within the grain matrix, and the Mg concentrations of these precipitates are listed in Table 4.2. Raynal and Roth [27] reported that GP zones were found in Al-11.5% Mg alloy aged at 0°C for 9 months using small angle neutron scattering, and the Mg concentration of GP zones was suggested to be 19%. In the decomposition process, GP zones will be replaced by β'' phase (Al_3Mg) with 22.86 wt.% Mg. [16,32,139] After aging at 175°C for 15 days, β' phase (Mg concentration 27 wt.%) [23] was observed at the grain boundary of Al 5083 H131. As shown in Table 4.2 (see Appendix A.3 for EDS line scan results), both the peak and the average (average over the size of the precipitate) Mg concentration of precipitates 2 and 4 are less than 19%, which could be GP zones. The average Mg concentrations of precipitates 1 and 5 is very close to 27 wt.%, which could be β' phase. The average Mg concentration of precipitate 3 is close to 22.86 wt.%, indicating it could be β'' phase.

Fig. 4.16 shows STEM images and EDS results of a sample obtained from a navy ship in service for more than 10 years. Precipitates are found to form on pre-existing particles (Fig. 4.16(a)), at the triple junction of grain boundaries (Fig. 4.16(b)), and at grain boundaries (Fig. 4.16(c)). The thickness of precipitates at the grain boundary is around 5 nm, and the grain boundaries do not appear to be fully covered by precipitates, even though the ASTM G67 mass loss is high, as discussed later in the text. Fig. 4.16(d) is the STEM image of two intergranular precipitates, and the corresponding EDS line scan results for one precipitate (highlighted by an arrow in Fig. 4.16(f)) are shown in Fig. 4.16(e). The Mg concentration of the precipitate is about 24.3 wt.%, which is consistent with β'' phase. Thus, the precipitate in Fig. 4.16(d) could be β'' phase. To further identify whether Mg-rich precipitates form within the grain matrix of the navy ship sample or not, high-resolution STEM images were obtained, and one of them is shown in Fig. 4.16(f). No modulated structure, lattice distortion or strain field [16] caused by aggregation of Mg atoms was observed within the grain matrix, suggesting that no GP zones had formed. Moreover, there are no superlattice spots appearing in the FFT pattern (inserted in Fig. 4.16(f)), which confirms no β'' phase is present.

Mg-rich precipitates were observed to nucleate heterogeneously on pre-existing particles or at grain boundaries of Al 5456 H116 alloy samples aged for 1.5, 9, 18, and 30 months, while intragranular Mg-rich precipitates were only found in the matrix of the 30-month sample. In the navy ship sample, Mg-rich precipitates are observed at heterogeneous nucleation sites such as triple junctions of grain boundaries, grain boundaries, and pre-existing particles. This could be explained by the relatively lower activation energy needed for heterogeneous nucleation. For the case of grain boundary nucleation, the nucleation

barrier, ΔG_{het}^{*}, can be estimated from the homogenous nucleation barrier, $\Delta G_{\hom}^{*}$, using the following equation:

$$\Delta G_{het}^{*} = \Delta G_{\hom}^{*} S(\theta) \tag{4.1}$$

where $S(\theta) = (2+\cos\theta)(1+\cos\theta)^2/2$, and θ is the contact angle. [84] Based on STEM results, [137] the value of θ is around 20 deg, and the corresponding S(θ) is calculated to be 0.005, indicating the energy barrier for nucleation at the grain boundary is only 0.5% of that for homogeneous nucleation. Therefore, Mg-rich precipitates prefer to form on heterogeneous nucleation sites.

In Fig. 4.14(c), a GP zone was found around dislocations. Dislocations could possibly play two different roles in the precipitation of Mg-rich phases. First of all, dislocations work as segregation sites for Mg atoms. Three-dimensional atom probe results by D. Blavette *et al*. [140] show that oversized solute atoms tend to segregate to the dilated part of the dislocations (close to the dislocation core below the dislocation line), and the undersize solute atoms are likely to migrate toward the compressed regions above the dislocation line. Therefore, solute-enriched regions form around the dislocation. Furthermore, some solute atoms segregated around the dislocation line will continue to diffuse towards the dislocation core under the driving force produced by strain field caused by dislocation itself. [140] In this case, a solute-enriched area will form at dislocation cores. In the present study, a Mg solute atom on the substitutional site is 12% (r_{Al}=1.43Å, r_{Mg}=1.60Å) larger than an Al atom, which can cause lattice distortion. This kind of distortion can be released when Mg atoms segregate near dislocation lines. In addition,

dislocation cores can also serve as fast paths for solute atoms. Zhu [23] and Goswami [36] have already observed the dislocation-assisted pipe diffusion phenomenon in commercial Al 5083 alloy.

The aging temperature (environmental temperature) for the navy ship sample typically ranges from 5℃ to 70℃ during a day of outdoor exposure to sunlight. [17] The nucleation rate in the navy ship sample can be calculated using the standard Becker-Döring [87] nucleation equation

$$\frac{dN}{dt} = NZ\beta^* \exp\left(-\frac{\Delta G^*}{RT}\right) \tag{4.2}$$

where N is the number of nucleation sites per unit volume, Z is the Zeldovich factor, [63] and β^* [64] is the condensation rate of the solute atoms. The fitted aging temperature (with a periodicity of 12 hours) for the navy ship sample was given in Ref. [131], and the other parameters used in Eq. (4.2) can be obtained from Table 1 in Ref. [141]. The average nucleation rate for the navy ship sample during an aging cycle is only 21% of that in the Al 5456 H116 alloy aged at 70℃. Moreover, the diffusivity of Mg atoms at 70℃ is 20 times faster than that at 45℃, [17] based on the diffusion activation energy [137] of Mg in Al. Therefore, both the radius and the total volume fraction of Mg-rich precipitates in the navy ship sample are smaller than those of the Al 5456 H116 alloy sample (aged at 70℃ for 30 months).

Osamura and Ogura[32] identified the formation of GP zones in Al-Mg (4.64 wt.%) alloy by means of calorimetry and electrical resistivity measurements. Nozato and Ishihara [29] reported that GP zones were able to form in Al-Mg (7.6 at.%) alloy. However,

other researchers [37] have suggested GP zones can only form within Al alloys of higher Mg concentration (>13%). Our EDS results (from both Talos and the JEM) combined with TEM images indicate that GP zones and β'' phase are able to form in Al 5456 H116 alloys (5.2 wt.%) aged at 70℃ for 30 months. Two different β phase precipitation sequences have been reported in previous research. [16,32] For Al alloys of Mg concentration close to 10 at.%, [31,32] GP zones nucleate first, then transform into β'' and β' phase gradually. However, β'' phase will form directly within the grain matrix of Al alloys of Mg concentration higher than 20 at.% during the aging process. [16,32] In the present study, GP zones, β'', and β' phase are observed in Al 5456 alloy aged at 70℃ for 30 months, indicating that it follows a precipitation sequence similar to the first type.

Considerable previous research reported that Mg-rich phases (including GP zones and β'' phase) tend to distribute periodically along certain directions ([200] and [220]) within the grain matrix, [16,31] and two mechanisms, homogeneous nucleation and spinodal decomposition mechanisms, [16,27,31] were applied to explain this phenomenon. However, Mg-rich precipitates in Al 5456 H116 alloy aged at 70℃ for 30 months were not found to distribute along certain directions. One possible explanation is that Al-Mg alloys used in previous research were cast alloys without further mechanical work, while Al 5456 H116 is a wrought alloy which has more dislocations. Consequently, Mg-rich phases in Al 5456 will preferentially nucleate on sites like dislocations (as shown in Fig. 4.14), which have low energy barriers [84] and are widely distributed within the grain matrix [23,36]. The nucleation precipitates associated with dislocations have also been observed previously in Al 6xxx [142] and 7xxx [143] alloys.

4.3.2 STEM results of intergranular Mg-rich precipitates formed in Al 5xxx alloys

As shown in Fig 4.17, experimental results of intergranular Mg-rich precipitates for Al 5083 aged at 70℃ for different times were obtained using TEM. Fig. 4.17(a) and (b) are DF-STEM images, and the dark precipitates observed at the grain boundary indicate the enrichment of Mg. In Fig. 4.17(c), (d), and (f), EDS mapping and EDS line scan results of the corresponding area clearly reveal that the grain boundary is rich in Mg. Fig. 4.17(e) shows the presence of β phase using a selected area diffraction pattern. The thickness and continuity of intergranular precipitates increases with aging time.

Fig. 4.18(a) to (b) illustrates that intergranular precipitates formed within Al 5083 H116 aged at 50℃ for 41 months and 70℃ for 18 months. It is noticeable that the grain boundary of Al 5083 H116 is still discontinuous after exposure at 50℃ for 41 months. In addition, discontinuous intergranular precipitates were also observed at the grain boundary of Al 5083 H116 aged at 70℃ for 30 months

The experimental continuity results of Al 5083 H131 aged at 30-70˚C for different times were obtained from STEM images as shown in Fig. 4.19. A thin layer of precipitates was found at the grain boundary of Al 5083 H116 sample aged for 6 months (see Fig. 4.19 (a)). Thicker and discontinuous precipitates were observed in the 8 months' sample, as shown in Fig. 4.19 (b). When aging time increases to 10 months, the intergranular precipitates become continuous, Fig. 4.19 (c).

4.4 APT results of Al 5083 H116

Mg-rich precipitates were very difficult to reveal using STEM-EDS for Al 5083 H116 aged at 50℃ for 9 and 24 months, and thus APT was applied as a complementary

technique due to the enhanced chemical sensitivity of APT compared to STEM-EDS. Fig. 4.20(a) displays a 3D reconstruction of an analyzed volume containing ~1.1×10^7 atoms from the Al 5083 H116 sample aged at 50°C for 24 months, and the results (Fig. 4.20(a)) indicate this sample consists of two phases and a phase boundary. The 3D atom maps of all elements in the material are displayed in Fig. 4.20(a). The top region of the APT needle is rich in Al and Mg, which is the matrix of Al 5083 H116 alloy. While the bottom region of the APT needle is composed of Al, Mn, Fe, and Cr with a composition that corresponds to Al_6(Mn,Fe,Cr)-type pre-existing particle as observed in STEM EDS results above. Fig. 4.20(b) and (c) illustrates the 3D morphology of Mg-rich precipitates, which were delineated by 10 at.% Mg isoconcentration surfaces. Moreover, a 5 at.% Mn isoconcentration surface was added to highlight the position of pre-existing particle-matrix interface. Mg-rich precipitates were found in the matrix as well as on the pre-existing particle. Six Mg-rich precipitates of oblate ellipsoid morphology are observed in the matrix, and the magnified views of three precipitates are shown in Fig. 4.20 (d). The size of these precipitates ranges from 2.5 to 6.5 nm (in radius). However, the morphology of precipitates formed on the pre-existing particle are lamellar (see Fig. 4.20 (e)). The thickness of these lamellar precipitates is less than 2 nm, and the length of them varies from 1 nm to 15 nm. The number density of precipitates formed on the pre-existing particle is almost five times that for precipitates nucleated in the matrix, which could be attributed to the lower energy barrier needed for heterogeneous nucleation. [84]

Fig. 4.21 (a) illustrates the line scan results of an Mg-rich precipitate formed in the matrix, as shown in Fig. 4.20(d) (indicated by an arrow). Mg concentration of the precipitate is around 18.3 at.%, which is even lower than the reported concentration of GP

zones (19 at.%). [27] Therefore, these precipitates could be GP zones. Mg concentration of one of the lamellar precipitates (see Fig. 4.20(b) and (e)) formed on the pre-existing particle is shown in Fig. 4.21 (b), and a higher Mg concentration, 24.8 at.% (average along the thickness direction), is detected. *β*" phase is reported to have a stoichiometry of Al_3Mg, [32] which is very close to the Mg concentration (24.8 at.%) of precipitates in Fig. 4.20(e). Thus, precipitates formed on pre-existing particles are most likely to be *β*" phases.

4.5 Small angle neutron scattering results of Al 5xxx alloys

Fig. 4.22 displays the scattering cross-section of Al 5083 H131 and H116 alloys in the as-quenched and differently aged states. For both Al 5083 H131 and H116, the as-quenched sample shows the lowest scattering intensity, and the scattering intensity decreases with increasing scattering vector (*q*). After aging at 70℃ for 1.5 months, a considerable increase in scattering intensity was observed for the Al 5083 H131 alloy sample. A further increase in scattering intensity was identified for Al 5083 H131 aged at 70℃ for 9 months. However, the scattering intensity of Al 5083 H131 alloy starts to decrease beyond 9 months in spite of the increase in aging time (18 and 30 months). In addition, the scattering intensity of the 30 months' sample is even slightly lower than that of the 1.5 months' sample. The scattering intensity results of Al 5083 H116 alloy aged at 70℃ also experienced similar kinetics as Al 5083 H131 samples (increases first and then decreases), whereas the highest scattering results were achieved at 18 months, which is 9 months later than the Al 5083 H131 sample. The SANS results of the Al 5083 H116 sample aged at 50℃ are shown in Fig. 4.22 (c). Even though the scattering intensity increase is

not large, a clear increasing trend can still be observed from 9 months to 41 months (see the inserted image in Fig. 4.22 (c)).

Fig. 4.23 compares the SANS results for the AQ, navy ship sample, and Al 5456 H116 sample aged at 70℃ for 30 months. For q<0.02 Å^{-1}, there is little change in scattering intensity for these three samples. The scattering intensity of the 30 months sample is larger than that of the navy ship sample and the AQ sample for 0.02<q<0.09 Å^{-1}. When 0.09<q<0.8 Å^{-1}, only the navy ship sample has scattering intensity observable above background.

The SANS experimental results were fitted using the two-phase model of isolated particles in a homogeneous matrix [25]. The difference in scattering length densities $\Delta\eta$ is given by

$$\Delta\eta = \left|\eta_p - \eta_m\right| = \left|\sum x_i^p b_i / v_i - \sum x_i^m b_i / v_i\right| \tag{4.3}$$

where η_p and η_m are the average scattering length density of the precipitate and the matrix, b is the scattering length of individual elements, x is the atomic fraction, and the atomic volume is denoted by v. The coherent scattering length of Al and Mg are 0.3449×10^{-12} cm and 0.5375×10^{-12} cm, respectively [144]. During the fitting of SANS results, a constant $\Delta\eta$ was assumed at first. However, the scattering intensities of Al 5083 H131 (70℃) keep increasing with aging time, as shown by the dashed lines in Fig. 4.22 (a). Therefore, a variable $\Delta\eta$ must be applied to explain the decrease in scatting intensities of Al 5083 H131 and H116 aged at 70℃.

The Mg concentration of precipitates in Al 5083 H131 and H116 aged at different temperatures for different times obtained from STEM-EDS and APT are shown in Fig. 4.23. Mg concentrations of the precipitates are found to increase with aging time. For example, when aged at 70°C, the average Mg concentration (shown as diamonds in Fig. 4.23) of precipitates in the 1.5 months' Al 5083 H131 alloy sample is only 14.1 at.% , while it increases to 32.3 at.% in the 30 months' sample. The concentrations of Mg for GP zones, β", β', and β phases are shown in Table 4.3. The increase of average Mg concentration indicates the phase transformation from GP zones to β'/β phase. The corresponding scattering length density, η, calculated using Eq. (4.3), is also listed in Table 4.3. From GP zone to β" phase, $\Delta\eta$ increases, while from β" phase to β' and β phase it decreases.

STEM and APT, as complementary techniques, provide valuable information for the quantitative analysis of SANS results. Based on STEM and APT results, the shape of the Mg-rich precipitate is ellipsoid, with two semimajor axes of length R, and one semiminor axis of length (uR), where u is the aspect ratio. The values of u for Al 5083 H131 and H116 are 0.3 and 0.5, respectively. The aspect ratio is equal to 0.6 for Al 5456 H116 30 months' sample, and 0.23 for the navy ship sample based on statistical results from STEM images.

The modeling results of SANS (solid lines) are shown in Fig. 4.22 (for Al 5083 H131 and H116) and 4.23 (for Al 5456 H116 and the navy ship sample), which agree well with experimental results. The χ^2-test results of the navy ship sample are also inserted in Fig. 4.23, indicating a good agreement ($\sum\chi^2$=1.3) between the experimental and modeling results. Moreover, the scattering intensity results of the AQ samples (both Al 5083 H131, H116, and Al 5456 H116) show a linear relationship with q^{-4}, which is also known as the Porod law. [145] This relationship could be explained by scattering caused by the sharp

interface between Al_6Mn-type pre-existing particles and the matrix. The results of SANS experiments are summarized in Table 4.4. Both radius and volume fraction of Mg-rich precipitates increase with aging time, which is consistent with the STEM results. In addition, for Al 5083 H131 and H116 aged at 70℃ for 30 months, the precipitate radius in Al 5083 H131 is larger than that in the H116 sample. Despite the relatively long aging time (41 months) at 50℃, the average radius of precipitates is much smaller than that of Al 5083 H116 aged at 70℃ for 30 months. The number density of precipitates decreases with aging time, suggesting coarsening happens in both alloys, Table 4.4.

The volume fraction distribution of precipitates obtained from SANS is shown in Fig. 4.25. The total precipitate volume fraction in Al 5456 H116 30 months' sample is 1.39%, which is much larger than that (0.36%) of the navy ship sample. In addition, the average precipitate radius in the Al 5456 H116 30 months' sample is 18.5 nm, whereas the size of precipitates formed in the navy ship sample (at the triple junction of grain boundaries, grain boundaries, and on pre-existing particles) is only 13 nm, as shown in the inserted image of Fig. 4.25. The average precipitate radii obtained from STEM images are also shown in the inserted image of Fig. 4.25. The average radius obtained from SANS is slightly larger than that obtained from STEM for both Al 5456 H116 30 months' sample (16.4 nm) and the navy ship sample (12 nm); the difference can be due to the low Z-contrast of Al and Mg atoms, which makes it hard to identify the Mg-rich phase of low Mg concentration formed at the edge of each precipitate for STEM.

Table 4.1 Size (nm) and aspect ratio of Mg-rich precipitates formed in Al 5083 H131 and H116 alloys aged at different temperatures for different times as measured using STEM.

Aging time	Al 5083 H131 (70°C)	Al 5083 H116 (70°C)	Al 5083 H116 (50°C)
1.5 mo	6.4±2.6		
3 mo		6.8±3.1	
9 mo	16.6±5.5	10.1±4.8	
18 mo	21.1±6.2	11.8±4.1	
24 mo			8.2±1.8
30 mo	25.2±8.3	18.6±5.2	
41 mo			13.5 ± 3.7
Aspect ratio	0.3	0.5	0.5

Table 4.2 Average and peak Mg concentration of intragranular precipitates in Fig. 4.15(a) and (d).

	Mg concentration (Talos)		Mg concentration (JEM)	
	Average (wt.%)	Peak (wt.%)	Average (wt.%)	Peak (wt.%)
1	29.5±3.7	33.9	26.7±4.9	31.8
2	15.6±1.5	17.7	14.9±1.86	17.8
3	25.0±3.7	33.0	23.4±3.3	30.8
4	10.6±0.7	12.3	10.4±1.1	12.2
5	27.8±2.7	32.4	24.8±6.4	32.3

Table 4.3 Mg concentration and scattering length density of different phases in Al 5083 alloy.

	Mg concentration (at.%)	Scattering length density, η ($\times 10^{10}$ cm^{-2})
matrix	5.25	2.14
GP zone	15	2.23
β"(Al_3Mg, $L1_2$)	25	2.31
β'(Al_3Mg_2, hcp)	40	2.18
β (Al_3Mg_2, fcc)	40	2.18

Table 4.4 Radius, number density, and volume fraction of Mg-rich precipitates obtained from SANS.

	Aging time/(month)	Radius (nm)	Number density (/m^3)	Volume fraction (%)
Al 5083 H131-70℃	1.5	7.5±2.5	1.9E21	0.06±0.015
	9	10±3.3	8.4E20	0.1±0.03
	18	15.5±5.1	4.0E20	0.28±0.08
	30	21.5±6.3	3.1E20	0.6±0.15
Al 5083 H116-70℃	3	6.8±2.1	1.6E21	0.034±0.01
	9	11.0±2.6	7.5E20	0.1±0.035
	18	13.8±3	3.1E20	0.13±0.04
	30	17.5±4	2.3E20	0.27±0.08
Al 5083 H116-50℃	9	7±1.8	8.7E20	0.02±0.005
	24	8.5±2.3	4.0E20	0.027±0.01
	41	13±3.1	2.2E20	0.091±0.029

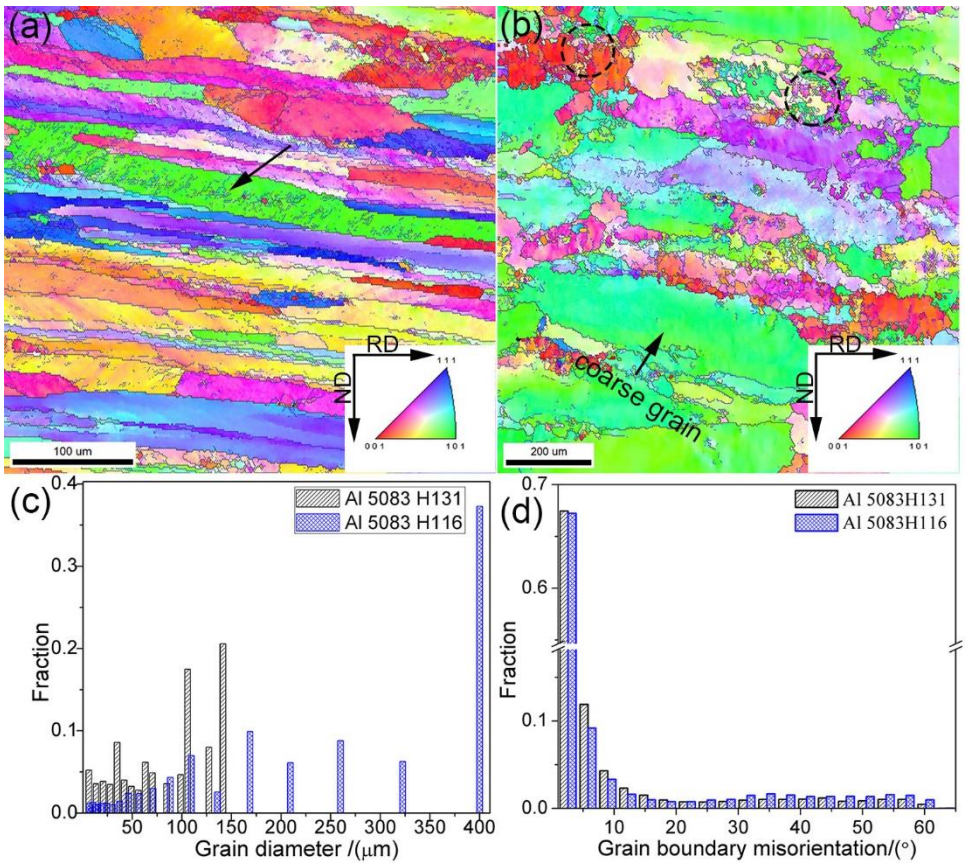

Figure 4.1 EBSD inverse pole figure (IPF) maps of (a) Al 5083 H131 and (b) Al 5083 H116, (c) grain size distribution of Al 5083 H131 and Al 5083 H116, and (d) grain boundary misorientation of Al 5083 H131 and Al 5083 H116.

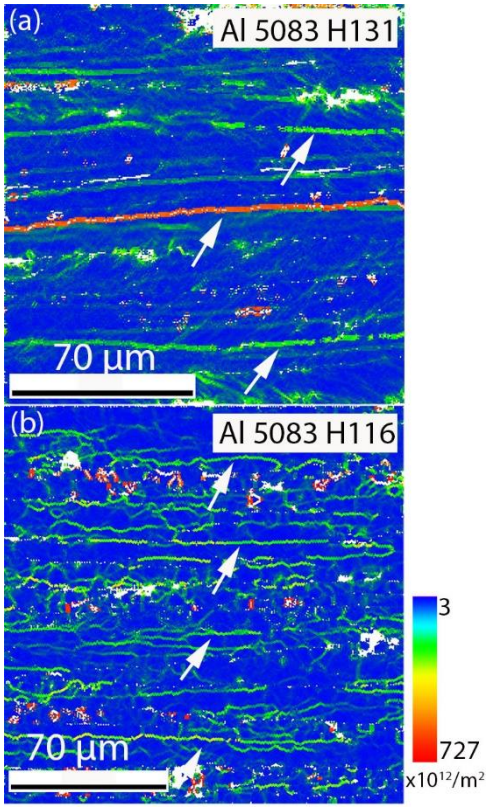

Figure 4.2 Geometrically necessary dislocation density maps of as-received (a) Al 5083 H131 and (b) Al 5083 H116 alloy.

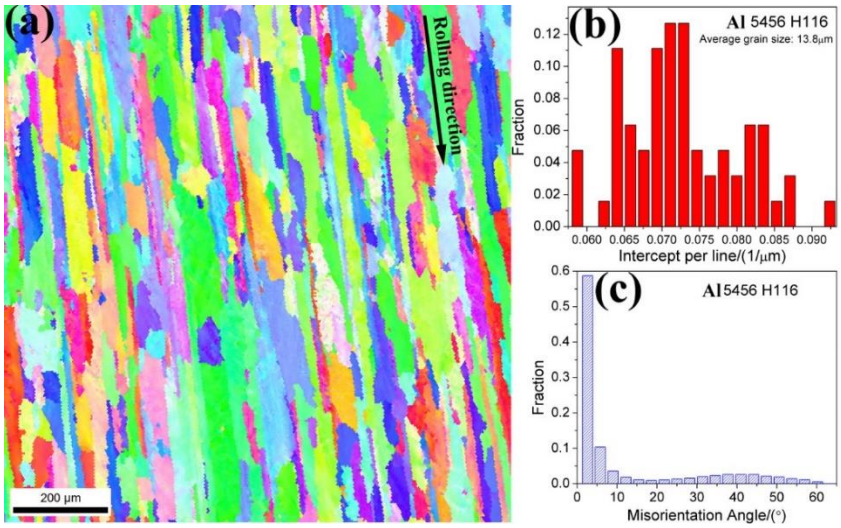

Figure 4.3 EBSD inverse pole figure (IPF) maps of (a) Al 5456 H116, (b) grain size distribution of Al 5456 H116 obtained from the intercept per line method, and (c) grain boundary misorientation angle distribution results of Al 5456 H116.

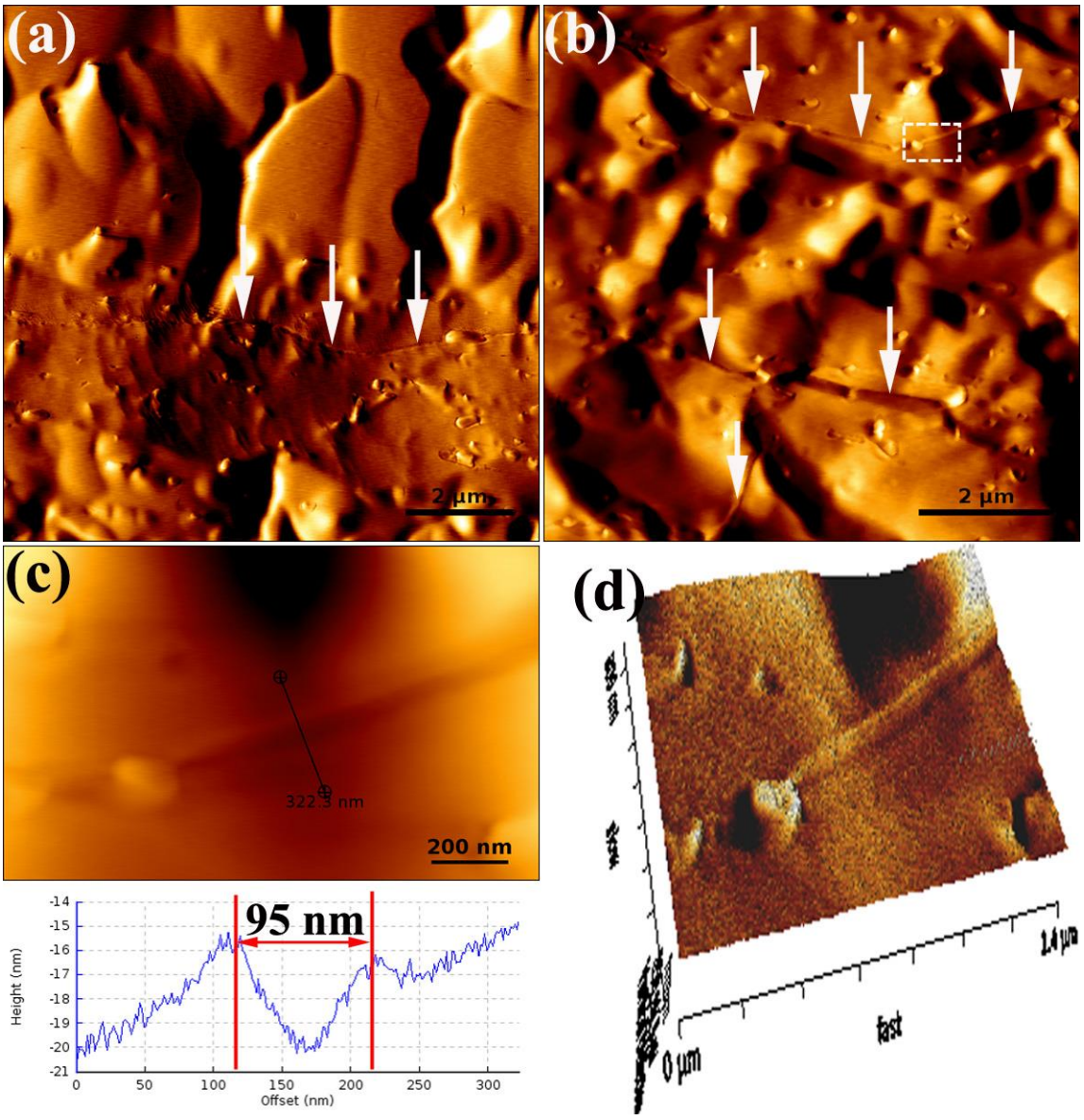

Figure 4.4 AFM results of Al 5083 H131 aged at 70°C for 30 months (a) and (b) vertical trace image, (c) height trace image of the area within the dash frame in (b) and the height distribution along the line scan, (d) 3D image of (c).

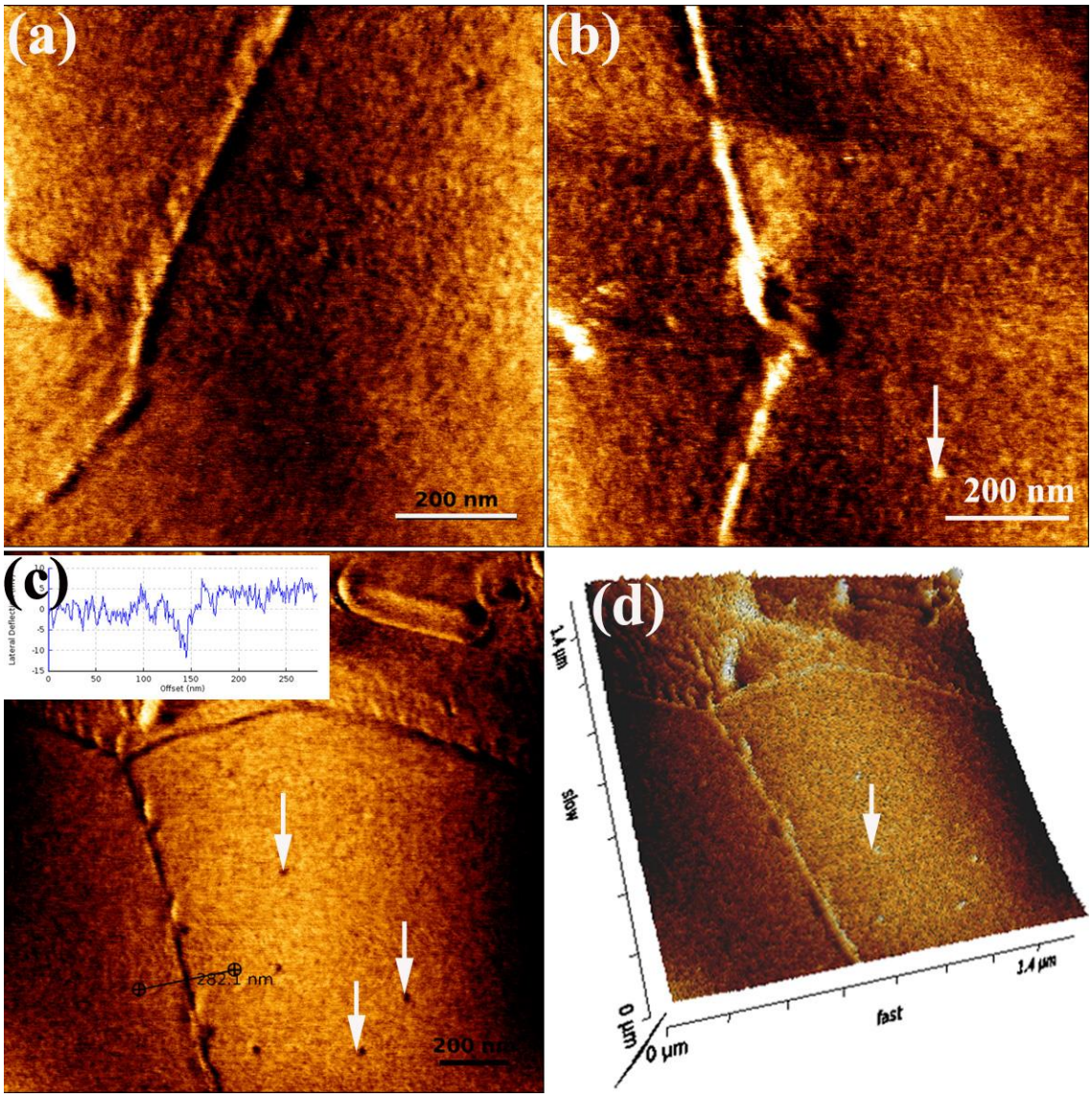

Figure 4.5 AFM results of Al 5456 H116 aged at 50°C for 18 months (a) vertical and (b) horizontal trace image, (c) and (d) vertical and 3D image of a triple junction of three grain boundaries.

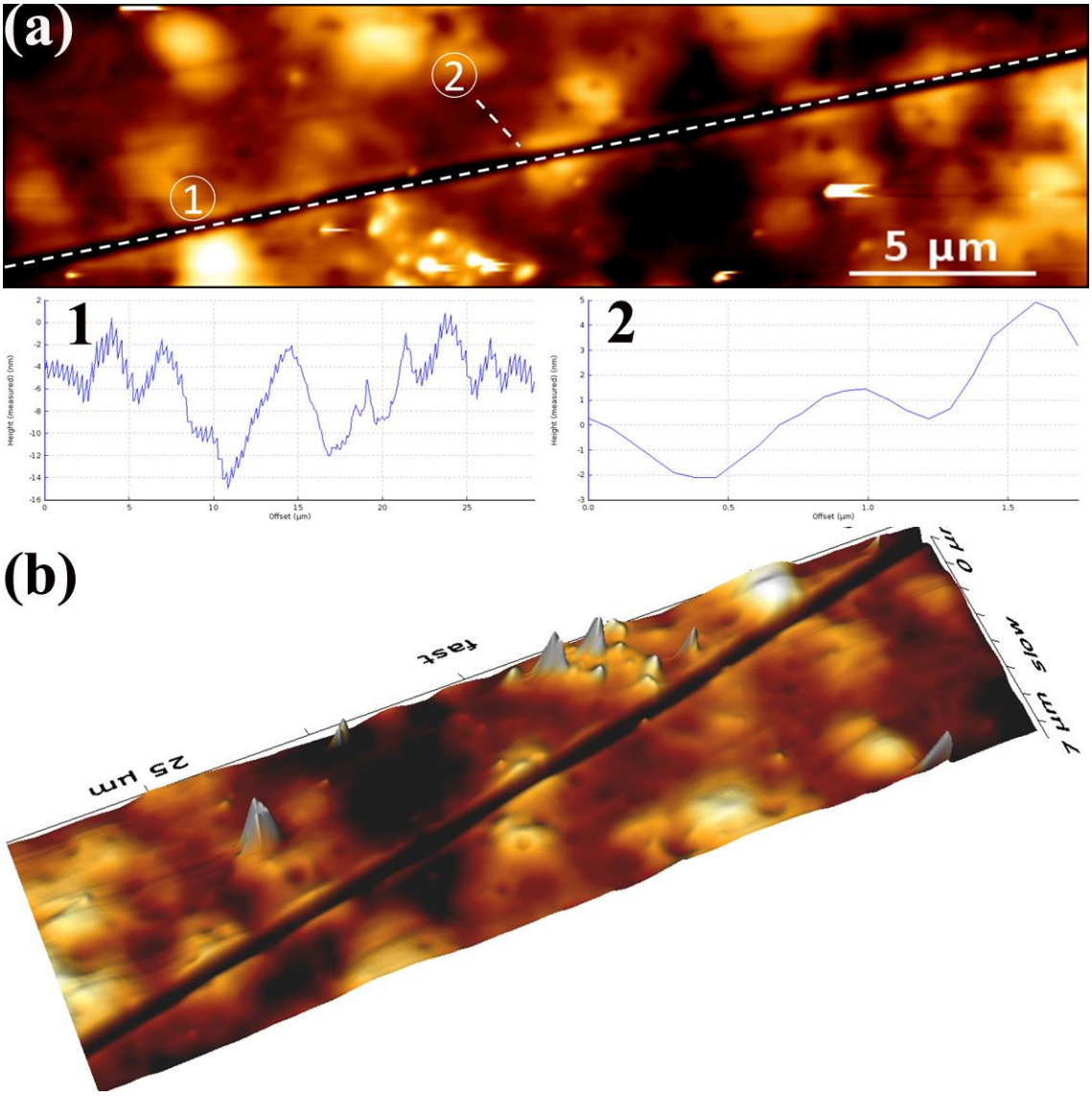

Figure. 4.6 AFM results of Al 5083 H131 aged at 70℃ for 30 months (a) height trace image (tapping mode) of a grain boundary and height distribution along line scan 1 and 2, (b) 3D image of (a).

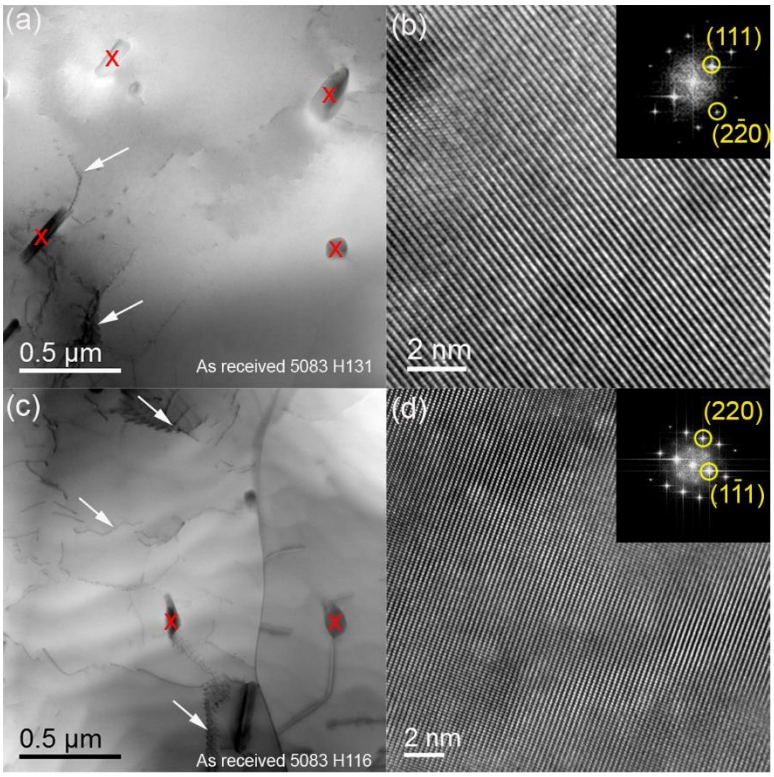

Figure 4.7 BF-STEM images of the as received (a) Al 5083 H131 and (c) Al 5083 H116 sample. High resolution TEM images of (b) Al 5083 H131 and (d) Al 5083 H116, and the corresponding fast Fourier transform (FFT) patterns (inserted).

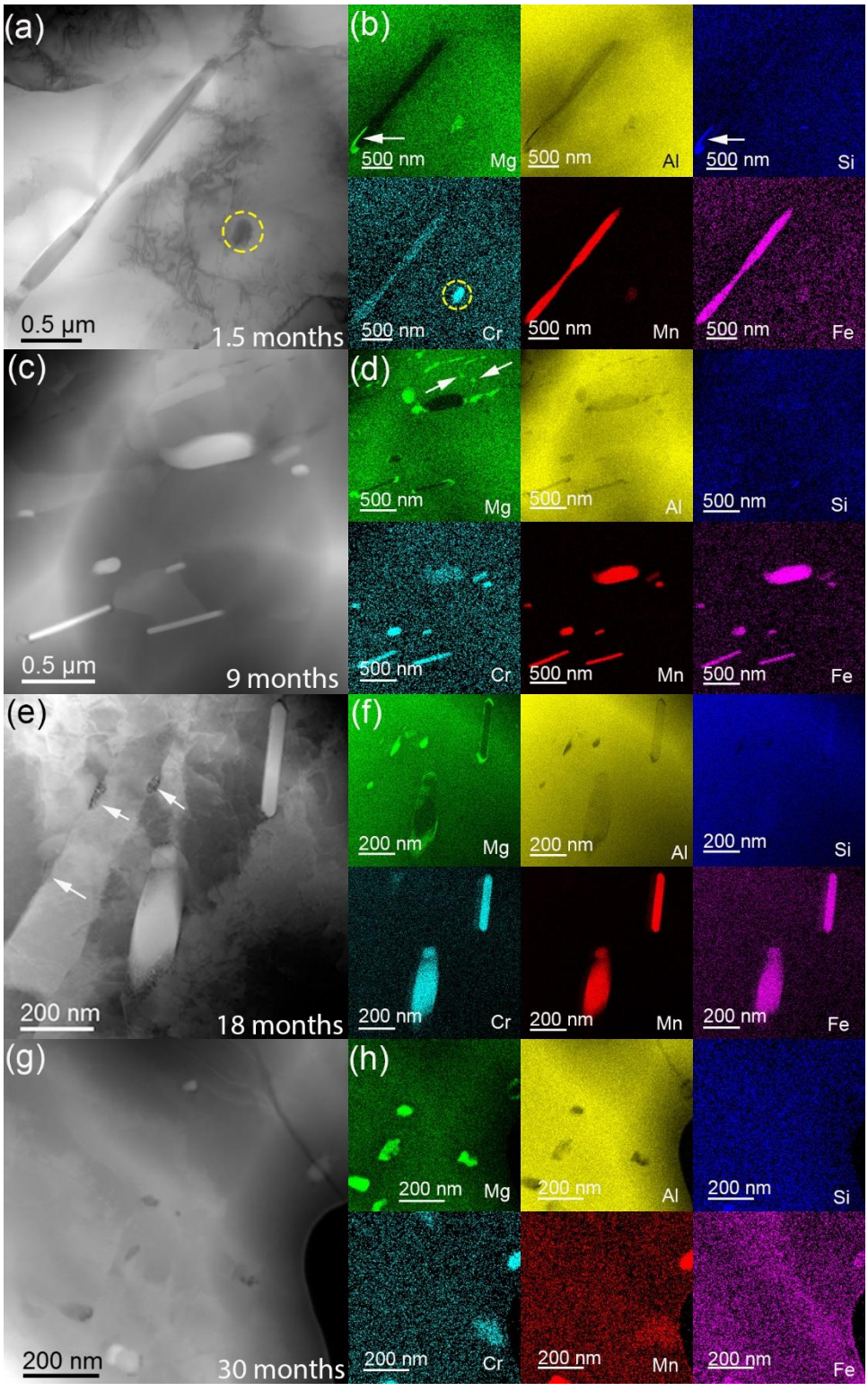

Figure 4.8 BF-STEM images of Al 5083 H131 aged at 70°C for (a) 1.5 months, and DF-STEM image of Al 5083 H131 aged at 70°C for (c) 9 months, (e) 18 months, and (g) 30 months, and the corresponding EDS maps for the (b) 1.5 months, (d) 9 months, (f) 18 months, and (h) 30 months samples.

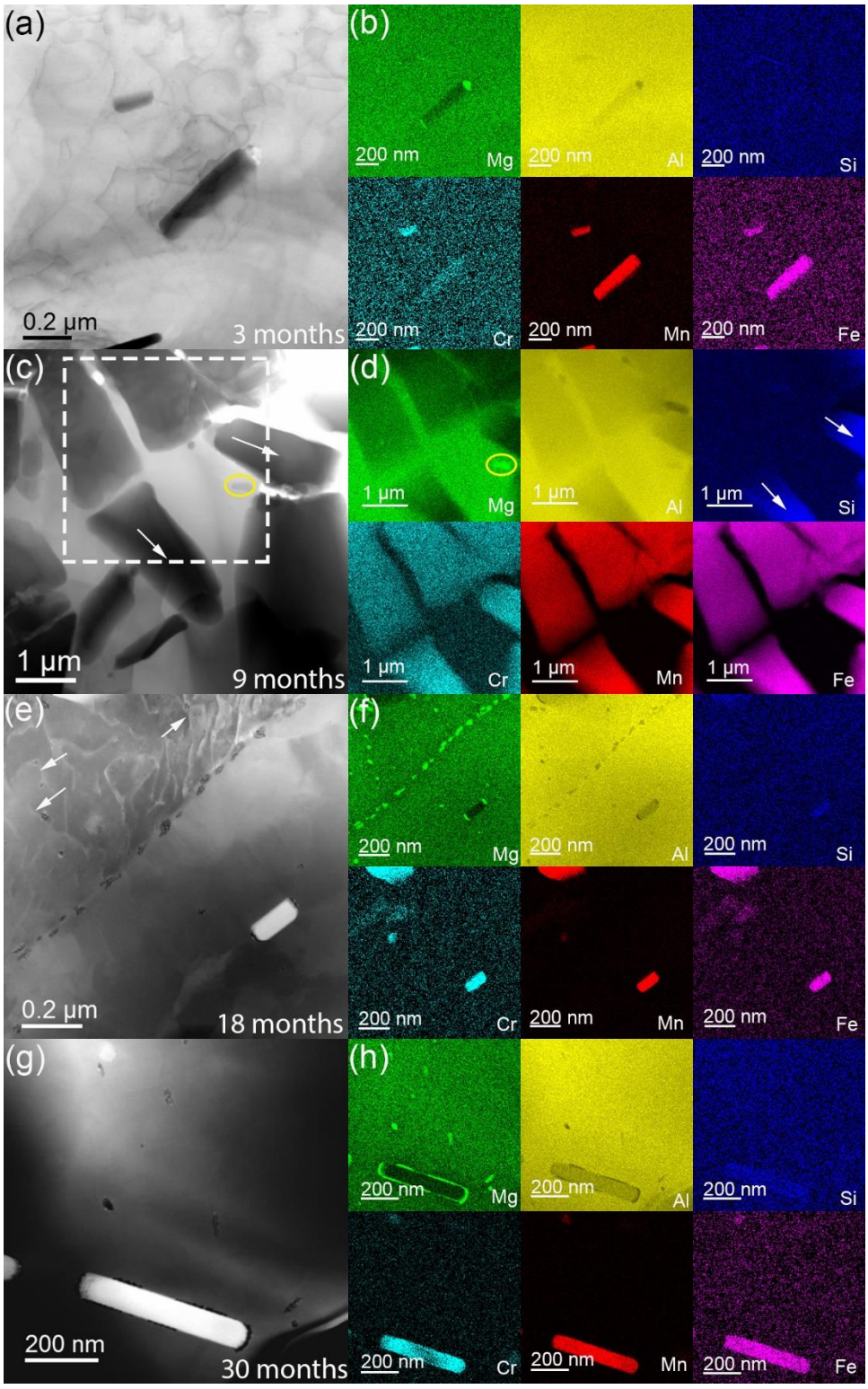

Figure 4.9 BF-STEM images of Al 5083 H116 aged at 70℃ for (a) 3 months and (c) 9 months, and the DF-STEM images of Al 5083 H116 aged at 70℃ for (e) 18 months and (g) 30 months, and the corresponding EDS maps for the (b) 3 months, (d) 9 months (the area within the dash frame of (c)), (f) 18 months, and (h) 30 months samples.

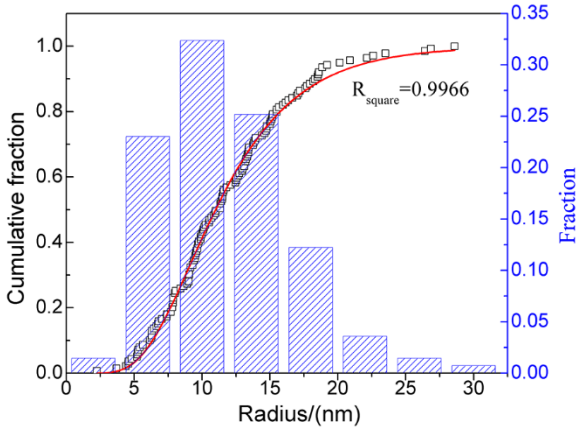

Figure 4.10 Size distribution and the cumulative log-normal fitting of Mg-rich precipitates formed in Al 5083 H116 alloy aged at 70℃ for 18 months.

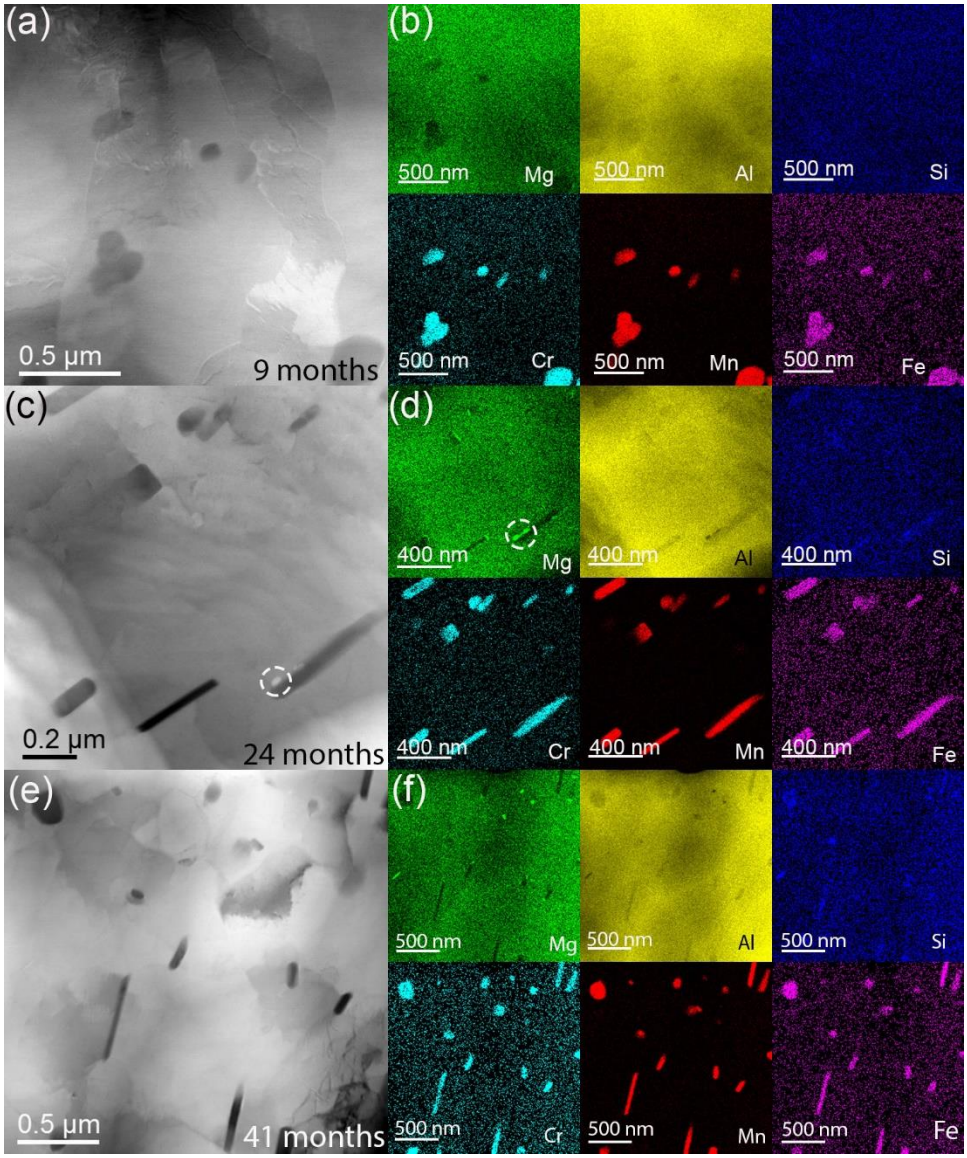

Figure 4.11 BF-STEM images of Al 5083 H116 aged at 50℃ for (a) 9 months, (c) 24 months, and (e) 41 months, and the corresponding EDS maps for the (b) 9 months, (d) 24 months, and (f) 41 months sample.

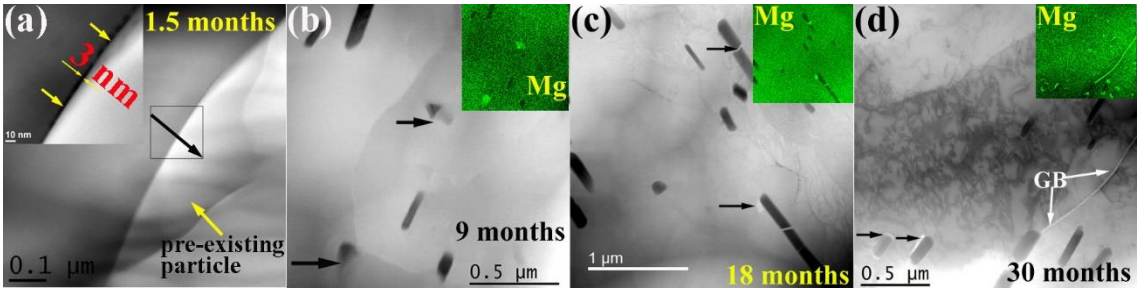

Figure 4.12 BF-STEM images of Al 5456 H116 aged at 70℃ for (a) 1.5 months, (b) 9 months, (c) 18 months, and (d) 30 months. Fig. (a) is obtained using Hitachi HF-3300 S/TEM, and Fig. (b)-(d) are obtained using JEM 2800. The inserted image in (a) is a high-angle annular dark-field (HAADF) image of the area within the square frame, and the corresponding STEM-EDS line scan results (indicated by the arrow in the frame) are shown in Appendix A.1. EDS mapping results of Mg for (b), (c), and (d) have been inserted, and the position of Mg rich precipitates and the grain boundary has been highlighted by arrows.

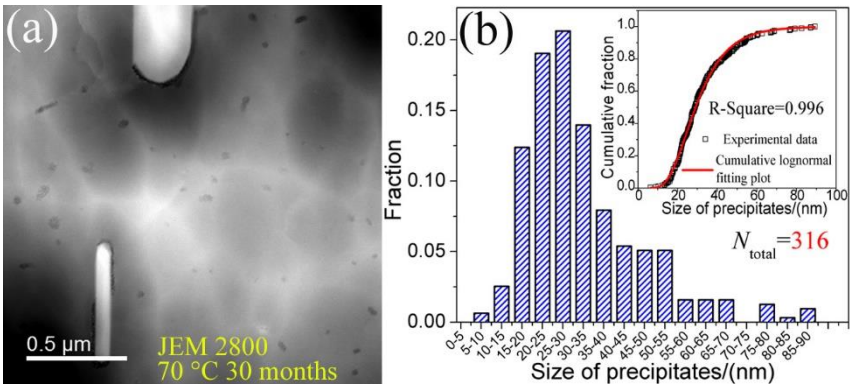

Figure 4.13 STEM results of precipitates formed in Al 5456 H116 aged at 70℃ for 30 months (a) HAADF-STEM image of the grain matrix obtained from JEM 2800, and (b) size distribution of intragranular Mg rich precipitates in Al 5456 H116 aged at 70℃ for 30 months.

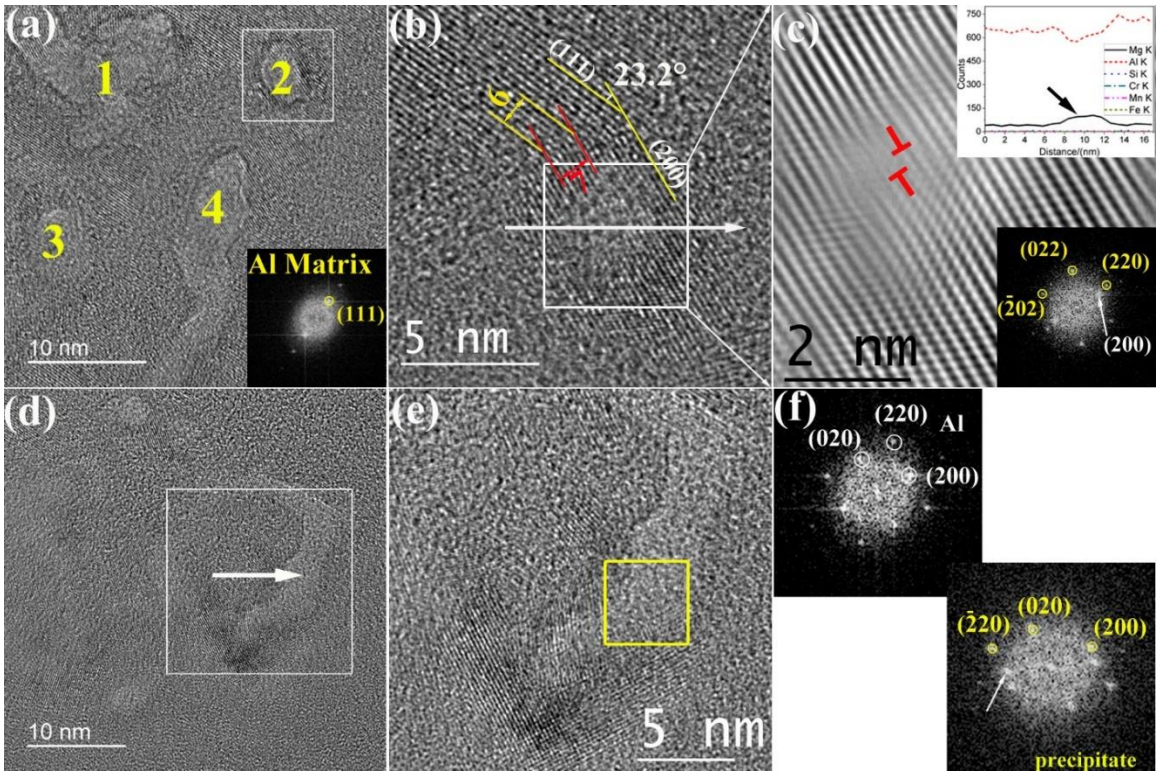

Figure 4.14 TEM results of Al 5456 H116 aged at 70°C for 30 months (a) TEM image of 4 intragranular Mg-rich precipitates formed in the matrix obtained from JEM 2800, the inserted image is the FFT of Al matrix, (b) High resolution TEM image of precipitate 2 as highlighted in (a), (c) Inverse FFT results of the area within the frame of (b), the inserted images are the EDS line scan results across the precipitate as highlighted by the arrow in (b) and the FFT of the Mg-rich precipitate, (d) TEM image of some other Mg-rich precipitates formed in the matrix of Al 5456 H116 aged at 70°C for 30 months, (e) TEM image of the precipitate within the frame of (d), and (f) the FFT results of Al matrix the area within the frame in (e).

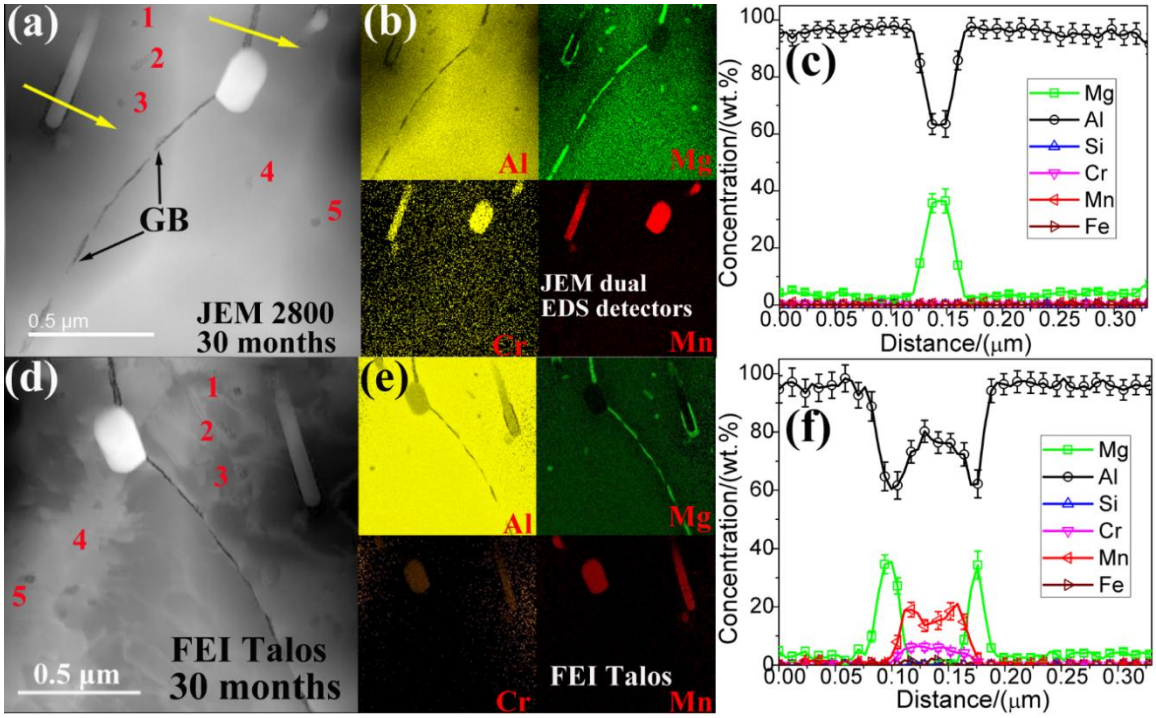

Figure 4.15 STEM and EDS results of Al 5456 H116 aged at 70℃ for 30 months (a) HAADF-STEM image of a grain boundary obtained from JEM 2800, (b) EDS mapping results of (a) obtained from the ultrafast EDS system of JEM 2800, (c) EDS line scan results across the grain boundary as indicated by arrows in (a). (d) HAADF-STEM image of the same area in (a) obtained from FEI Talos F200X, (e) EDS mapping results of (d) obtained from Talos, and (f) EDS line scan results across the pre-existing particle as indicated by arrows in (a). There are 5 intragranular precipitates identified by numbers in (a) and (d), and the corresponding EDS line scan results obtained from JEM ultrafast EDS system and FEI Talos F200X are shown in Fig. Appendix A.3.

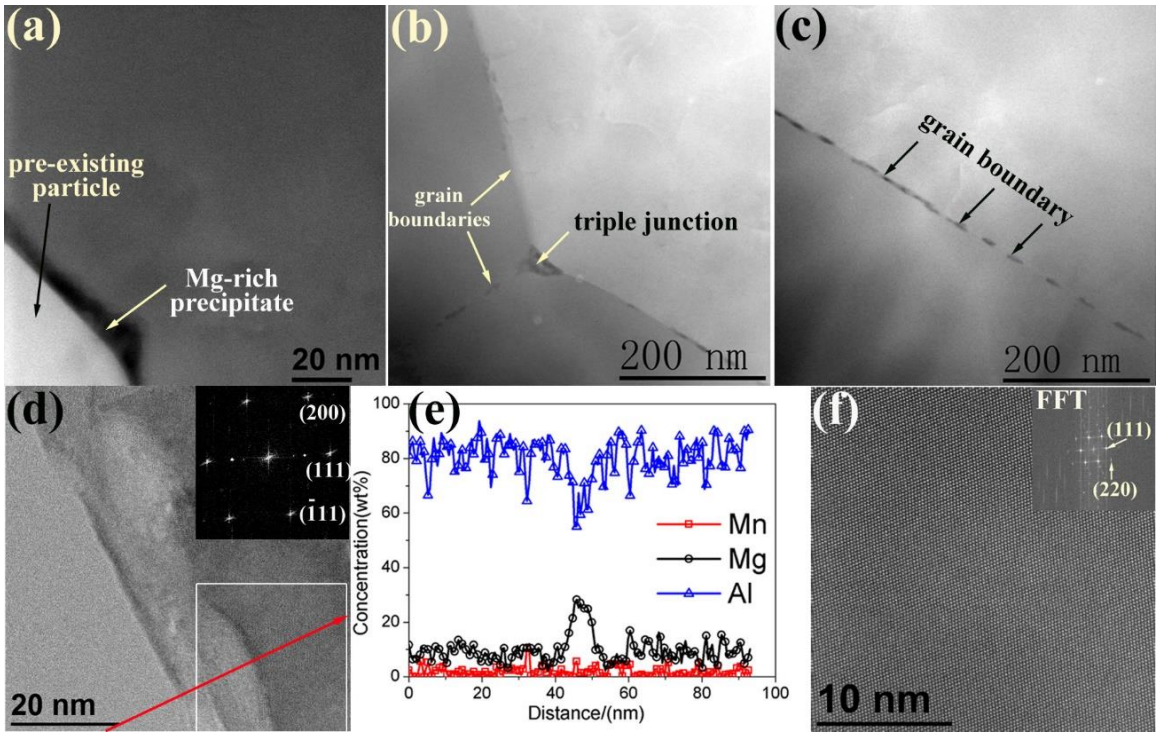

Figure 4.16 HAADF-STEM images of Mg-rich precipitates formed (a) at pre-existing particle, (b) triple junction of grain boundaries, (c) grain boundary of the navy ship sample, (d) HAADF-STEM image of two precipitates formed at the grain boundary of the navy ship sample, inserted images shows the FFT of the precipitate within the frame of (d), (e) EDS line scan results of the precipitate in (d) (as highlighted by an arrow), and (f) high resolution STEM image and the corresponding FFT pattern of the Navy ship sample. All the images are obtained using the JEM-2200FS S/TEM.

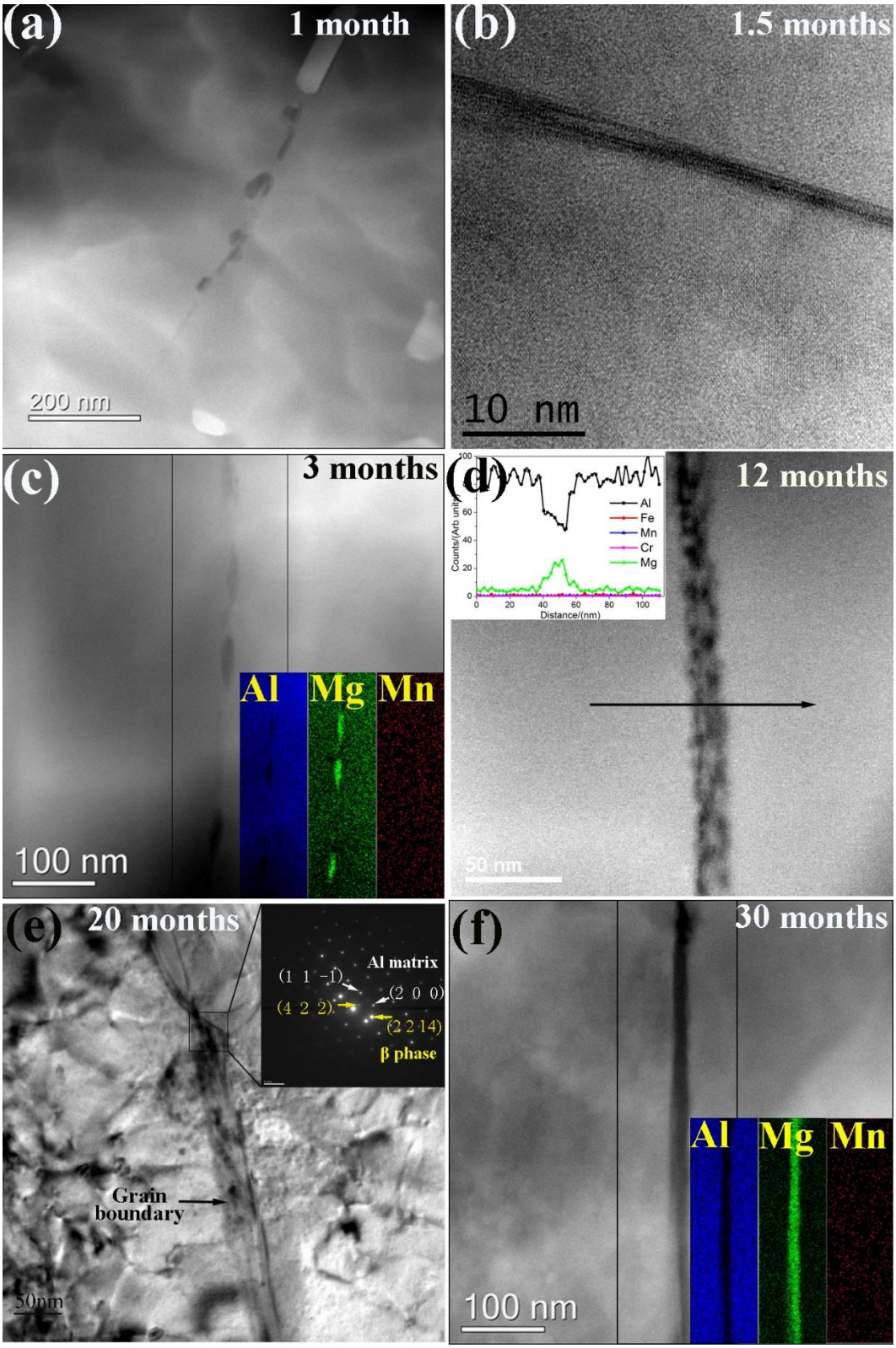

Figure 4.17 DF-STEM image of β phase formed at the grain boundary of Al 5083 aged for different times (a) 1 month, (b) 1.5months, (c) 3 months, (d) 12 months, (e) 20 months and (f) 30 months.

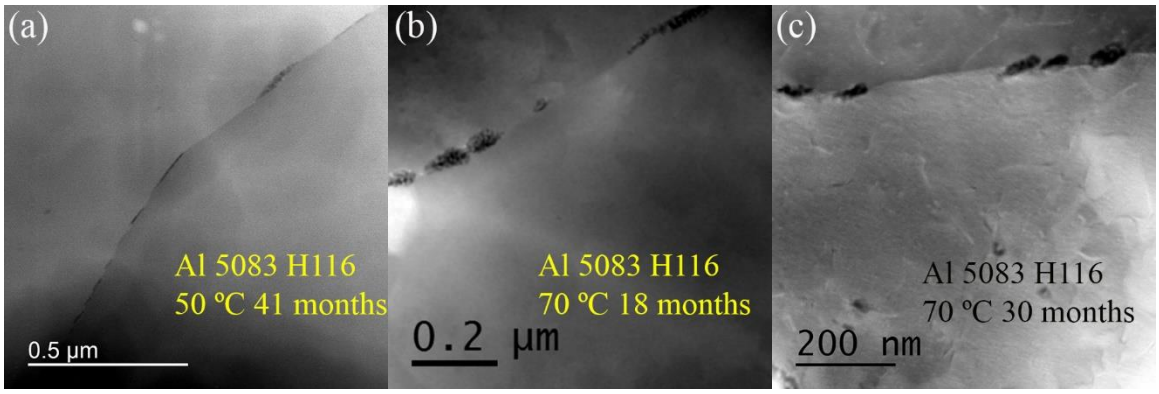

Figure 4.18 STEM results of Al 5083 H116 (a) DF-STEM image of Al 5083 H116 aged at (d) 50℃ for 41 months, (b) 70℃ for 18 months and (c) 30 months.

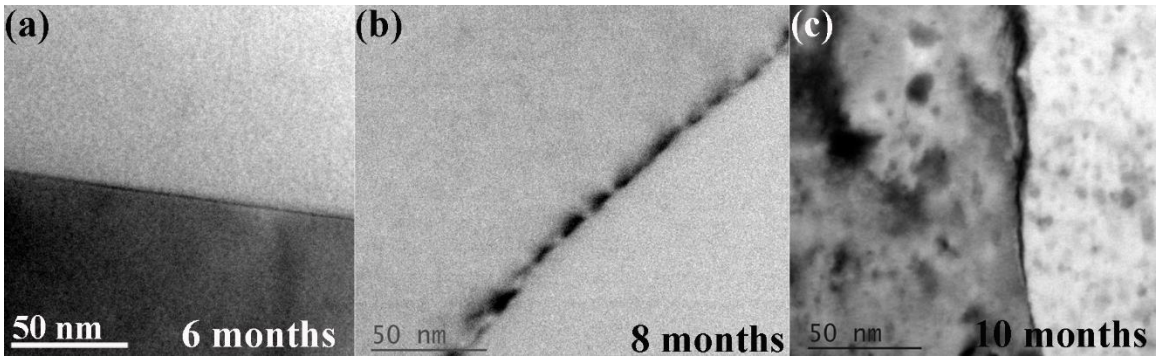

Figure 4.19 DF-STEM image of Al 5083 H131 aged at 30-70℃ for (a) 6 months, (b) 8 months, and (c) 10 months.

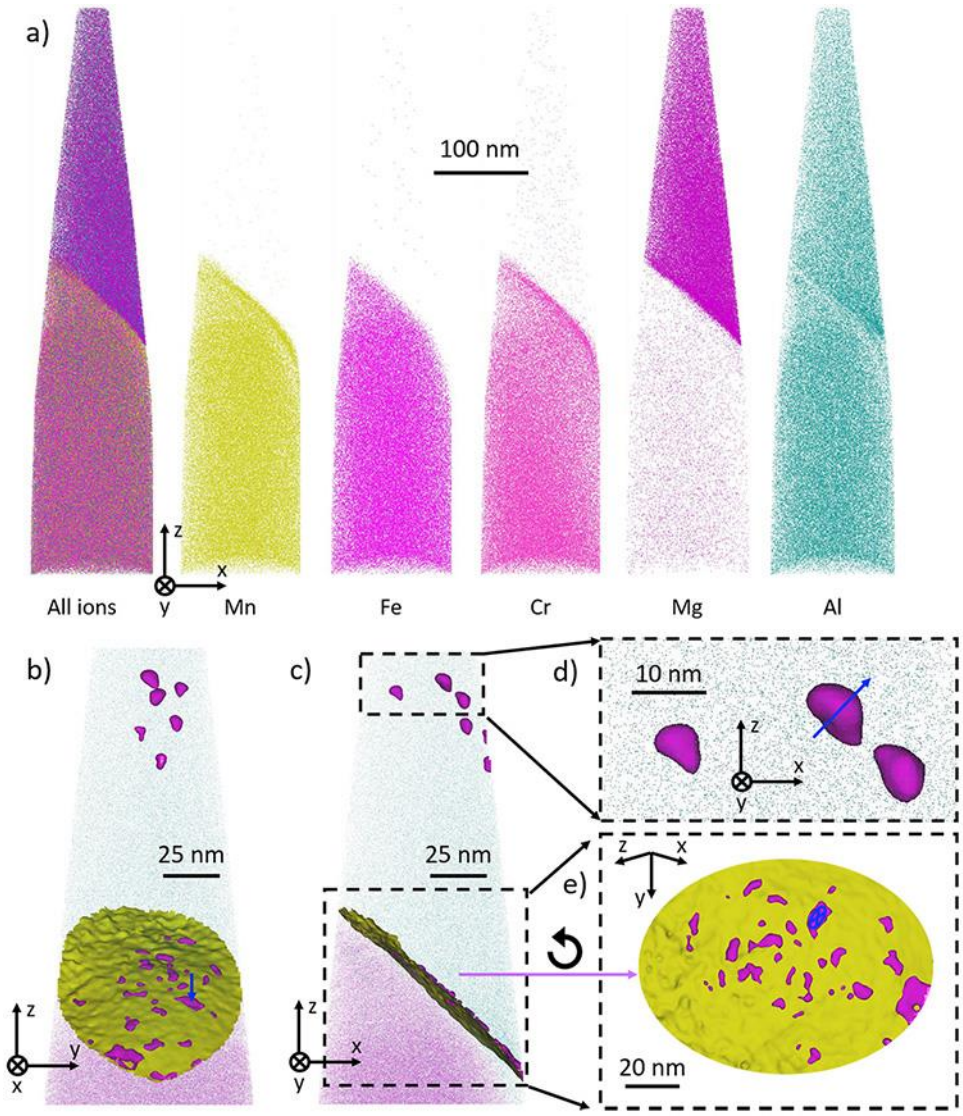

Figure 4.20 APT results of Al 5083 H116 aged at 50°C for 24 months (a) APT atom maps for all elements, Mn, Fe, Cr, Mg, and Al (b) A magnified region of the APT needle with a 5 at. % Mn isosurface (yellow) defining the matrix/precipitate interface and 10 at.% Mg isosurfaces (purple) showing Mg rich precipitates within the matrix and at the matrix/precipitate interface. Al and Fe atoms are also displayed. The blue arrow indicates the region of the 1D line profile shown in Figure 4.21(b). (c) A 90° rotation of (b). (d) A magnified view of the Mg precipitates within the Al-Mg matrix. The blue arrow indicates the direction of the 1D line profile shown in Figure 4.21(a). (e) A magnified and rotated view of the matrix/precipitate interface showing the Mg rich precipitates formation on the interface. A blue x indicates the z-direction of the 1D line profile shown in Figure 4.21(b).

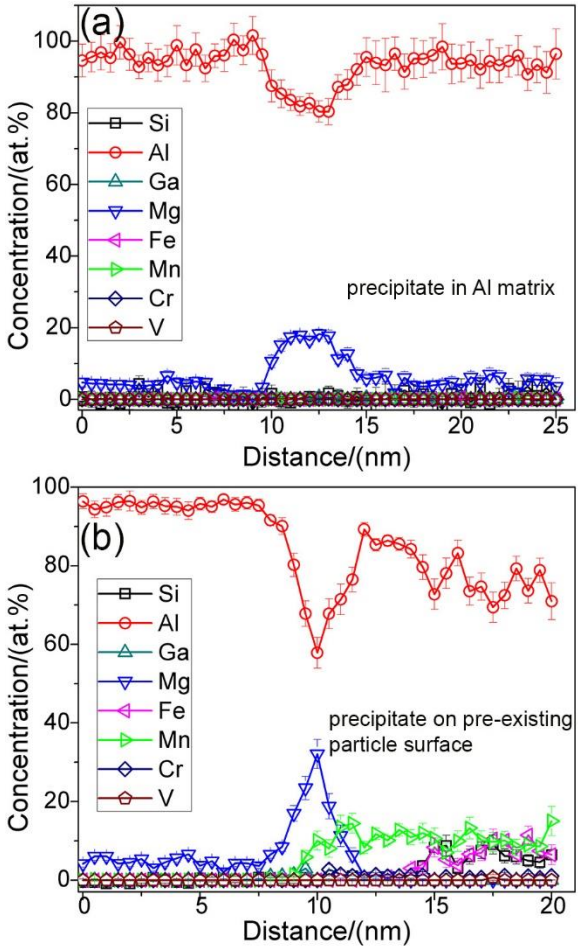

Figure 4.21 APT line scan results of Mg-rich precipitates formed (a) in the matrix (identified by an arrow in Figure 4.20(d)) and (b) on the matrix-pre-existing particle interface (highlighted by an arrow in Figure 4.20(e)) of Al 5083 H116 aged at 50°C for 24 months.

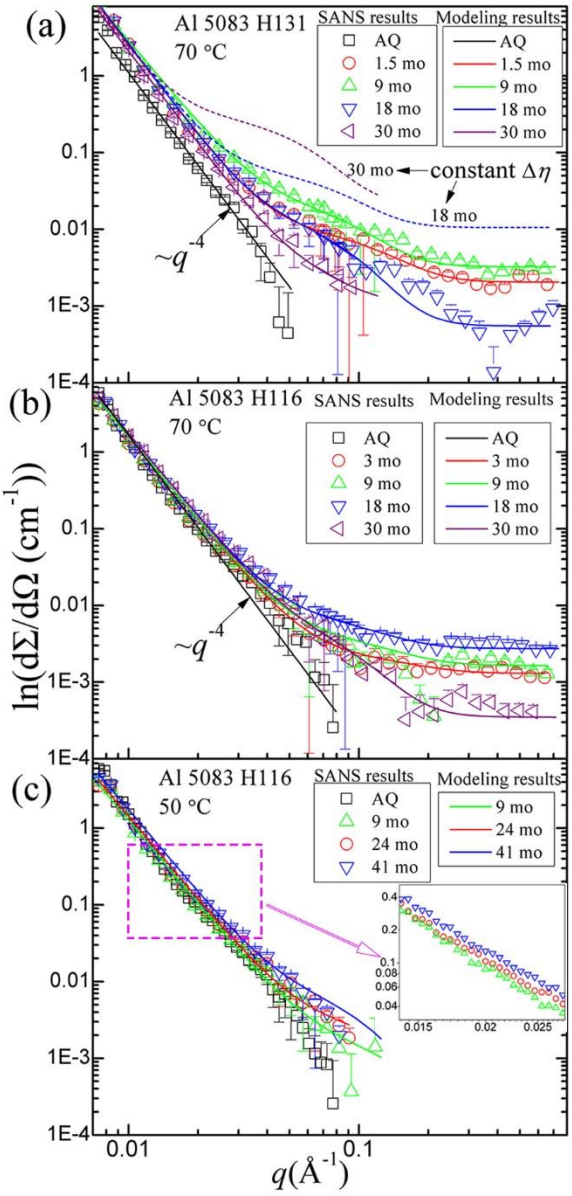

Figure 4.22 SANS results of Al 5083 H131 alloy aged at (a) 70℃ and Al 5083 H116 aged at (b) 70℃ and (c) 50℃ for different times.

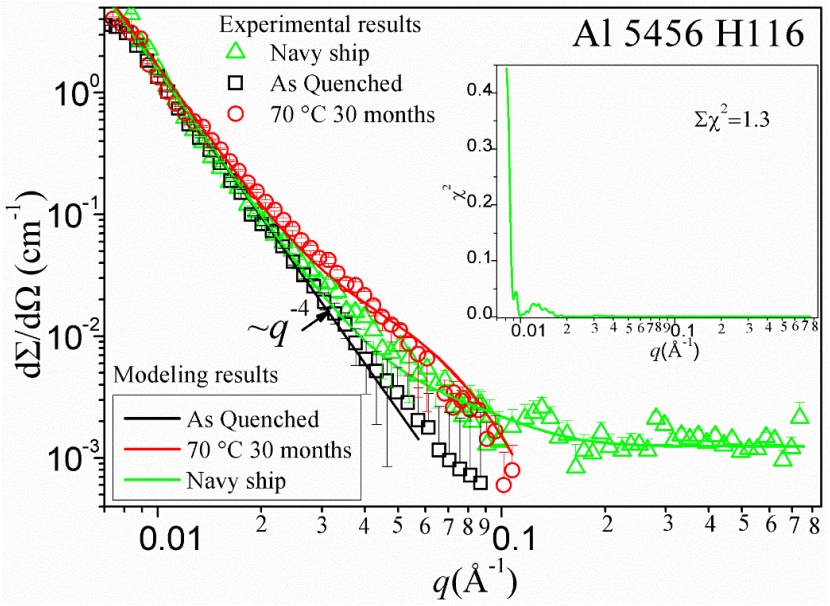

Figure 4.23 The SANS results for the as quenched, navy ship sample, and Al 5456 H116 aged at 70℃ for 30 months, the solid lines are the fitting results using Eq. (3.1), and the inserted image shows the χ^2-test result of the navy ship sample.

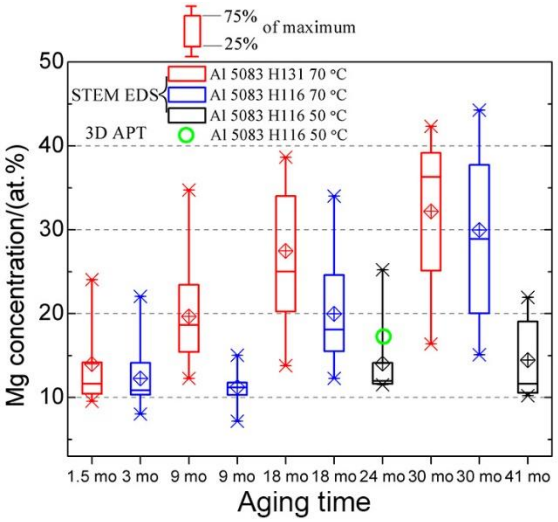

Figure 4.24 Statistical results of Mg concentration obtained from STEM EDS and APT for precipitates formed in Al 5083 H131 and H116 aged at different temperatures for different times.

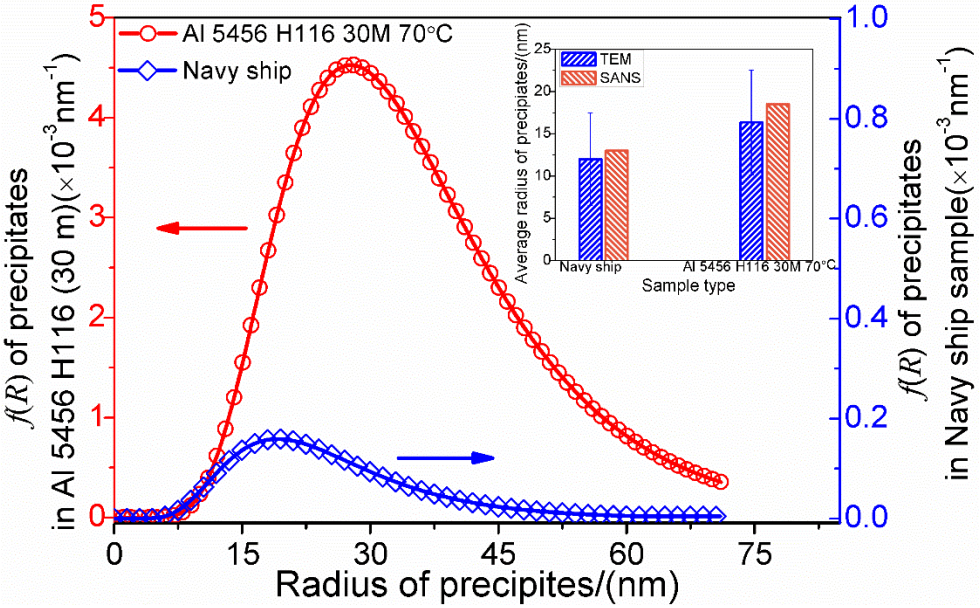

Figure 4.25 The volume fraction distribution results of the navy ship sample and the Al 5456 H116 aged at 70℃ for 30 months. The inserted image shows the average radii of intragranular precipitates obtained from STEM images and SANS fitting.

CHAPTER 5

MODELING OF Mg-RICH PRECIPITATES FORMED IN LOW TEMPERATURE SENSITIZED Al 5XXX ALLOYS

Based on STEM, APT, and SANS results above, Mg-rich precipitates are observed to form within Al matrix and at grain boundaries. In the present chapter, the nucleation, growth, and coarsening of intragranular and intergranular Mg-rich precipitates will be modeled using classical nucleation theory, mean field precipitate growth theory, and modified precipitate coarsening theory.

5.1 Modeling of intragranular precipitates formed in Al 5803 alloys

The precipitation process of Mg-rich precipitates in Al 5083 alloys is simplified as the precipitation of multiple phases (GP zone, β", β', and β phase) in a binary system (Al-Mg) scenario. By introducing the local equilibrium of chemical potential, Chen *et al*. modified the classical nucleation and growth theory to describe the precipitation behavior in a multicomponent system. [101] In the present study, this method was used to predict the evolution of Mg-rich phases in Al 5083 alloys. For simplification, several assumptions were made, as follows: (1) Mg concentrations in GP zones, β", β', and β phase are constant;

(2) the aspect ratio of GP zones, β", β', and β phase is the same for each alloy. By introducing the local equilibrium of chemical potential, Chen *et al*. modified the classical nucleation and growth theory to describe the precipitation behavior in a multicomponent system. [101]

5.1.1 Nucleation

For a spherical precipitate, the total Gibbs free energy change during nucleation is illustrated as

$$\Delta G = -V\Delta G_{v,i} + \gamma_i A \tag{5.1}$$

where $\Delta G_{v,i}$ is the driving force for nucleation of precipitate *i* (stands for GP zone, β", β', or β phase), *V* is the volume of the precipitate, *A* is the surface area of the precipitate, and γ_i is the interfacial energy of matrix and precipitate *i*.

By differentiating Eq.(5.1), the critical radius, R_i^* , needed for precipitate *i* to achieve stable growth is given as

$$R_i^* = \frac{2\gamma_i}{\Delta G_{v,i}} \tag{5.2}$$

The critical thermodynamic barrier for nucleation is then derived as

$$\Delta G_i^* = \frac{16}{3}\pi \frac{\gamma_i^3}{\Delta G_{v,i}^2} \tag{5.3}$$

The overall nucleation rate can be calculated by the Kampmann and Wagner's [88] equation,

$$\left.\frac{dN}{dt}\right|_i = N(1-f_V)Z_i\beta_i^* \exp\left(-\frac{\Delta G_i^*}{kT}\right)\exp\left(-\frac{\tau_i}{t}\right) \tag{5.4}$$

where N is the number of nucleation sites per unit volume, f_V is the volume fraction of all precipitates, and Z_i is the Zeldovich factor for precipitate i

$$Z_i = \frac{v_{at,i}}{2\pi R_i^{*2}}\sqrt{\frac{\gamma_i}{kT}} \tag{5.5}$$

where $v_{at,i}$ is the atomic volume and k is Boltzmann constant. β_i^* is the condensation rate of the solute atoms to a cluster of critical radius R_i^*

$$\beta_i^* = \frac{4\pi R_i^2 D\overline{X}_m}{a_0^4} \tag{5.6}$$

where $\overline{X}_m$ is the average Mg concentration in the matrix, D is the solute diffusion coefficient in the matrix, and a_0 is the lattice parameter. The incubation time for precipitate i is given as

$$\tau_i = \frac{4}{2\pi\beta_i^* Z_i^2} \tag{5.7}$$

5.1.2 Growth

At the interface of precipitate-matrix, a local equilibrium was assumed as follows:

$$\mu_{P_i} = \mu_{I_i} \tag{5.8}$$

where μ_{P_i} and μ_{I_i} stand for the chemical potential of Mg in the precipitate and matrix at the interface. Considering of the Gibbs-Thomson [146] effect, μ_{P_i} can be rewrote as

$$\mu_{P_i} = \mu_i + \frac{2\gamma_i v_{at,i}}{R_i} \tag{5.9}$$

where μ_i is the chemical potential for precipitate *i* of infinite radius, γ_i is the interfacial energy of matrix-precipitate *i*, and R_i is the radius of precipitate *i*. The flux of Mg, J_i, to certain precipitate *i* can be expressed using the growth rate, υ_i, as follows

$$J_i = \upsilon_i\left(X_{I_i} - X_{P_i}\right) \tag{5.10}$$

where X_{I_i} is the Mg concentration at the interface on the matrix side, and X_{P_i} is the Mg concentration in precipitate *i* at the interface. While the flux of Mg can also be calculated

using the diffusivity of Mg, *D*, in the matrix

$$J_i = -D\nabla X_i \tag{5.11}$$

where ∇X_i is the concentration gradient of Mg close to the interface on the matrix side. Combined Eq. (5.10) and (5.11) yields

$$\upsilon_i\left(X_{P_i} - X_{I_i}\right) = D\nabla X_i \tag{5.12}$$

∇X_i can be estimated using the following equation

$$\nabla X_i = \frac{\overline{X}_m - X_{I_i}}{d_i} \tag{5.13}$$

where d_i is the effective diffusion distance, which can be obtained as follows

$$d_i = \frac{\Omega_i}{2W_i} R_i = \varepsilon_i R_i \tag{5.14}$$

In the above equation, ε_i is a factor which equals (Ω_i/W_i), Ω_i is the dimensionless supersaturation, which is calculated as

$$\Omega_i = \frac{\overline{X}_m - X_{I_i}}{X_{P_i} - X_{I_i}} \tag{5.15}$$

W_i can be calculated from Ω_i using the following equation

$$2W_i^2 - 2W_i^3\sqrt{\pi}\exp\left(W_i^2\right)erfc\left(W_i\right) = \Omega_i \tag{5.16}$$

Insert Eq. (5.13) and (5.14) into Eq. (5.12), we can obtain

$$\upsilon_i\left(X_{P_i} - X_{I_i}\right) = D\frac{\overline{X}_m - X_{I_i}}{\varepsilon_i R_i} \tag{5.17}$$

Meanwhile, the diffusion coefficient of Mg, *D*, can be related to the chemical potential as follows

$$D = XM\frac{\partial \mu}{\partial X} \tag{5.18}$$

where *M* is the atomic mobility of Mg. Submitting Eq. (5.18) into Eq. (5.11), we can obtain

$$J_i = -D\nabla X_i = -X_{I_i} M\nabla \mu_i \tag{5.19}$$

Combine Eqs. (5.10), (5.14), and (5.19),

$$\upsilon_i\left(X_{P_i} - X_{I_i}\right) = X_{I_i} M \frac{\mu_m - \mu_{I_i}}{\varepsilon_i R_i} \tag{5.20}$$

In consideration of the ellipsoid shape of the precipitates, Eq. (5.20) can be modified to

$$\frac{4u}{F_{shape}} \upsilon_i\left(X_{P_i} - X_{I_i}\right) = X_{I_i} M \frac{\mu_m - \mu_{I_i}}{\varepsilon_i R_i} \tag{5.21}$$

where u is the aspect ratio, and F_{shape} is the shape factor

$$F_{shape} = 2 + \frac{u^2}{\sqrt{1-u^2}} \ln\left(\frac{1+\sqrt{1-u^2}}{1-\sqrt{1-u^2}}\right) \tag{5.22}$$

The final growth rate of precipitate i is given as

$$\upsilon_i = \frac{dR_i}{dt} = \frac{X_{I_i}}{X_{P_i} - X_{I_i}} \frac{F_{shape}}{2u} M \frac{\mu_m - \mu_{I_i}}{\varepsilon_i R_i} \tag{5.23}$$

The evolution of precipitate size distribution was described using the Euler-like approach developed by Myhr and Grong [96] and Perez *et al.* [85] The Euler-like approach is based on the discretization of the particle size distribution of precipitate i into size classes (indexed using j). For precipitate i, the number of new nuclei during the time step Δt is given by

$$\Delta N_i = \left.\frac{dN}{dt}\right|_i \Delta t \tag{5.24}$$

The new nuclei were put into the size class *j* of radius $R^*_{kT,i,j}$, which is calculated as

$$R^*_{kT,i,j} = R^*_{i,j}\left(1+\frac{1}{\sqrt{\pi}Z_{i,j}}\right) \tag{5.25}$$

The item $\left(1/\sqrt{\pi}Z_{i,j}\right)$ was added to ensure the stable growth of the new nuclei. Based on the mass balance of Mg in class *j*, the new population of class *j* at time (t+Δt) can be calculated using the control volume approach

$$\begin{aligned} N^{t+\Delta t}_{i,j} = {} & N^t_{i,j} + \frac{\Delta t}{\Delta R}\upsilon^t_{i,j-1}\left[\mathrm{Indx}\left(\upsilon^t_{i,j-1}\right)N^t_{i,j-1} + \mathrm{Indx}\left(-\upsilon^t_{i,j-1}\right)N^t_{i,j}\right] \\ & - \frac{\Delta t}{\Delta R}\upsilon^t_{i,j}\left[\mathrm{Indx}\left(\upsilon^t_{i,j}\right)N^t_{i,j} + \mathrm{Indx}\left(-\upsilon^t_{i,j}\right)N^t_{i,j+1}\right] \end{aligned} \tag{5.26}$$

where $N^t_{i,j}$ stands for number of precipitate *i* in class *j* at time *t*, ΔR is the width of a size class, and $\mathrm{Indx}(x)$ is a function defined as follows:

$$\mathrm{Indx}(x) = \begin{cases} 1, & \text{for } x > 0 \\ 0, & \text{for } x \le 0 \end{cases} \tag{5.27}$$

The overall number of precipitates *i* is obtained from the definition as

$$N_i = \sum_j N_{i,j} \tag{5.28}$$

and the average radius of precipitate *i* is given as

$$\overline{R_i} = \frac{\sum_j R_{i,j} N_{i,j}}{N_i} \tag{5.29}$$

The volume fraction of precipitate *i*

$$f_{V,i} = \sum_j N_{i,j} V_{i,j} \tag{5.30}$$

The average Mg concentration of the matrix is deduced from the solute mass balance principle:

$$\overline{X}_m = X_{0,m} - \sum_i f_{V,i} X_i \tag{5.31}$$

5.1.3 Parameters for the model

The chemical potential of the matrix and the precipitates (GP zones, β", β', and β phase), and the driving force for nucleation were calculated using the CALPHAD approach, which was based on the principle of minimizing the Gibbs free energy in the system. [147] The thermodynamic calculation of the Al-Mg system, including β", β', and β phase, has been performed in previous studies, [22,148–150] and the parameters used in the present

research are listed in Appendix A.2. Nozato and Ishihara [29] proposed that GP zones have a short-range ordered Al_3Mg structure, which was verified by Sato and Kamio [16] using high-resolution TEM. The fraction of the ordered Al_3Mg structure was assumed to be 50%, the average Mg concentration in GP zones was assumed to be 15 at.%, and the detailed calculation was shown in Appendix A.2.

The interfacial energy, γ_i, is a vital physical parameter for the nucleation and coarsening process of the predictive model. Sonderegger and Kozeschnik [151] developed an analytical approach to estimate the interfacial energy based on the broken-bond model, which has been proven to be effective in both steel [152] and Al alloy [99]. According to their model, the interfacial energy is calculated as

$$\gamma_i = \frac{n_s z_{s,eff}}{N_A z_{L,eff}} \Delta H_i \tag{5.32}$$

where n_s is the atom number density (per unit area) at the interface, which is equal to $\left(4^{2/3}/a_0^2\right)$ for fcc structure. $z_{s,eff}$ is the effective number of broken bonds, N_A is Avogadro's constant, and $z_{L,eff}$ is the effective coordination number. The mean value of $z_{s,eff}/z_{L,eff}$ for fcc is 0.3004 [151]. ΔH_i is the enthalpy of solution for precipitate *i*. The calculated values of γ_i are listed in Table 5.1.

The model was numerically solved using the standard simulation language MATLAB R2014a. The width of size class, ΔR, is set to be 0.5 nm. The standards for choosing the value of Δt, the cut-off values of size distributions, and the creation of new

size class can be find in Ref. [85]. The values of the other parameters in the model can be found in Table. 5.1.

5.1.4 Modeling results

Fig. 5.1 presents the modeling results of nucleation density, precipitate radius, volume fraction, and Mg concentration in the matrix versus aging time. The modeling results of number density versus aging time (Fig. 5.1) agree well with experimental results. In Al 5083 H131 aged at 70℃, GP zones nucleate first, followed by β", β', and β phase. From GP zone to β phase, the maximum number density decreases, which could be attributed to the depletion of nucleation sites and increasing energy barriers for nucleation. Metastable phases, GP zone, β" and β' phase, start to dissolve at 1, 4.5, and 8 months, respectively. The precipitate population of GP zones dominates at 1.5 months, and β" phase is the main precipitate at 9 months. While after 14 months (18 and 30 months), β' and β phases are predominant phases in the matrix. Al 5083 H116 aged at 70℃ shares the same precipitation sequence with Al 5083 H131, while the number densities of GP zones, β" and β' phase are less. In addition, β' and β phases become the main precipitates after 20 months. Even fewer precipitates are observed in Al 5083 H116 aged at 50℃, and the ultimate prevail phases are GP zones and β" phase after 41 months.

Fig. 5.1 also demonstrates the modeling and experimental results of precipitate radius at different aging time. During the nucleation stage, the precipitate radius changes slowly with time, and after that the precipitate starts to grow fast with aging time. The modeling results agree well with the experimental results for both Al 5083 H131 and H116 alloys. The radius of GP zone is minimum at the beginning of aging (for both Alloys), while it

reaches its maximum among the four types of precipitates at the end of the aging (30 months for 70℃, and 41 months for 50℃), which can be explained by the coarsening of GP zones (see Fig. 5.1 precipitate number density *N*). In addition, after aging at 70℃ for 30 months, the radius of GP zone in Al 5083 H131 is slightly larger than that in Al 5083 H116. While the radius of GP zone in Al 5083 H116 aged at 70℃ for 30 months is much larger than that of the same alloy aged at 50℃ for 41 months.

The volume fraction (Fig. 5.1, f_V) of precipitates is observed to increase continuously with aging time with a good agreement between simulation results and experimental results for both Al 5083 H131 (70℃) and H116 (50 and 70℃) alloys. On the contrary, the average Mg concentration in the matrix (Fig. 5.1, $\overline{X}_m$) decreases continuously with aging time.

The comparison of experimental and modeling results of precipitates' size distributions are displayed in Fig. 5.2. For Al 5083 H131 aged at 70℃ (Fig. 5.2 (a)), the increase of average radius and decrease of maximum precipitate numbers occur simultaneously from 1.5 to 30 months, which corresponds to a mixed growth/coarsening regime within an increasing influence of coarsening effects. The modeling results match well with SANS results. Moreover, the broadening of particle size distribution (PSD) of GP zone, β", β', and β phase was also observed. Perez *et al.* [85] found that the broadening of PSD will generate enough small particle size classes and ensure the beginning of coarsening stage. As a matter of fact, the PSD of GP zones at 30 months is firmly close to the standard LSW (Lifshitz-Slyosov-Wagner) [72,92] distribution (see Fig. 5.2 (a) 30 months), indicating the precipitation of GP zones occurs in the pure coarsening stage.

The PSD results of Al 5083 H116 aged at 70℃ for different times are shown in Fig. 5.2 (b), and the kinetics is quite similar to that of the Al 5083 H131 sample. However, there

is a slowing of coarsening compared with that of Al 5083 H131. For example, small size classes of GP zones formed during the nucleation stage have not been fully dissolved and resulted in a spike on the PSD plot of GP zones (see Fig. 5.2 (b) 18 months). An obvious shift between the PSD and the standard LSW distribution of GP zones can be observed (Fig. 5.2 (b) 30 months), indicating coarsening is not the only phenomenon. What's more, the population of β' phase rather than β phase is the largest in the 30 months' sample of Al 5083 H116 aged at 70℃. For 5083 H116 aged at a lower temperature (50℃), the precipitate number density and radius are much smaller (Fig. 5.2 (c)). Moreover, a large retardation of the growth and coarsening stages is also identified. From 3 to 24 months, even though the number of GP zone keeps decreasing, the shape of the GP zone PSD does not change too much. While in the 41 months' sample, the overall PSD of GP zones consists of a crest resulting from the growth of precipitates of relatively larger radius (larger than the critical radius), and a spike caused by the dissolving of smaller precipitates (smaller than the critical radius). Therefore, the large deviation between the theoretical LSW distribution and the PSD of GP zones (Fig. 5.2 (c) 30 months) can be attributed to the fact that GP zones are still in the growth and coarsening stage. The corresponding dominant phase in the 41 months' sample is β" phase.

5.1.5 Discussions

5.1.5.1 Effect of different tempers

For Al 5xxx alloys, H1 is a strain-hardened only temper, and the second digit of the temper represents the strain-hardened extent. [153] Therefore Al 5083 H131 (3/8 of full hardness) experiences more cold working than Al 5083 H116 (1/8 of full hardness), [153]

which was confirmed by the hardness of these two alloys. In addition, EBSD reveals that GND density (Fig. 4.2) of Al 5083 H131 is 1.6 times that in Al 5083 H116. STEM (Fig. 4.8, Table 4.1) and SANS (Fig. 4.9, Table 4.4) results show that fewer Mg-rich precipitates are formed in Al 5083 H116 than in H131, and the radii of these precipitates are smaller at the same aging states (for instance, 70℃ for 9, 18, and 30 months). Moreover, the modeling results (Fig. 5.1 and Fig. 5.2) show that there is a retardation of coarsening stage in Al 5083 H116 compared with H131 alloy.

The precipitation of Mg-rich precipitates (GP zone, β", β', and β phase) is a diffusion-controlled process, and Mg is the diffusion rate limiting element. Dislocations have been reported to be favorable nucleation sites for precipitation and potentially provide rapid diffusion paths for solute atoms. [84] On the one hand, the higher dislocation density in Al 5083 H131 provides more heterogeneous nucleation sites, leading to the higher precipitate number density in Al 5083 H131. On the other hand, the pipe diffusion effect [154] of dislocation can highly facilitate the growth of β' phase, which has been observed in previous studies [15,23]. Hart [155] proposed a simple way to estimate the effective diffusion coefficient, D_{eff}, caused by dislocations, as follows

$$D_{eff} = (1 - f_d) D_{bulk} + f_d D_d \tag{5.33}$$

where f_{d} is the fraction of dislocation, D_{bulk} and D_{d} are the diffusion coefficients of Mg in the Al matrix and dislocation cores. f_{d} can be calculated from dislocation density and the area of dislocation core. Taking the dislocation along the {111} plane as an example, the radius of the dislocation core ranges from 0.35 to 1.4 nm. [143] Atomic simulation reveals

that the activation energy of a Mg atom in the dislocation core is about 75% [156] that in the bulk (Q=-112.499kJ, see Table 5.1). The GND density (5.33×10^{13} m^{-2} for H131, and 3.28×10^{13} m^{-2} for H116) is used to roughly estimate the relative dislocation density ratio. Based on Eq. (5.33), D_{eff} of H131 to that of H116 is about 1.5 at 70℃. Henceforth, a relatively slower precipitate growth rate (Eq. (5.23)) as well as a smaller precipitate radius will be expected in Al 5083 H116.

Moreover, the growth driving force ($\mu_m - \mu_{I_i}$) related to the Gibbs-Thomson effect is also of great importance. Fewer and smaller precipitates in Al 5083 H116 lead to a higher average matrix concentration (see $\overline{X}_m$ results in Fig. 5.1 (a) and (b)), indicating a larger μ_m. Combining Eq. (5.9) and (5.23), one finds a smaller R_i value is needed to make v_i negative. Consequently, only precipitates smaller than R_i can dissolve, which leads to the spike in the PSD plot of GP zones at 18 months.

5.1.5.2 Effects of different aging temperatures

For Al 5083 H116, different aging temperatures lead to a large difference in the precipitation behavior (see Table 4.1, Table 4.4, Fig. 5.1 and 5.2). A higher aging temperature means more atoms are able to overcome the energy barrier for nucleation, thus more precipitates are found in the 70℃ aged Al 5083 H116 sample. Moreover, the diffusion coefficient of Mg atoms at 70℃ is 10 times that at 50℃ (Q=-112.499kJ). Therefore, the smaller precipitate size and the retardation of the growth and coarsening stage can be explained in the same way above (different temper effects), whereas a higher temperature may cause recrystallization of cold-worked alloy and the reduction of dislocations. Oguocha *et al.* [157] aged Al 5083 H116 alloys at different temperatures, and

found that obvious recrystallization happened at temperatures higher than 175℃. Henceforth, 70℃ is not high enough to cause recrystallization and a large decrease in dislocation density.

5.1.5.3 Different nucleation sites

STEM and EDS results reveal that Mg-rich precipitates first form on heterogeneous sites such as the surface of pre-existing particles, dislocations, and grain boundaries. The relatively low active energy for nucleation of these sites is used to explain the preference. [158] APT results show that the shape of precipitates on the surface of pre-existing particle is different from that in the matrix. Considering β" phase is coherent with Al matrix, [16] one possible reason for this difference is that the diffusion coefficient of Mg at the β" phase-matrix interface is close to that of Mg in the matrix, when an elongated precipitate shape will be expected. [137]

5.1.5.4 Phase transformation sequence

The precipitate sequence of Mg-rich precipitates is affected by aging temperature, Mg concentration in the matrix, and aging time. β' and β phase are reported to form at high temperatures (>150℃), [34] while given enough aging time (12 months) β' and β phase were also observed to form at 70℃ in Al 5083 alloy [23]. Moreover, TEM and differential scanning calorimetry (DSC) [16,32] results indicated that GP zones will form before the appearance of β" phase in a matrix of relatively low Mg concentration (<14 wt.%), and both GP zones and β" phase [16] can formed below 80℃. In the present study, the Mg concentration is 5.25 at.%, the aging temperature is 50 and 70℃, and the aging time is as

long as 41 and 30 months, respectively. Therefore, GP zones, β", β', and β phase are able to form in Al 5083 alloy. In reality, the presence of GP zones and β" phase in Al 5083 H116 sample aged at 50℃ have been confirmed by APT results.

In order to fit the SANS results, the value of $\Delta\eta$ was assumed to be variable based on the concentration change of Mg-rich precipitates. Furthermore, in the modeling part, a multiphase (GP zone, β", β', and β phase) precipitation process was assumed. Fig. 5.3 is the difference of scattering length density obtained from SANS fitting and calculation based on the volume fraction of each phase, using the following equation:

$$|\Delta\eta|^2 = \sum_i f_{V_i}^2 |\eta_i - \eta_m|^2 \tag{5.34}$$

Both experimental and model results of $\Delta\eta$ show a decreasing trend for Al 5083 alloys aged at 70℃. For Al 5083 H116 alloy aged at 50℃, the value of $\Delta\eta$ does not change too much from 9 to 41 months. In Fig. 5.3, the modeling results are always larger than the experimental results, and one possible explanation is that the volume of Mg-rich precipitates is underestimated when fitting to the overall SANS results. In spite of this difference, the assumption of phase transformation from supersaturated solid solution-GP zone- β"- β'- β phase in Al 5083 alloy aged at 50 and 70℃ is reasonable.

5.1.5.5 The multiphase binary Al-Mg system model

In order to deal with the phase transformation (from GP zone to β phase) process in Al 5083 alloys aged at 70 and 50℃, the local equilibrium of Mg chemical potential at the interface of precipitate *i*-matrix is assumed. This assumption was introduced by Chen *et*

al. [101] to handle the continuous tie-lines shifting problem caused by the cross-diffusion in multicomponent systems. In the present study, Al 5083 alloys were simplified as an Al-Mg binary system, and no cross-diffusion phenomenon needs to be considered, while the local equilibrium assumption is still a good method to account for different Mg concentrations at different interfaces of precipitate *i*-matrix. Svoboda [96,158] developed a model to describe spherical precipitates formed in multicomponent multiphase systems, and in this model growth of precipitates, change of precipitate concentration, different type of solute atoms, and different nucleation sites are considered. In addition, an Euler-like multiclass method was adopted to predict the number evolution of precipitates. In fact, if the precipitate concentration is assumed to be constant in Svoboda's model, the precipitate growth mechanism will become the same as the model in the present study.

The model in this study predicts the dissolution of metastable phases, the growth of precipitates, the increase of overall precipitate volume, and the depletion of Mg in the matrix as well as Svoboda and Chen's model did. However, the radius of GP zone in Al 5083 H131 does not decrease even after 30 months, which is different from the results in Ref. [100] and [102]. In these two studies, the aging temperature is very high (>500℃), the precipitation and diffusion process was so fast that the matrix became deplete of solute atoms very quickly. Under this condition, the solute concentration in the matrix is even lower than solute concentration at the largest precipitate-matrix interface. Thus, all precipitates will start to dissolve and the radius of precipitate will decrease too. Fig. 5.4 displays the PSD of GP zones and β" phase versus their growth rates (υ_i) for different radius class of Al 5083 H131 aged at 70℃ for 30 months. The turning point is the place where

growth rate turns from negative to positive (radius from small to large). Therefore, there is still a large number of GP zones and β" phase can grow.

5.2 Modeling of intergranular precipitates formed in Al 5803 alloys

Both Fisher [52] and Shewmon [53] had investigated and obtained a solution to the problem of diffusion within the grain matrix and along the grain boundary. By referring to their solution method, our analysis is based on assumptions, as follow: (1) the flux of solute within the grain is everywhere normal to the grain boundary, (2) the concentration of Mg at the clean grain boundary and matrix-precipitates interface is the same and written as $C_{\alpha\beta}$, (3) the Mg-rich precipitates formed at grain boundaries are treated as β phase (Al_3Mg_2), and their concentration is C_β.

5.2.1 Shape of intergranular precipitates

The most common precipitate morphology formed at the grain boundary of Al 5xxx alloy is that of the allotriomorphs. In previous research, [56,137] the shape of intergranular precipitate was assumed to be

$$\frac{r^2}{R^2}\sin^2\chi+\left[\left(\frac{z}{mR}\right)\tan^2\chi+1\right]^2\cos^2\chi=1 \qquad (5.35)$$

where $m=\tan\psi$, and ψ is the contact angle of the precipitate, which is equal to $\theta(R)$. R is the half-length of precipitate, as shown in Fig. 5.5. Depending on different values of χ, Eq. (5.35) is able to represent an ellipse as well as a sphere, and the detailed relationship between χ and the precipitate shape can be found in Ref. [137].

Based on Eq. (5.35), the half-volume of the precipitate, *M*, is given as (Eq. (33) in Ref. [137])

$$M = \int_0^R 2\pi r z(r,t) dr = \frac{\pi m}{3}\left[1 - \frac{1}{(1+\cos\chi)^2}\right] R^3 = f_{PV} R^3 \tag{5.36}$$

And half the surface area of the precipitate, S_A, can be obtained as [159]

$$S_A = \frac{\pi}{b'^2 e}\left\{\begin{array}{l} b'^2\left[ea'^2 + b'^2 \ln(eab + ab)\right] - a'd'e\sqrt{(a'd'e)^2 + b'^4} \\ -b'^4 \ln\left(z_d ea + \sqrt{(z_d ea)^2 + b^4}\right) \end{array}\right\} R^2 = f_{PA} R^2 \tag{5.37}$$

where

$$a = \frac{R}{\sin\chi} = a'R \tag{5.38}$$

$$b = \frac{mR}{\tan^2\chi\cos\chi} = b'R \tag{1.39}$$

$$z_d = \frac{mR}{\tan^2\chi} = d'R \tag{5.40}$$

$$e = \sqrt{1-\left(\frac{b}{a}\right)^2} = \sqrt{1-\left(\frac{m}{\tan\chi}\right)^2} \tag{5.41}$$

where e is the eccentricity of the ellipse, and a, b, and z_d can be found in Fig. 5.5.

5.2.2 Flow to the grain boundary

By considering only the half-space $0 < z < h/2$ (h is grain size), the concentration of Mg in the grain matrix satisfied Fick's second law,

$$\frac{\partial C(z,t)}{\partial t} = D_m \frac{\partial^2 C(z,t)}{\partial z^2} \tag{5.42}$$

where D_m is the volume-diffusion coefficient in the grain matrix.

Fig. 5.6 is a typical TEM image of Al 5083, and the image shows the grain size is about 1μm. In the early stage of aging, the diffusion distance of Mg within the grain matrix (for example, after aging at 70 ºC for one month), is only 4 nm, which is far less than the grain size. Therefore, the diffusion system can be treated as a semi-infinite bulk case, and the appropriate boundary conditions for the concentration $C(z,t)$ are

$$C(z,0) = C_\alpha, \quad h/2 \geq z \geq 0, \tag{5.43}$$

$$C(0,t) = C_{\alpha\beta}, \; t > 0 \tag{5.44}$$

where C_α is Mg concentration inside the grain before aging, and $C_{\alpha\beta}$ is Mg concentration at the grain boundary. According to the boundary conditions listed above, the Mg concentration profile inside the grain is, therefore,

$$C(z,t) = C_{\alpha\beta} + (C_\alpha - C_{\alpha\beta})\,erf\left(\frac{z}{2\sqrt{D_m t}}\right) \tag{5.45}$$

The value of solute flux to the grain boundary can be written as

$$J_{ms} = D_m \left.\frac{\partial C(z,t)}{\partial z}\right|_{z=0} = \frac{(C_\alpha - C_{\alpha\beta})D_m^{\frac{1}{2}}}{\sqrt{\pi t}} \tag{5.46}$$

In this study, Al 5083 was aged at 70 ºC for as long as 30 months. Fig. 5.7 presents an EDS line scan and the corresponding concentration profile of Mg within the grain matrix of Al 5083 aged at 70 ºC for 30 months. An obvious Mg deplete zone, about 150 nm in width, can be found on each side of the grain boundary in Fig.5.7 (b). Moreover, from the symmetry of the Mg concentration profile, the grain size is estimated to be 0.6 μm, indicating the diffusion distance is almost 50 percent of the grain size. Thus, at the end of aging, the diffusion system is finite, and the appropriate boundary conditions for intermediate and long-term exposures are shown as follows:

$$C(z,0) = n_\alpha,\ h/2 \geq z \geq 0 \tag{5.47}$$

$$C(0,t) = C_{\alpha\beta},\ t > 0 \tag{5.48}$$

$$\frac{\partial C(h/2,t)}{\partial z} = 0 \tag{5.49}$$

Therefore, the Mg concentration profile inside the grain for long-term aging of Al 5083 alloy at low temperatures is obtained as

$$C(z,t) = C_{\alpha\beta} + 4\frac{C_\alpha - C_{\alpha\beta}}{\pi}\sum_{j=0}^{\infty}\frac{1}{(2j+1)}\sin\left(\frac{(2j+1)\pi z}{h}\right) \exp\left[-\left(\frac{(2j+1)\pi}{h}\right)^2 D_m t\right],\ (j = 0,1,2,\ldots) \tag{5.50}$$

and the corresponding value of Mg flux to the grain boundary is

$$J_{ml} = D_m \left.\frac{\partial C(z,t)}{\partial z}\right|_{z=0} = \frac{4(C_\alpha - C_{\alpha\beta})D_m}{h} \sum_{j=0}^{\infty}\exp\left[-\left(\frac{(2j+1)\pi}{h}\right)^2 D_m t\right],\ (j = 0,1,2,\ldots) \tag{5.51}$$

However, this equation does not work well for short diffusion distances. Therefore, for long-term aging of Al 5083 alloy, the concentration profile of Mg inside the grain needs to be described using two different expressions.

5.2.3 Mg concentration along the grain boundary

Brailsford and Aaron [56] investigated the time-dependent grain boundary concentration by considering the solute flux diffused to the grain boundary. To solve the unsteady state diffusion equation along the grain boundary, a further approximation, $\partial C_b/\partial t = 0$, was made to make up the limited number of boundary conditions. In this research, a collector plate-based equivalent Mg concentration at grain boundary, C_{Rx}, will be established according to the solute mass balance.

$$J\left(\pi R_c^2 - \pi r_i^2\right) = 2\pi r_i\left(\delta_{eff}/2\right)D_b\left.\frac{dC}{dr}\right|_{r=r_i} \tag{5.52}$$

where J is the solute flux to the grain boundary, R_c is the radius of the collector plate, δ_{eff} is the effective thickness of grain boundary, D_b is the solute diffusivity within the grain boundary, and r_i is the distance to the center of the precipitate within the collector plate surface (see Fig. 5.5), where the concentration gradient of solute atoms is $\left.\frac{dC}{dr}\right|_{r=r_i}$.

Integrating the above equation along the grain boundary from R to R_x (see Fig. 5.5) gives

$$\frac{J}{\delta_{eff} D_b}\int_R^{R_x}\left(R_c^2\frac{1}{r_i} - r_i\right)dr = C_{R_x} - C_R \tag{5.53}$$

or

$$C_{R_x} = C_R + \frac{J}{\delta_{eff} D_b}\left[\frac{R^2}{2} - R_c^2\ln R + R_c^2\ln R_x - \frac{R_x^2}{2}\right] \tag{5.54}$$

where C_R is the Mg concentration immediately adjacent to the surface of intergranular precipitate. The value of C_R is determined by the Gibbs-Thomson [89,90,146] equation as

$$C_R = C_{eq} \exp\left(\frac{\gamma v_{at}^P}{kT} K_R \right) \tag{5.55}$$

C_{eq} is the Mg concentration in the grain boundary away from the influence of Mg-rich precipitates, which is equal to $C_{\alpha\beta}$ in this study. γ is the interfacial energy matrix-precipitate, and v_{at}^P is the atomic volume. K_R is equivalent curvature of the precipitate, [84] and it is given as

$$K_R = \frac{2 f_{PA}}{3 f_{PV} R} \tag{5.56}$$

Therefore, the average Mg concentration at precipitate-free grain boundary area can be calculated as:

$$\overline{C}_{R_x} = \frac{1}{R_c - R} \int_R^{R_c} C_{R_x} \, dr \tag{5.57}$$

After some algebra, $\overline{C}_{R_x}$ is obtained as

$$\overline{C}_{R_x} = \left[C_R + \frac{J}{\delta_{eff} D_b} \left(\frac{R^2}{2} - R_c^2 \ln R \right) \right] + \frac{J}{\delta_{eff} D_b (R_c - R)} \left[R_c^3 \left(\ln R_c - \frac{7}{6} \right) - R \left(R_c^2 \ln R - R_c^2 - \frac{R^2}{6} \right) \right] \tag{5.58}$$

5.2.4 Nucleation of intergranular precipitates

In classical nucleation theory, precipitates will nucleate within the supersaturated matrix, and based on the ideal solution model, the driving force for nucleation can be written as

$$\Delta g = -\frac{kT}{v_{at}^P} \ln \left(\frac{\overline{C}_{R_x}}{C_{eq}} \right) \tag{5.59}$$

where C_{eq} is the equilibrium solute concentration of the grain boundary. From the driving force, [160] a critical nucleation radius was derived as

$$R^* = -\frac{2 f_{PA} \gamma}{3 f_{PV} \Delta g} \tag{5.60}$$

The corresponding activation energy for nucleation is

$$\Delta G^* = \frac{4 f_{PA}^3}{27 f_{PV}^2} \frac{\gamma^3}{\Delta g^2} \tag{5.61}$$

By introducing incubation time τ_0 for nucleation, Kampmann and Wagner [88] modified the standard Becker-Döring [87] nucleation theory, leading to the follow expression for the nucleation rate per unit area

$$\left.\frac{dN}{dt}\right|_n = \delta_{eff} N_{0het} Z\beta^* \exp\left(-\frac{\Delta G^*}{kT}\right)\exp\left(-\frac{\tau_0}{t}\right) \tag{5.62}$$

where $N_{0\text{het}}$ is the number of nucleation sites per unit volume at the grain boundary, and Z is the Zeldovich factor [63]

$$Z = \frac{v_{at}^P}{2\pi R^{*2}}\sqrt{\frac{\gamma}{kT}} \tag{5.63}$$

β^* is the condensation rate of the solute atoms to a cluster of critical radius R^*. Russell [64] proposed an expression involving the diffusion coefficient D_b, the lattice parameter a_0, and the average solute concentration at grain boundaries. β^* is expressed as:

$$\beta^* = \frac{4\pi R^{*2} D_b \overline{C}_{R_x}}{a_0^4} \tag{5.64}$$

The incubation time is given as

$$\tau_0 = \frac{4}{2\pi\beta^* Z^2} \tag{5.65}$$

For the complex structure of grain boundary, N_{0het} is difficult to obtain directly. However, it can be estimated from the nucleation site per unit volume within the grain matrix, N_{0hom}, [84] which is

$$\frac{N_{0het}}{N_{0\hom}} = \frac{\delta_{eff}}{h}\exp\left(\frac{\Delta G^*_{\hom} - \Delta G^*}{kT}\right) \tag{5.66}$$

where, δ_{eff} is the effective thickness of grain boundary, and $\Delta G^*_{\hom}$ is the activation energy for homogeneous nucleation.

For precipitation within the grain matrix, the volume fraction of the precipitates calculated from the classical nucleation theory is less than 1 percent at the very beginning of the coarsening process. [85] However, TEM results showed that grain boundaries of Al 5xxx alloys will be fully covered by Mg-rich precipitates if aging temperature is high enough and aging time is long enough. [137] For heterogeneous nucleation at grain boundaries, precipitates nucleate within a narrow area with a width δ_{eff}. Therefore, all potential nucleation sites will be utilized gradually. Considering this effect, the available nucleation sites per unit volume will be modified accordingly with time.

Fig. 5.8 shows the average size of precipitates in comparison with the effective grain boundary thickness at different times. At t_2, this thickness of the β phase is equal to δ_{eff}. When aging time, t, is shorter than t_2, the bulk of the precipitate is located within the grain boundary area, therefore the available volume for the nucleation of new precipitates is given as

$$V_{avl} = (1m^2) \times \delta_{eff} - 2NV \tag{5.67}$$

where N is the number of precipitates within the grain boundary per unit area, and V is half the volume of precipitates. The volume of grain boundary per unit area is given as ($1m^2 \times \delta_{eff}$), which will be simplified as δ_{eff} hereafter.

For a long aging time ($t > t_2$), the thickness of Mg-rich precipitates is larger than δ_{eff}. In this case, the available volume for the formation of new arriving precipitates is

$$V_{avl} = \delta_{eff} - 2NV' \tag{5.68}$$

with

$$V' = f_{PV} R\left(R^2 - R_{\delta/2}^2\right) = f_{PV}\left[1 - \frac{1}{\sin^2 \chi} + \left(\frac{1}{\tan \chi} + \frac{\delta_{eff}}{2}\frac{\tan \chi}{mR}\right)^2\right] R^3 \tag{5.69}$$

where V' is half the volume of the precipitate within the grain boundary, and $R_{\delta/2}$ is equal to [$r(z = \delta_{eff}/2)$](see Fig. 5.8). From Eqs. (5.67) and (5.68), the fraction of the available boundary volume is written as

$$f_{avl} = V_{avl} / \delta_{eff} \tag{5.70}$$

Then, the nucleation rate can be modified as

$$\left.\frac{dN}{dt}\right|_n = \delta_{eff} f_{avl} N_{0het} Z\beta^* \exp\left(-\frac{\Delta G^*}{kT}\right)\exp\left(-\frac{\tau_0}{t}\right) \tag{5.71}$$

The collector plate mechanism was first put forward by Aaron and Aaronson, [50] and modified by Carolan and Faulkner, [58] which proved to be an effective method in heterogeneous precipitation. For a variable collector plate, the area, $\overline{A}$, is equal to

$$\overline{A} = 4\pi D_b t \tag{5.72}$$

while the collector plate mechanism also assumed that one precipitate corresponds to one collector plate. Henceforth, when grain boundary nucleation density is relatively high, the collector plate area is given by

$$\overline{A} = 1/N \tag{5.73}$$

where N is the number of nuclei per unit area at grain boundary. The final collector plate area should equal the smaller value of the above two expressions, which can be written as

$$\overline{A} = \mathrm{Min}\left[4\pi D_b t,\ 1/N\right] \tag{5.74}$$

5.2.5 Growth and coarsening theory of intergranular precipitates

In the first stage of precipitation, nucleation and growth are considered simultaneously. The increasing nucleation density is caused by the formation of new

precipitates, and the variation of the mean precipitate radius includes two parts: the growth of the existing precipitates and the arrival of new precipitates. Based on the mass conservation of Mg, we can obtain

$$Jdt = (C_\beta - C_{\alpha\beta})NdV + (C_\beta - C_{\alpha\beta})V^* dN \tag{5.75}$$

leading to the growth rate equation

$$\left.\frac{dV}{dt}\right|_g = \frac{J}{N(C_\beta - C_{\alpha\beta})} - \frac{1}{N}\frac{dN}{dt}\left(\eta f_{PV} R^{*3}\right) \tag{5.76}$$

where C_β is the Mg concentration of the precipitate, and V^* is the volume of the new-forming precipitates. Wagner and Kampmann [88] pointed out that the new-arriving precipitates can grow only if their radius is slightly larger than the critical nucleation radius. Thus, a numerical factor η was used to account for this effect. The value of η is taken as 1.05. [94]

In the late stage of precipitation, nucleation rate will decrease progressively because of the desaturation of solute atoms as well as the depletion of the nucleation sites. Precipitate growth and coarsening will take place within the grain boundary. Three intergranular coarsening mechanisms will be discussed.

5.2.5.1 Kirchner's coarsening mechanism [67] for grain boundary precipitates

Based on Speight's results [69] of the growth rate of intergranular precipitate, Kirchner [67] derived a distribution function for precipitates at the grain boundary by

considering Wagner's continuity theory. [68] The volume change rate versus time with respect to the steady state distribution function (the coarsening stage) was obtained as follows:

$$\left.\frac{dV}{dt}\right|_{Kc} = \frac{27 f_{PV} C_{\alpha\beta} \delta_{eff} \gamma v_{at}^{P}}{128(C_{\beta} - C_{\alpha\beta}) A' \ln(R_c / R) kT} \frac{D_b}{R} \tag{5.77}$$

in which $A' = 3 f_{PV}^{2} / \pi f_{PA}$. The detailed derivation of Eq. (5.77) can be found in Appendix A.3.

5.2.5.2 (Lifchitz-Slyosov-Wagner) LSW Coarsening mechanism [68,72]

By adopting the growth mechanism developed by Zener, [49] coupled with solving the continuity and solute mass balance equations, Lifchitz and Slyosov [72] and Wagner [68] simultaneously derived the mean radius evolution equations for the coarsening stage (referred as the LSW law). The LSW equation is widely used to describe the coarsening process of precipitate within the grain matrix. By assuming Mg diffusion only takes place within the grain boundary area, and the solute flux between the grain matrix and the grain boundary can be ignored, the classical LSW theory can be modified for the case of intergranular precipitate coarsening, as shown in Appendix A.4.

$$\overline{R}^{3} = \frac{4}{9} \frac{f_{PA}}{f_{PV}} \alpha D_b t \tag{5.78}$$

Considering the solute concentration difference, the pure coarsening rate is written as

$$\left.\frac{dV}{dt}\right|_{Lc} = \frac{4}{9}\frac{\alpha f_{PA} D_b}{(C_\beta - C_{\alpha\beta})} \tag{5.79}$$

5.2.5.3 The new coarsening model

Ardell [70] found the particle size distribution function of intergranular precipitates can be totally different for different volume fractions (equals to $N\pi R^2$ in this study) of precipitates at grain boundaries. In the limiting case, ($N\pi R^2$)=0, the steady-state particle size distribution function is of the same form as that derived by Kirchner. [67] However, when ($N\pi R^2$)=1, the famous LSW particle size distribution function can be used. In fact, these two distribution functions indicate two different coarsening mechanisms. In this study, we assume that in the entire coarsening process, the control mechanism will transfer continuously from the Kirchner mechanism to the LSW mechanism, which can be written as

$$\left.\frac{dV}{dt}\right|_{c} = (1 - f_L)\left.\frac{dV}{dt}\right|_{Kc} + f_L \left.\frac{dV}{dt}\right|_{Lc} \tag{5.80}$$

where f_L stands for the fraction of the LSW mechanism, which can be extracted from the relationship between (R_{max}/R) (R_{max} is the maximum allowable particle size in the distribution of particle size) and the volume fraction of grain boundary precipitates ($N\pi R^2$), as shown in Fig. 5.9. According to Ardell's research, [70] there is no explicit expression

between (R_{max}/R) and ($N\pi R^2$), thus an equation is fitted and shown in Fig. 5.9. After adaptation to the range of f_L (from 0 to 1), the final expression of f_L is

$$f_L = 1 + 0.111 \ln\left(R^2 / R_c^2 + 0.00012\right) \tag{5.81}$$

In order to transfer continuously from the growth stage to the coarsening stage, Deschamps and Bréchet [94] and Perez *et al*. [85] introduced a coarsening fraction, f_c, based on the mean radius and critical radius of the precipitates to weight the pure growth and pure coarsening behavior. Perrard *et al*. [161] calculated the coarsening fraction from the ratio between the current volume fraction and the Gibbs-Thomson effect corrected equilibrium volume fraction of precipitates. In this study, the coarsening fraction is defined as the ratio of solute flux caused by the coarsening mechanism to the total solute flux to the precipitate, which is given as follows:

$$f_c = \left.\frac{dV}{dt}\right|_c \Big/ \left(\left.\frac{dV}{dt}\right|_g + \left.\frac{dV}{dt}\right|_c \right) \tag{5.82}$$

Combining Eqs.(5.77), (5.79), and (5.82), the overall volume change rate of precipitate in the growth and coarsening stages can be obtained as:

$$\left.\frac{dV}{dt}\right|_f = f_c \left.\frac{dV}{dt}\right|_c + (1 - f_c) \left.\frac{dV}{dt}\right|_g \tag{5.83}$$

In the pure coarsening stage, the solute mass balance in a unit area of grain boundary can be given by (assuming the value of f_{PV} does not change within the time interval Δt)

$$N(t) f_{PV} R^3(t)(C_\beta - C_{\alpha\beta}) + J\Delta t = N(t+\Delta t) f_{PV} R^3(t+\Delta t)(C_\beta - C_{\alpha\beta}) \qquad (5.84)$$

Differentiation of Eq. (5.84) and use of the pure coarsening theory (Eqs. (5.77) and (5.79)) yields the precipitate number density evolution during the pure coarsening stage:

$$\left.\frac{dN}{dt}\right|_c = \frac{J}{f_{PV} R^3 \left(C_\beta - C_{\alpha\beta}\right)} - \frac{N}{f_{PV} R^3} \left.\frac{dV}{dt}\right|_c \qquad (5.85)$$

The volume growth rate of precipitates can be also derived from Eq. (5.36), and with the aid of Eq. (5.83), we can obtain

$$\frac{dM}{dt} = \frac{d(f_{PV} R^3)}{dt} = \left.\frac{dV}{dt}\right|_f \qquad (5.86)$$

After some algebra, we can have the precipitate growth rate in the length direction as

$$\frac{dR}{dt} = \frac{1}{3 f_{PV} R^2} \left.\frac{dV}{dt}\right|_f - \frac{R}{3 f_{PV}} \frac{df_{PV}}{dt} \qquad (5.87)$$

As stated by Deschamps and Brechet, [94] the transition from nucleation and growth stage to growth and coarsening stage is determined by the relative value of the rate of

decrease in the precipitate number density caused by coarsening and nucleation. According to this criterion, the number of precipitates is given as

$$\left\{\begin{array}{ll} \dfrac{dN}{dt}=\left.\dfrac{dN}{dt}\right|_c & \text{if} \quad -\left.\dfrac{dN}{dt}\right|_c > \left.\dfrac{dN}{dt}\right|_n \\ \dfrac{dN}{dt}=\left.\dfrac{dN}{dt}\right|_n & \text{if} \quad -\left.\dfrac{dN}{dt}\right|_c < \left.\dfrac{dN}{dt}\right|_n \end{array}\right\} \tag{5.88}$$

Combining Eqs. (5.76), (5.82), (5.85), and (5.88), it is apparent that the value of f_c must be larger than 0.5 before coarsening can really start ($dN/dt<0$). In other words, when f_c is smaller than 0.5, precipitate growth will dominate regardless of the nonzero value of f_c. For intergranular precipitation, there is a long period between the precipitation stage and the coarsening stage, therefore the precipitate number evolution rate is equal to the number change rate during the coarsening stage, as shown in Eq. (5.88).

5.2.6 Numerical solution

Similarly, a first-order explicit finite difference approximation method is used to perform the integration as well as the differentiation process in this study. In Eq. (5.87), the value of df_{PV}/dt can be calculated as follows:

$$\frac{df_{PV}}{dt}=\frac{f_{PV}(t+\Delta t)-f_{PV}(t)}{\Delta t} \tag{5.89}$$

Given a start value of N, R, and t, half the length of the precipitate, R, and the nucleation number density, N, can be integrated by using an inverted form of Eq. (5.89)

with an adaptive time step. Using Eq. (35) in Ref. [137], half the thickness, *S*, of the precipitate is

$$S = \frac{m\cos\chi}{1+\cos\chi} R \tag{5.90}$$

During the numerical solving process, the area of the collector plate changes as a result of the nucleation and the coarsening mechanism. In order to avoid an overlap effect, we adopt the smaller value of Eqs. (5.72) and (5.73). In terms of the transition from short-term concentration profile to a long-term concentration profile of Mg within the matrix, the same criterion in Ref. [137] ($2\sqrt{D_m t} \approx 20\%$ of the grain size) will be used. In addition, the results of *R* and *t* of the former stage will used as the initial values for the next stage. The time interval in the numerical solving process is chosen to be 1 second, yielding a reasonable result compared with experimental results without consuming too much computational time.

Parameters used for the numerical solving of the model are listed in Table 5.2. Part of the parameters, such as diffusion coefficient of Mg at different places (D_m, D_b, D_s), contact angle (ψ), grain size (h), Mg concentration (C_α, C_β, $C_{\alpha\beta}$) etc. can be found in Fig. 5.10, Fig. 5.11, and Ref. [137]. The precipitates-matrix interfacial energy, γ, will be slightly adapted to fit the experimental data. According to previous research, [162,163] the retained value of 0.07 $J \cdot m^{-2}$ is in a reasonable range, varying from 0.04 to 0.4 $J \cdot m^{-2}$. The effective thickness of the grain boundary is assumed to be 0.5 nm. [164,165]

5.2.7 Results and discussions

Inserting the above parameters into the model, the thickness and continuity results can be calculated using the numerical method. As shown in Fig. 5.12, the modeling results match generally well with the experimental results obtained from TEM images of Ref. [137]. Moreover, before 12 months, the modeling results of thickness and continuity are larger than the value obtained from the model in Ref. [137], and after 12 months these two values become smaller. One possible explanation for this phenomenon is that the number of nucleation is fixed ($3.2\times10^{13}/m^2$) for the whole nucleation stage in the previous research. [137] However, the nucleation density in the present study increases gradually from 0 to $4.5\times10^{13}/m^2$. In other words, at the beginning of nucleation, there are more collector plates at the grain boundary in the previous model, [137] therefore solute flux arriving at each collector plate will decrease when the total Mg atom flux does not change (the total solute flux will not change if the aging temperature is the same). Consequently, the growth rate of precipitates will decrease, and finally smaller precipitates will form. However, because of a higher ultimate nucleation density in this study ($4.5\times10^{13}/m^2$), the growth rate as well as the average size of precipitates will eventually become smaller than that in Ref. [137] after 12 months, as shown in Fig. 5.12. Moreover, thickness calculated from the Kirchner mechanism will become gradually larger than the results of the LSW mechanism, which will be discussed in detail later.

Fig. 5.13 shows the evolution of intergranular precipitate density for the total nucleation-growth-coarsening sequence. Because of the relatively low aging temperature (70℃), the nucleation really starts after 10^6 s, and the LSW coarsening mechanism finally leads to a higher nucleation density than the Kirchner model and our new model (see Fig.

5.13). For the model using the Kirchner coarsening mechanism, the coarsening fraction is much smaller than that of the LSW model as indicated in Fig. 5.14. In addition, the value of f_c for both the LSW and Kirchner mechanism is less than 5 % before 5×10^6 s (about 2 months), indicating the precipitate growth rate is much larger than the coarsening rate. Based on these two facts, the overall growth rate (calculated from Eq. (5.83)) of the Kirchner model is higher than the LSW model. Thus, the precipitate size of the Kirchner model tends to be larger than the LSW model. As we assumed above, all the nucleation happens within a layer of 0.5nm, and a larger average grain size results in a lower nucleation density (N).

In the growth and coarsening regime, the total nucleation number is constant for both the LSW and the Kirchner model. However, when the continuity ($\sqrt{N\pi R^2}$) becomes close to 1, the precipitate number density in the Kirchner model decreases sharply. Further examination reveals that the sudden change in the total number of precipitates was caused by the break down of Eq. (5.77). In Speight's model, [69] the concentration in the grain boundary at a distance (L), C_L, was treated as a constant. This simplification is reasonable when L is much larger than the radius of precipitates. However, when R is close to L, Eq. (8) in Ref. [69] will break down, as well as for the growth mechanism used in Kirchner's model. [67] As shown in Fig. 5.13, when the aging time approaches 1×10^8 s, the value of $[1/\ln(R_c/R)]$ enlarges 3×10^4 times, as well as for the coarsening rate. Henceforth, the number density changing rate of the coarsening stage goes below 0 as the aging time approaches 1×10^8 s (see Eq. (5.88)).

The coarsening fraction value of different mechanisms is shown in Fig. 5.14. In order to verify the validation of the coarsening fraction expression (Eq. (5.82)), the classical

intragranular precipitate nucleation, growth, and coarsening model was adopted in this study. Parameters listed in Table 1 of Ref. [137] were used to obtain the final precipitate radius, density, and the transformation fraction. The coarsening fraction values were shown in the inserted diagram of Fig. 5.14. Perez *et al.* [85] pointed out that the expression of coarsening fraction proposed by Deschamps and Brechet [94] was unable to predict the dissolution of precipitates (when $R<R^*$). Instead, they developed a more general expression, as follows:

$$f_c = 1 - 1000\left(\frac{R}{R^*} - 1\right)^2 \quad 0.99R^* < R < 1.01R^* \tag{5.91}$$

Both Eq. (5.91) and the expression derived by Dechamps and Brechet work well for the general case of intragranular precipitation, with the exception of some special cases like Al_3Sc precipitation in Al-0.12% Sc alloy. [162] The coarsening fraction obtained from our new expression is close to the existing two expressions. Moreover, a small peak, as indicated by a small arrow in Fig. 5.14, was observed when the aging time was as long as 10^3 seconds. Combining the nucleation density versus time result (Fig. 5.13) and Eq. (12) in Ref. [166], it is easy to find that the nucleation rate reaches a maximum at 10^3 seconds. Henceforth, the solute flux coming to the surface will decrease, and ultimately lead to the small peak of coarsening fraction. In other words, our coarsening expression is also valid in the nucleation and growth stage.

The coarsening fraction of the LSW mechanism can be as large as 10%, which is much larger than that (0.8%) of the Kirchner mechanism. This can be attributed to the different growth rate adopted in these two mechanisms

$$\text{Kirchner: } 3f_{PV}R^2\frac{dR}{dt} = 2\pi R\left(\delta_{eff}/2\right)D_b\left.\frac{dC}{dr}\right|_{r=R} \tag{5.92}$$

$$\text{LSW: } 3f_{PV}R^2\frac{dR}{dt} = f_{PA}R^2D_b\left.\frac{dC}{dr}\right|_{r=R} \tag{5.93}$$

If we assume the solute gradient at the surface of the precipitate is the same for Eqs. (5.92) and (5.93), and the final ratio of these two growth rates (Kirchner/LSW) can be estimated as δ_{eff}/R (the value of f_{PA} is around 3 in this study), as a result, the final coarsening rate of the Kirchner mechanism is far less than that of the LSW mechanism.

For the limiting case, $\left(N\pi R^2\right)\to 0$, $\ln(R_c/R)$ can be treated as a constant, and Kirchner's coarsening rate and particle size distribution function is obtained. Fig. 5.14 shows that a relatively small value of $\ln(R_c/R)$ leads to a slightly larger coarsening fraction, but the values are not far different from the variable case except at the place where it starts to break down (around 38.5 months). Ardell [70] pointed out that the volume fraction dependence of the particle size distribution will be sacrificed once $\ln(R_c/R)$ is simplified as a constant, which is not necessary. When $\left(N\pi R^2\right)\to 1$, the grain boundary will be fully covered by precipitates, indicating the precipitate growth equation developed by Zener [49] is valid. Thus the final coarsening rate equation and particle distribution function is of the same form as the well-known LSW mechanism for such conditions.

Aiming at deriving a more rigorous coarsening rate, Ardell [70] adopted an incomplete gamma equation to describe the relationship between interprecipitate spacing and the volume fraction of intergranular precipitates. However, because of the limitations of the incomplete gamma equation, there is a large deviation from the real case when $(N\pi R^2)\to 1$. In fact, Ardell's coarsening mechanism is firmly close to Kirchner's results by a factor of around 1.23. In our new model, the Kirchner coarsening mechanism will transfer continuously to the LSW mechanism with the aid of a factor f_L. It is apparent that f_L changes most rapidly when $(N\pi R^2)< 0.2$, as shown in Fig. 5.9, and after that f_L changes relatively little. Consequently, the thickness, continuity, and coarsening fraction results of the new model are close to the LSW mechanism, while the nucleation density result, which happens at the early stage of precipitation, is closer to the Kirchner mechanism model prediction.

Fig. 5.7 is a typical BF-STEM image of intergranular precipitates formed at the grain boundary of Al 5083 H131 aged at 70℃ for 30 months. The grain boundary was fully covered by a continuous precipitate film. Moreover, as we mentioned in previous research, [137] Mg concentration within the grain matrix is still high enough to support the further growth of β phase. Therefore, precipitate growth will dominate during the whole aging process of Al 5083 H131 before it becomes fully sensitized.

Fig. 5.15 shows the intergranular precipitate size distribution results predicted by the general steady-state particle size distribution expression derived in Ref. [70]. As shown in Fig. 5.15(a), for Al 5083 H131 alloy aged at 70℃ for 1 month, the precipitate size distribution results obtained from the general expression are far different from those predicted by the Kirchner and the LSW mechanism. In addition, comparing Fig. 5.15(a) and (b), the total precipitate number illustrates an increase largely because the nucleation

stage starts at around 10^6 s (2 months). Hereafter, the total number of precipitates is stable (see Fig. 5.15(b)) regardless of aging time, indicating the coarsening mechanism only accounts for a small fraction in the final growth rate at low exposure temperatures. In addition, the critical radius (R^*) and average radius (R) increases with aging time, and so does the ratio of R to R^*(see the inserted diagram in Fig. 5.15(b)). Based on Deschamps and Brechet [94] and Perez *et al.*'s [85] criterion, the coarsening stage will start before 40 months, which is not satisfactory in our study. As a matter of fact, a previous study [85] revealed that the criterion $R/R^*\approx1$ is only a necessary condition, but not a sufficient condition to establish the start of the coarsening stage. Instead, the precipitate size distribution results are more effective in predicting the inception of coarsening. Since the coarsening of larger precipitates is at the expense of the smaller ones, there must be enough small particles to initiate coarsening. In this study, the precipitate size distribution pattern does not change too much from 10 to 40 months, as shown in Fig. 5.15(b), suggesting coarsening is not prevalent even at the end of aging.

$MgZn_2$ precipitates are the main hardening particles formed in Al 7xxx alloys, [167,168] and the size and distribution of intergranular $MgZn_2$ strongly influence the properties of the alloy. [169,170] Considerable research has been reported on the characterization and modeling of $MgZn_2$ precipitates. [60–62,171,172] In order to examine the performance of the new model at high temperature, the evolution of $MgZn_2$ precipitates at grain boundary will be predicted and compared with existing experimental and modeling results. Parameters used for the modeling are extracted from Table 2 in Ref. [60]. Fig. 5.16 (a) and (b) shows the radius and interparticle spacing of intergranular $MgZn_2$ during isothermal heat treatment at 180℃. The new model gives a good description of both the interparticle

spacing and radius of $MgZn_2$. In addition, the prediction results using Jiang [60,61] and Yi's [137] models are also shown in Fig. 5.16. Even though the radius of intergranular precipitates obtained from the model in Ref. [137] agrees reasonably well with experimental results (when N=2.147×10^{14}), as shown in Fig. 5.16(a), the model fails to predict the increase of interparticle spacing (see Fig. 5.16(b)) because the coarsening effect is not considered. Thus, the new model works both for the low and high aging temperature scenarios, whereas the existing model does not. Moreover, when coupled with the nucleation and growth model in this study, the combined coarsening mechanism performs a better prediction than the LSW and Kirchner coarsening mechanism at 180℃.

Moreover, the nucleation density result versus time is given in Fig. 5.16 (c). An obvious decrease in the nucleation density was observed after the nucleation and growth stage, suggesting coarsening did take place at the end of aging. Further evidence can be obtained from the size distribution results of precipitates, as shown in Fig. 5.16 (d). Instead of locating within a narrow range (aged for 0.5 hour), the precipitate size distribution was highly enlarged (aged for 10 hours) and enough small precipitates were generated for coarsening to occur. At 180℃, the rate controlling element, Mg, in Al 7xxx alloy (Al 7150) is not supersaturated (only 2.4wt. %), thus the grain matrix will become depleted in Mg very quickly, which leads to the end of growth and inception of coarsening. Both Jiang [60,61] and Hass's [173] model adopted the Kirchner coarsening mechanism, which is reasonable for their cases because of the low Mg atom flux to the grain boundary. Moreover, TEM results in their work revealed that precipitates only occupied a small part of the grain boundary (R/R_c is small), thus the coarsening mechanism will not break down either.

An equivalent average Mg concentration at the grain boundary was derived in this study. In fact, several attempts have been made to obtain Mg concentration profiles along the grain boundary by Hoyt, [73] Chaix *et al*. [174] and Brailsford and Aaron. [56] However, it appears that further assumptions are needed to obtain enough boundary conditions to solve the steady-state diffusion equation. The assumption we adopted, $(\partial C_\beta / \partial r)_{r=R_c} = 0$, comes from the collector plate mechanism assumption that the solute flux arriving at the collector plate only contributes to the growth of precipitate in that collector plate. This treatment is indeed the same as the assumption of Brailsford and Aaron, [56] who obtained the Mg concentration along the grain boundary by solving a modified Bessel function. The evolution of nucleation density, thickness and continuity of β phase predicted using the equivalent average Mg concentration was consistent with the experimental results, consequently our treatment is reasonable.

Table 5.1 Parameters used in the model of intragranular precipitates.

Parameters	unit	value	Reference source
N	m^{-3}	6.02×10^{28}	[141]
k	$J\cdot K^{-1}$	1.38×10^{-23}	
T	℃	50 & 70	
$v_{at,GPzone}$	m^3	1.65×10^{-29}	[35]
$v_{at,\beta''}$	m^3	1.70×10^{-29}	[35]
$v_{at,\beta'}$	m^3	1.93×10^{-29}	[35]
$v_{at,\beta}$	m^3	1.93×10^{-29}	[35]
a_0	m	4.04×10^{-10}	[85]
M	$m^2\cdot s^{-1}$	$5.7\times10^{-5}\exp(-112499/R_CT)$	[175]
γ_{GPzone}	$J\cdot m^{-2}$	0.09	
$\gamma_{\beta''}$	$J\cdot m^{-2}$	0.15	
$\gamma_{\beta'}$	$J\cdot m^{-2}$	0.25	
γ_{β}	$J\cdot m^{-2}$	0.6	
$X_{0,m}$	at.%	5.25	

Table 5.2 Parameters for the modeling of intergranular precipitates.

Parameters	Unit	Value	Source
k	J/K	1.3806488×10^{-23}	
T	ºC	70	
ψ	°	20.5	[137]
γ	J/ m^2	0.07	[162,163]
C_α	wt.%	4.85	
C_β	wt.%	2.9	[137]
$C_{\alpha\beta}$	wt.%	32	
h	m	1×10^{-6}	
D_m	m^2/s	$1.49\times10^{-5}\exp(-120500/RT)$	[176,177]
D_b	m^2/s	$0.65\times10^{-4}\exp(-110500/RT)$	[58,59]
D_s	m^2/s	$0.45\times10^{-4}\exp(-105750/RT)$	[56]
δ_{eff}	m	0.5×10^{-9}	[164,165]
v_{at}^{P}	m^3	1.6×10^{-29}	[85]
a_0	m	4.04×10^{-10}	[85]
N_{0hom}	$\#/m^3$	6.02×10^{28}	[85]

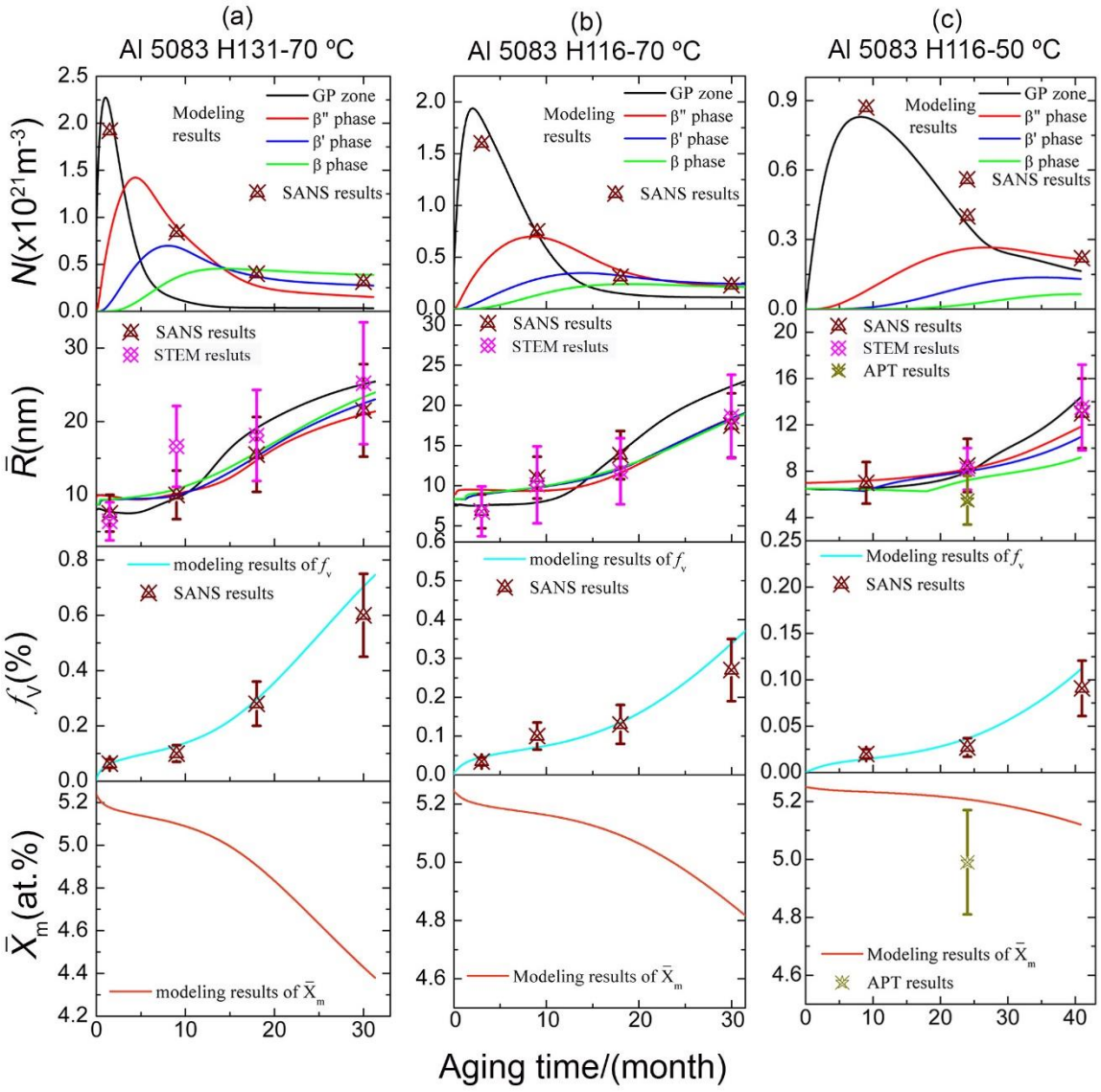

Figure 5.1 Evolution of the number density *N*, average radius $\bar{R}$, volume fraction f_v, and average Mg concentration $\bar{X}_m$ in the matrix as a function of aging time for (a) Al 5083 H131 (70℃) and H116 ((b) 70 and (c) 50℃) alloys and the corresponding STEM, SANS, and APT experimental results.

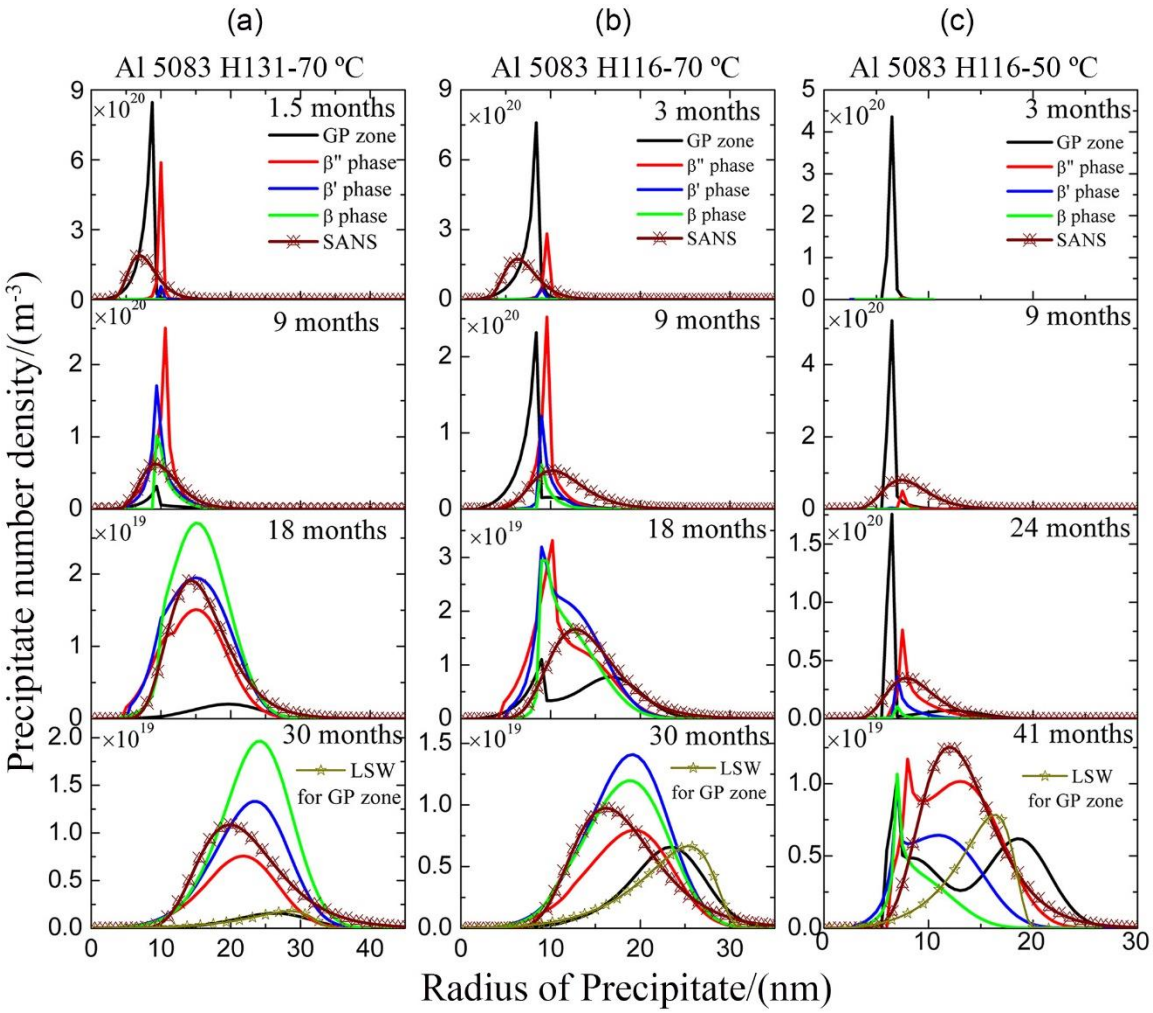

Figure 5.2 Experimental and modeling results of particle size distribution of precipitates formed in (a) Al 5083 H131 aged at 70℃ and Al 5083 H116 aged at (b) 70℃ and (c) 50℃.

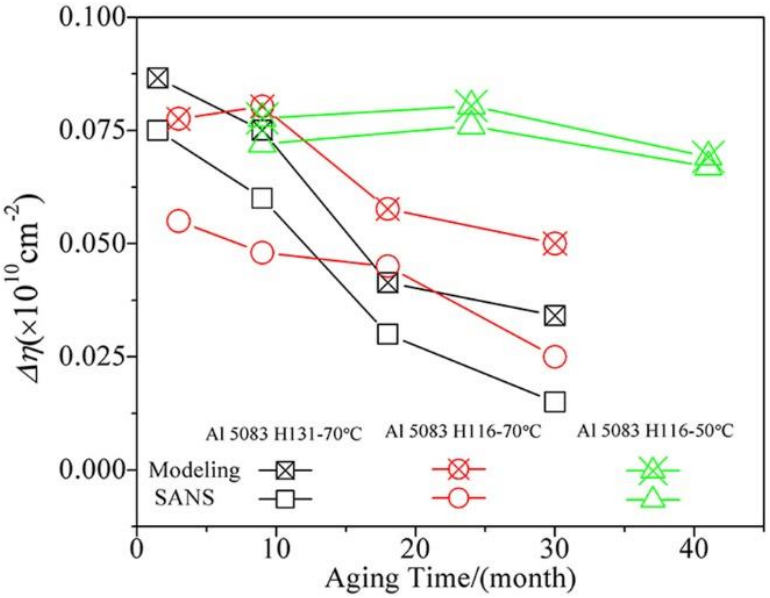

Figure 5.3 Comparison of scattering length difference for Mg-rich precipitates formed in Al 5083 H131 and H116 aged at 50 and 70°C obtained from SANS fitting and calculation of modeling results.

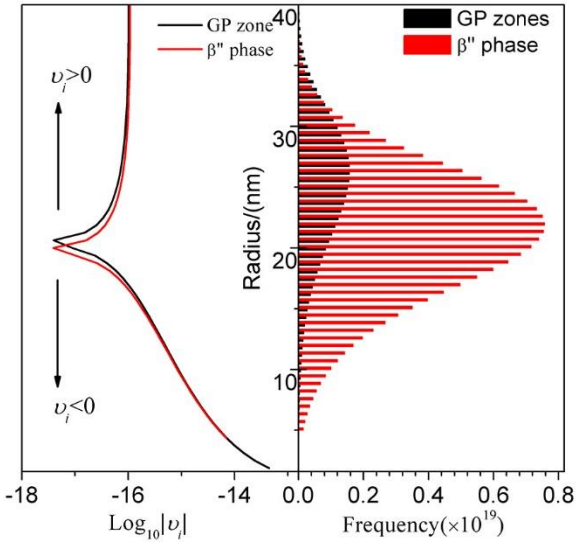

Figure 5.4 Comparison of growth rate (left side) and PSD (right side) of GP zones and β" phases formed in Al 5083 H131 aged at 70°C for 30 months.

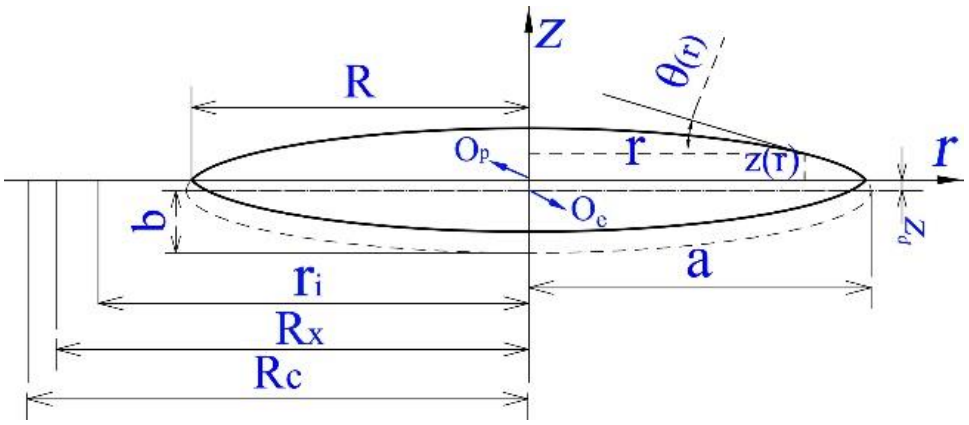

Figure 5.5 Schematic of β phase (the solid line) formed at the grain boundary, showing the half-thickness [$z(r=0)$], half-length (R), radius of collector plate (R_c), semi-major axis (a), semi-minor axis (b) of the ellipse (the dashed line). The coordinate of any point on the ellipse is given as [r, $z(r)$], and $\theta(r)$ is the angle between r and the tangent line of point [r, $z(r)$]. O_p and O_e are the origin of β phase and the ellipse respectively. z_d is the difference between b and [$z(r=0)$]. R_x and r_i are the distance to the center of the precipitate within the collector plate surface, and $R_c > R_x > r_i > R$.

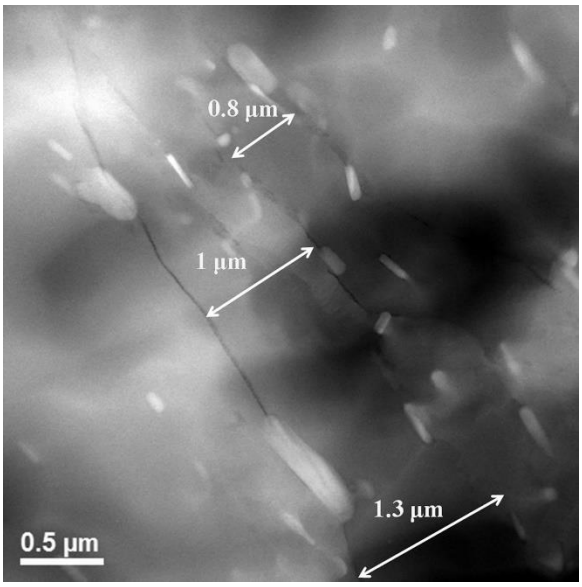

Figure 5.6 TEM image showing grain size measurements in Al 5083.

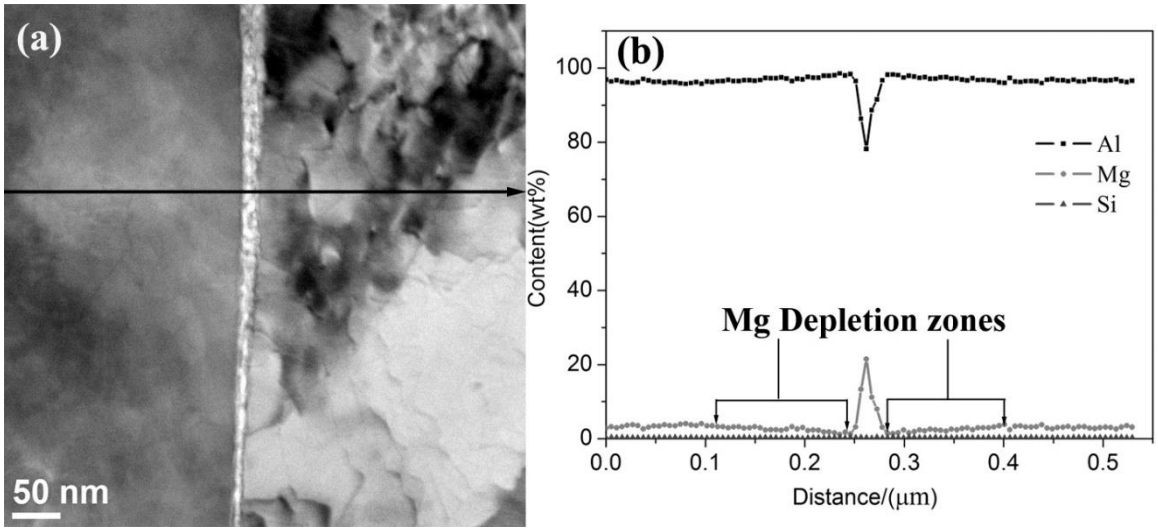

Figure 5.7 TEM and EDS results of Al 5083 aged at 70℃ for 30 months (a) TEM image of β phase formed at the grain boundary and, (b) EDS line scan results obtained across the β phase as indicated by the dark arrow in (a).

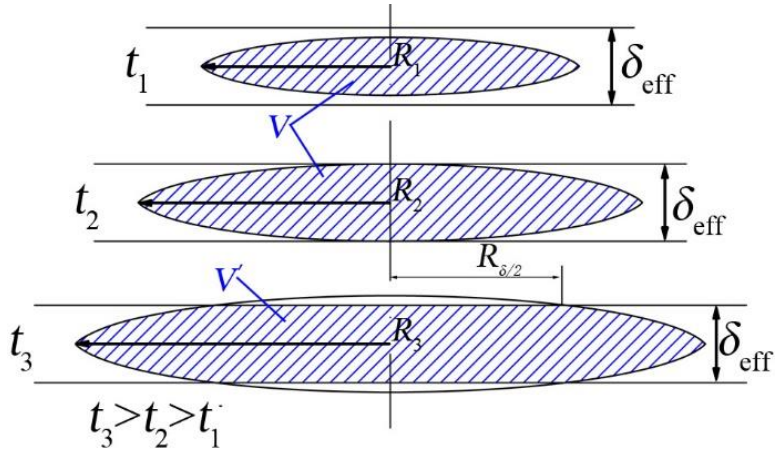

Figure 5.8 Diagram of the relative dimension of grain boundary and intergranular precipitate at different times.

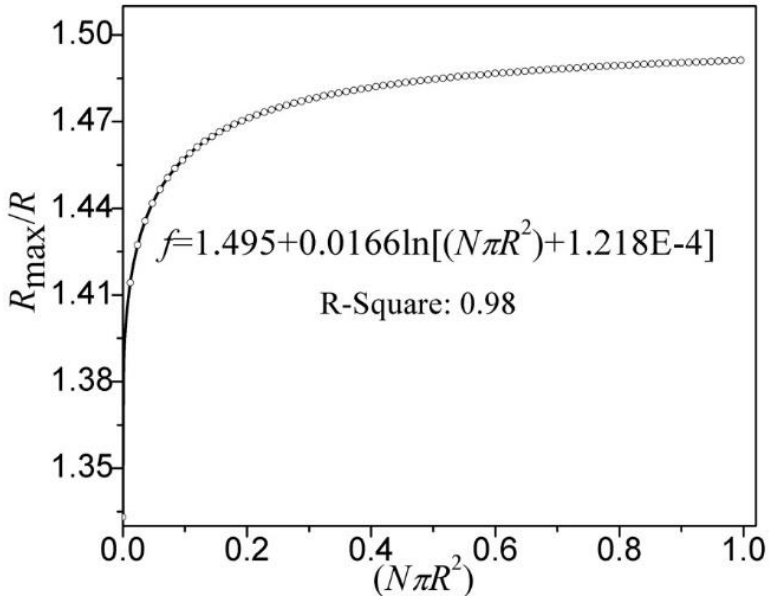

Figure 5.9 Illustrating the dependence of R_{max}/R on ($N\pi R^2$).

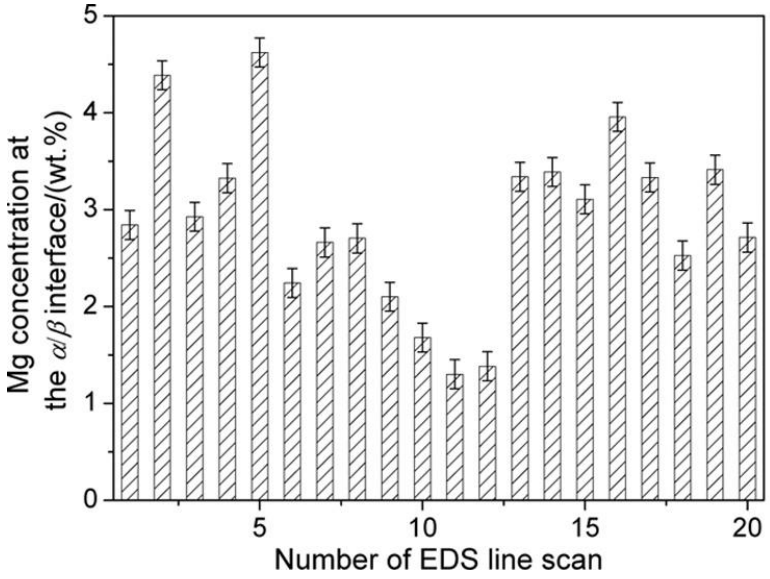

Figure 5.10 EDS line scan results of $C_{\alpha\beta}$.

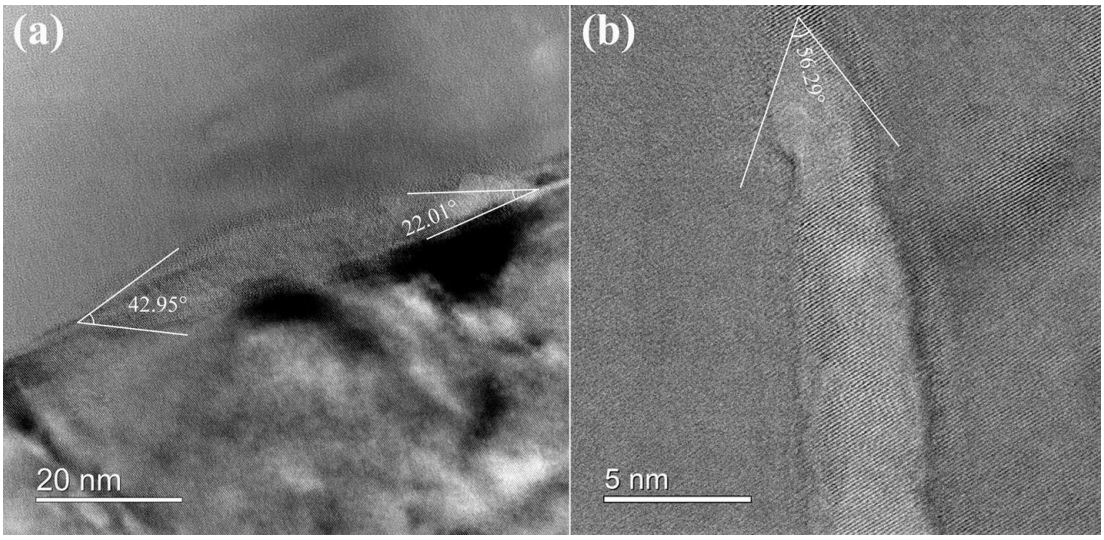

Figure 5.11 Contact angle of β phase at grain boundaries.

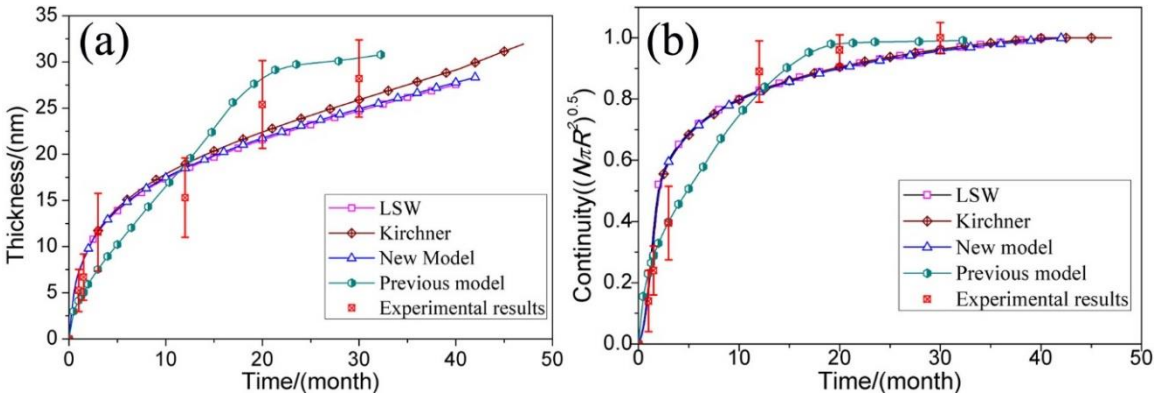

Figure 5.12 Comparison of experimental and modeling results of thickness (a) and continuity (b) of β phase at the grain boundary of Al 5083 H131 aged at 70℃ for different times.

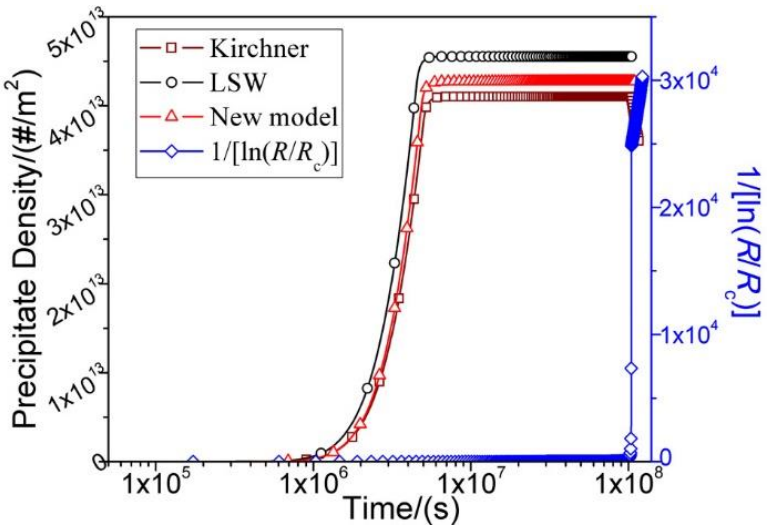

Figure 5.13 Nucleation density of intergranular β phase predicted by the LSW and Kirchner model (left y axis), and the value of [1/(lnR_c/R)] at different time (right y axis).

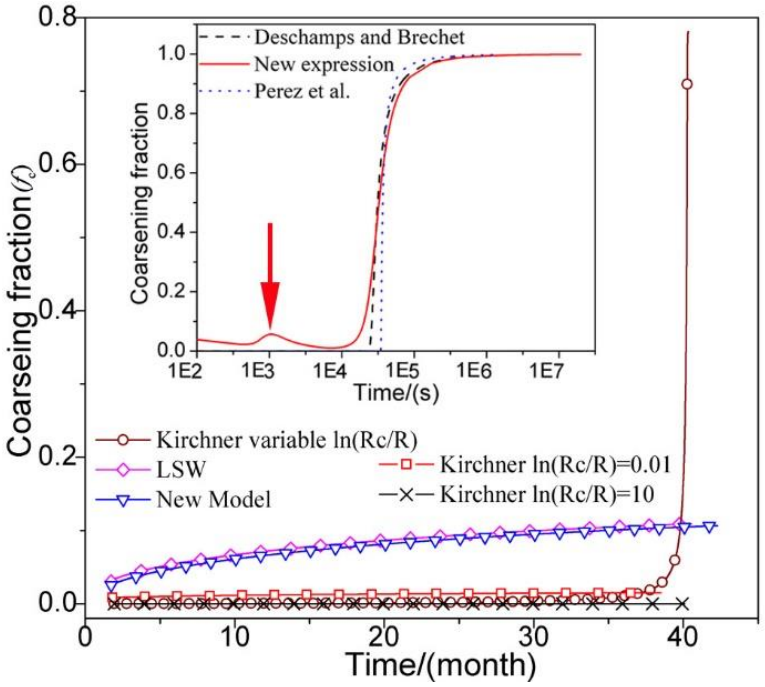

Figure 5.14 Coarsening fraction value (f_c) of the LSW model and the Kirchner model (including variable and constant ln(R_c/R)), inserted diagram is the coarsening fraction of intragranular precipitate using different expression for coarsening.

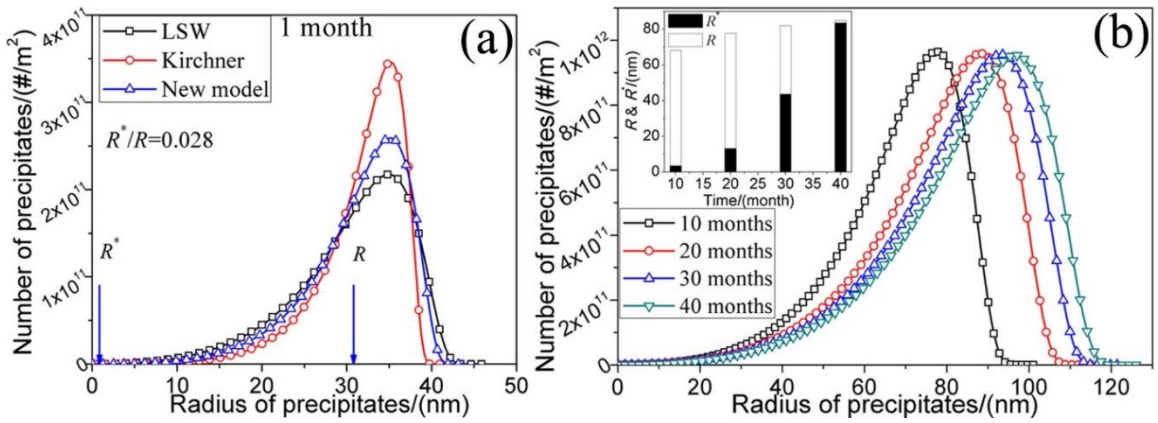

Figure 5.15 Particle size distribution of intergranular β phase (a) at 1 month obtained from the LSW, Kirchner and the new model, and (b) particle size distribution of intergranular β phase at 10, 20, 30, and 40 months, and the corresponding critical (R^*) and average (R) radius of precipitate predicted by the new model.

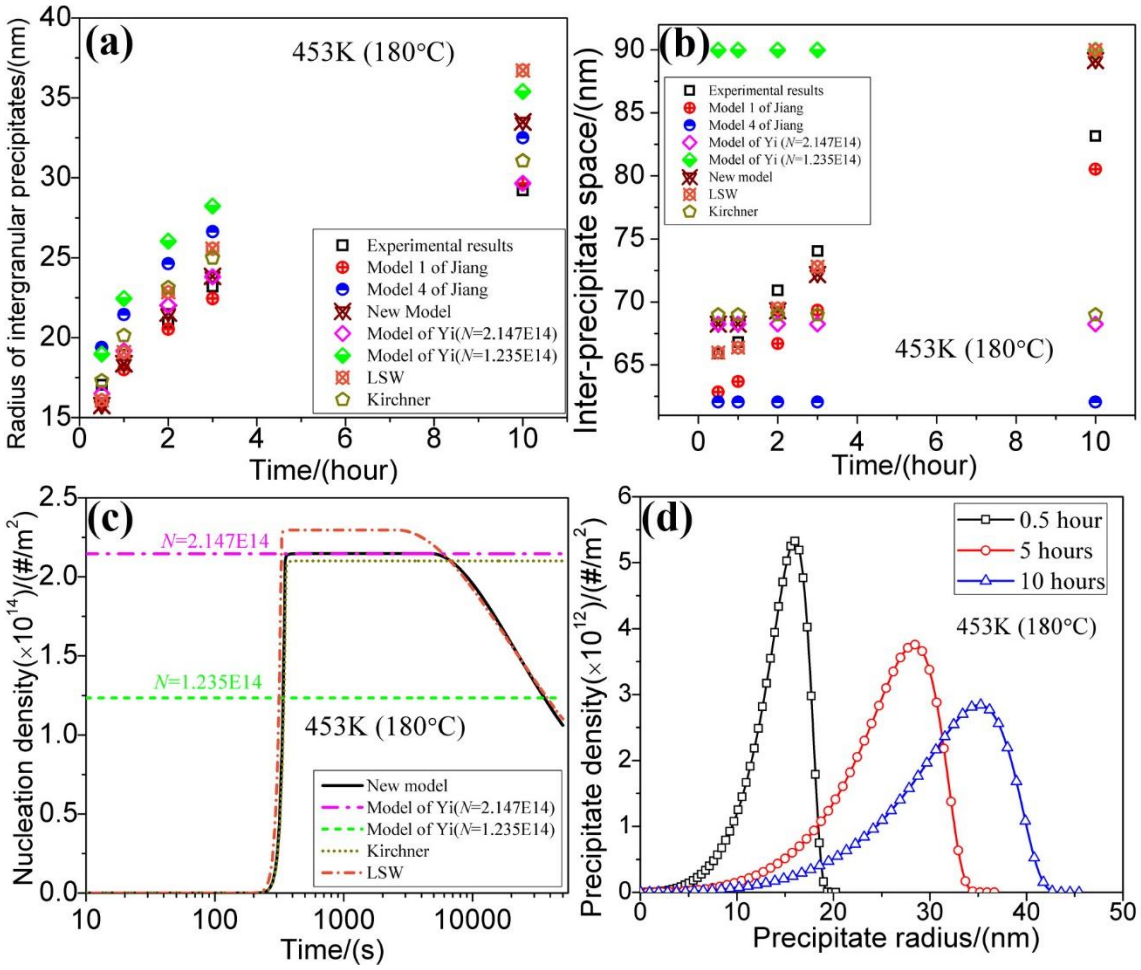

Figure 5.16 Experimental and modeling results of radius (a) and inter-particle spacing (b), and the evolution of nucleation density (c) and the particle size distribution (d) of intergranular precipitates formed in Al 7150 alloy aging at 180℃.

CHAPTER 6

INTERGRANULAR CORROSION OF Al 5XXX ALLOYS

In this chapter, the intergranular corrosion behavior of Al 5xxx alloys was investigated using SEM, AFM, and ASTM G67 mass loss test. In addition, a preliminary model based on continuity of intergranular precipitates was developed to predict mass loss.

6.1 Etching of intergranular precipitates

6.1.1 SEM results of intergranular precipitates etching experiments

In order to explore the IGC behavior, Al 5083 H131 sample aged at 70℃ for 12 months was etched using HNO_3 at room temperature for 1, 3 and 5 minutes. Each time, after etching, the sample will be dried and observed under SEM. Fig. 6.1 (a) is the SEM image of sample etched for 1 minute. Only two grain boundaries can be observed, and the distance between these two grain boundaries is about 40 μm. When etching time increases to 3 minutes (see Fig. 6.1 (b)), more grain boundaries become apparent, and the smallest distance between two grain boundaries is only 3 μm. Even more grain boundaries can be observed when etching time is as long as 5 minutes, as shown in Fig. 6.1 (c). And the distances between these boundaries are smaller than 5 μm. Based on the results of the etching experiments, one can conclude that some grain boundaries are less corrosion resistant than other grain boundaries.

6.1.2 AFM results of intergranular precipitate etching experiments

Fig. 6.2 (a) to (c) are AFM images of grain boundaries of Al 5083 H131 (aged at 70℃ for 30 months) etched by HNO_3 (70 vol.%) for 2 minutes. Three types of grain boundaries are shown in Fig. 6.2 (a), (b), and (c), respectively. In Fig. 6.2(a), the boundary is continuous, and the width and depth of the boundary is 100 nm and 8 nm, as shown by the height line scan across the grain boundary. For the grain boundary in Fig. 6.2(b), only a small part is etched by the phosphoric acid, and the width and depth of the grain boundary is only 40 nm and 1.5 nm. The grain boundary in Fig. 6.2(c) is different from the two grain boundaries in Fig. 6.2(a) and (b). The width of the grain boundary is 100 nm, but it is discontinuous and the etching depth is only 5 nm.

6.2 NAMLT of constant thermal exposed sample

For Al 5xxx alloys, the degree of sensitization caused by intergranular corrosion was obtained from ASTM G67 nitric acid mass loss test (NAMLT) results. Fig. 6.3(a) presents the results of NAMLT for Al 5050, 5052, 5083, and 5154 alloys. The final mass loss of Al 5050, 5052, and 5154 alloys aged at 70℃ for 31 months is still less than 5 mg/cm^2, which is attributed to the low Mg concentration in them (1.4wt.% for Al 5050, 2.5 wt.% for Al 5052, and 3.5wt.% for Al 5154). However, there is still an obvious increase in mass loss versus aging time, as shown by the inserted image in Fig. 6.3(a), indicating sensitization occurs gradually in these alloys. For Al 5083 (4.85 wt.% Mg) H32, mass loss increases rapidly in the first 9 months, and then reaches a plateau around 50 mg/cm^2 after that. Fig. 6.3 (b), (c), and (d) show the mass loss versus time relationship of Al 5083 H131, H116, and Al 5456 H116 aged at different temperatures (40, 50, 60, and 70℃). Before they

become fully sensitized, the mass loss for elevated temperature exposure is higher than that for a low-temperature exposure as shown in Fig. 6.3(b), (c), and (d). For all the three types of alloys (Al 5083 H131, H116 and Al 5456 H116), mass loss increases with time at the early aging stage, and a plateau (around 50 mg/cm^2) is reached eventually, as shown by the NAMLT results at 60 and 70℃ for all three alloys. Moreover, when aging time is as long as 57.5 months, the mass loss of Al 5083 H131 and Al 5456 H116 will also increase to a similar plateau level of 50 mg/cm^2 in spite of a relatively lower exposure temperature (50℃). The mass loss of Al 5083 H116 is only 15.6 mg/cm^2 (40℃) and 42.1mg/cm^2 (50℃) after 57.5 months of exposure, revealing this alloy provided exceptional resistance to intergranular corrosion. As stated by Zhu *et al*.,[178] for the same aging temperature and aging time, the mass loss sequence for these three alloys is Al 5456 H116>Al 5083 H131>Al 5083H116.

6.3 NAMLT of cyclic thermal exposed sample

In order to simulate the daily outdoor cyclic thermal exposure of Al 5xxx alloys due to sunlight, three different cyclic aging experiments were set up. The mass loss results of the cyclic aging experiments are given in Fig. 6.4. For all the three cyclic aging temperature profiles, NAMLT results increase with aging time, and there is also a mass loss plateau (approximately 50 mg/cm^2) for the 30-70℃ and 50-70℃ aging case. Furthermore, for the same aging time, mass loss for the 50-70℃ is slightly larger than that of the 30-70℃ experiments, and the 40-45℃ experiments showed low mass loss values.

6.4 ASTM G67 mass loss prediction model

The continuity versus time results of Al 5083 H116 (Fig. 6.5(a)) and H131 (Fig. 6.5(b)) aged at constant temperatures were obtained from the model in Chapter 5. For the 70℃ aging experiments, the continuity of Al 5083 H131 and H116 increases rapidly with time at the early stages of aging. This could result from the combined effects of collector plate growth as well as the high Mg concentration gradient adjacent to the grain boundary at the beginning of aging. Thereafter, the continuity growth rate decreases as a result of constant area collector plates and the smaller Mg concentration gradients within the grain matrix. When aging temperature decreases to 60℃, the slope of the continuity versus time plot at the early stage of aging also decreases because of the reduced Mg diffusivity at the lower temperature, which leads to a slower collector plate growth rate as well as less Mg flux coming from the matrix. The same trend was also observed in the 40 and 50℃ results for both types of alloys.

In order to apply the β phase growth model to the cyclic aging experiments, a minor modification was made. As stated in Chapter 5, at the early stage of aging, the collector plate varies with time, and the area of the collector plate is given as

$$\overline{A} = \pi(2\sqrt{D_b t})^2 = 4\pi D_b t \tag{6.1}$$

where D_b is the diffusion coefficient of Mg at the grain boundary, and t is aging time. For cyclical aging, temperature change will lead to a variation of the diffusion coefficient D_b. This variation can cause an error for the numerical solving process. Therefore the Euler

equation is used to calculate the collector plate area $\overline{A}$ for the case of cyclical thermal exposure:

$$\overline{A}(t+\Delta t) = \overline{A}(t) + \frac{d\overline{A}}{dt}\Delta t \tag{6.2}$$

where $d\overline{A}/dt$ /can be obtained from Eq. (6.1). The rest of the numerical solution process is the same as for the constant temperature case.

6.5 Results and discussion

Fig. 6.6 shows the continuity results of the cyclic aging experiments obtained from the modified model in Chapter 5. As shown in Fig. 6.6(a), the continuity increases rapidly at the early stages of aging and then the precipitate growth rate decreases slowly, which resembles the results of constant-temperature aging experiments. However, further examination reveals that there is a slight difference between the cyclical and constant thermal exposure continuity results. The detailed shape of the cyclic time-continuity plot (Al 5083 H116) of the 30-70℃ experiment is shown as an inserted image in Fig. 6.6(a). Within 24 hours (2 aging cycles), the continuity initially has a fast growth rate, and it is followed by a relatively slow growth rate before it increases its growth rate again. The variation in growth rate can be attributed to the cyclic aging temperature. For one aging cycle (0 to 12 hours), the aging temperature increases from 30℃ to 70℃ (in 6 hours) gradually, and drops down gradually to 30℃ (12^{th} hour) again. Correspondingly, the rate of increase of continuity will increase from minimum to maximum because of the temperature-controlled Mg diffusion rate, which changes with time. Additionally, the

amount of continuity increase for two consecutive aging cycles is shown in the inserted image of Fig. 6.6(a). The data show that the early aging cycles experience a faster growth rate (by 0.8×10^{-5}) than the latter aging cycles (0.55×10^{-4}). As a matter of fact, the cyclical time-continuity plot is more similar to the actual natural outdoor exposure than the constant aging situation. Fig. 6.6(b) shows the continuity prediction results of Al 5083 H131 aged at different cyclical temperature profiles for 30 months, which shows the same trend as that for Al 5083 H116, except for larger final continuity values. The experimental continuity results were obtained from STEM images as shown in Fig. 4.19 (Al 5083 H131 aged at 30-70℃ for different times), and the modeling results presented in Fig. 6.6 agree well with experimental results.

The relationship between ASTM G-67 mass loss and the continuity of intergranular β phase has been explored by many researchers. Lim *et al.* [179] and Jain *et al*. [121] obtained the continuity of intergranular β phase from SEM images of Al 5083 H131 aged at 100℃ for different times and etched by phosphoric acid at 50℃ for 30 seconds. Their results indicate that larger NAMLT results are accompanied with a higher continuity of β phase at grain boundaries. In addition, the penetration rate in different directions (longitudinal, transverse, and short transverse) are found to be different. Steiner and Agnew [180,181] developed a mass loss prediction model for isothermal and nonisothermal cases based on a modified JMAK model and an assumption that there is a linear relationship between continuity and mass loss. Derrick [182] developed a mass loss prediction model based on three corrosion rates (corrosion rate of β phase, corrosion rate of clean grain boundary, and corrosion rate of intermediate material). Fig. 6.7 shows the relationship between mass loss and continuity of Al 5083 H131 aged at 70℃ for different times (for the unsensitized Al

5083 H131, mass loss is 3±1 mg/cm^2, and continuity is 0). Considering the limited number of continuity results as well as the noisy mass loss data, it is not reliable to predict a new relationship between mass loss and continuity. Thus, we adopted the same assumption in Ref. [179] and [121] that continuity is linearly related to mass, and the R-squared value of the linear fit is 0.9 as shown in Fig. 6.7.

Fig. 6.8 shows the modeling results of ASTM G-67 mass loss together with the experimental results for Al 5083 H116 and H131 aged at constant temperature for different times. The modeling results (3D surface) match well with the experimental results (see cubes of different colors in Fig. 6.8). As shown in Fig. 6.8 (a), the red part of the surface represents mass loss larger than 30 mg/cm^2. From 55 to 70℃, increasing the aging temperature shortens the aging time needed to reach 30 mg/cm^2. The mass loss for the 40 and 50℃ aging experiments is still lower than 30 mg/cm^2 after 30 months. The modeling results of Al 5083 H131 (Fig. 6.8(b)) show the same trend as that of Al 5083 H116. However, for Al 5083 H131 only the mass loss for the 40℃ experiment is smaller than 30 mg/cm^2. Comparing Fig. 6.8 (a) and (b), it is obvious that there are larger red areas (mass loss> 30 mg/cm^2) but smaller blue and purple (mass loss <15 mg/cm^2) areas for Al 5083 H131 than for Al 5083 H116. These data show it is easier for Al 5083 H131 to become sensitized (based on the 30 mg/cm^2 mass loss standard), which means Al 5083 H116 is more corrosion resistant.

The mass losses of cyclic aging experiments of Al 5083 H116 and H131 are presented in Fig. 6.9 (a) and (b), respectively. For Al 5083 H116 (Fig. 6.9(a)) aged at 50-70℃ and 30-70℃, mass loss of these two experiments increases sharply during the first 10 months, and after that, mass loss increases at a slower rate. The modeled mass loss for

the 50-70℃ experiment is slightly higher than that of the 30-70℃ experiment, but the difference between them decreases with time. When aged at 50-70℃ and 30-70℃, the modeled mass loss for Al 5083 H131 also increased rapidly at first, as shown in Fig.6.9 (b). But it only takes 5 months before the rate of mass increase slows, indicating Al 5083 H131 is more susceptible to sensitization than Al 5083 H116 when exposed to the same cyclical temperature profile. Moreover, the modeled mass loss of the 50-70℃ and 30-70℃ cyclical experiments reaches the same level at 30 months, revealing less time is needed for the Al 5083 H131 to reach the mass loss plateau. The modeled mass loss of these two alloys agrees well with the experimental mass loss.

Table 6.1 shows the time needed to reach ASTM G-67 mass loss levels of 25 and 40 mg/cm^2. For the same degree of sensitization, Al 5083 H116 requires more time than Al 5083 H131 if the aging temperature is the same. The longest predicted time to a sensitization level of 40 mg/cm^2 is 177.4 months for Al 5083 H116 aged at 40℃.

Mg concentration is reported to have a significant effect on the DoS of Al 5xxx alloys. [11,178,183] Dix *et al.* [11] investigated the stress corrosion behavior of Al alloys of different Mg concentrations, which led to a conclusion that Al alloys with a relatively high Mg concentration (>3%) are not recommended for use at elevated temperature (> 65.6℃) for a prolonged period of time. Recently, Gupta *et al.* [183] performed research on Al alloys of different Mg concentrations (varying from 3.36 wt.% to 8.85 wt.%), and their results revealed that if Mg concentration is higher than 4.01 wt.%, mass loss will increase monotonically with Mg concentration. In the present study, 6 alloys (Al 5050 H32, 5052 H32, 5154 H32, 5083 H131, 5083 H116, and Al 5456 H116) were examined. Mg concentrations for Al 5050, 5052, and 5154 are 1.4wt.%, 2.5wt.% and 3.5wt.%,

respectively, [184] and the mass loss for all the three alloys is smaller than 5 mg/cm^2 after 31 months of exposure to 70℃, which is consistent with Gupta *et al.*'s results [183] that Al alloys with low Mg concentrations (3.36 wt.%) are to some extent immune to sensitization. However, a sensitization trend was observed for Al 5154 H32 (3.1-3.9 wt.% Mg) aged at 70℃, and given an even longer aging time (> 30 months), it is possible that this alloy will become sensitized as stated by Dix *et al.* [11] Moreover, compared with Al 5050, 5052, and 5154, a sharp increase in mass loss was observed for Al 5083 H32 aged at the same temperature for the same time, which can be attributed to the higher Mg concentration of Al 5083 (4.85wt.%).

The effect of temperature on the sensitization of Al 5xxx alloys has been reported in previous research. As the growth of intergranular β phase results from Mg atoms diffusing from the matrix, a higher aging temperature will lead to greater Mg diffusivity as well as faster β phase growth. [137] However, the driving force for Mg atom diffusion is also temperature dependent. Mg saturation concentration within the matrix will increase with increasing temperature as shown by the equilibrium phase diagram for Al-Mg alloy, [11] therefore less Mg will be available if aging temperature increases. For Al 5083 and Al 5456, when aging temperature increases from 40℃ to 70℃, the results of NAMLT also increase until they become fully sensitized. EDS line scan results [137] show that there is still enough Mg for further growth of β phase after aging at 70℃ for 30 months. The low mass loss of Al 5050, 5052, and 5154 alloy can be attributed to a low thermodynamic diffusion driving force for Mg atoms diffusions.

In order to investigate the effect of grain size on the sensitization behavior of Al 5083 Alloy, Sikora *et al.* [185] compared the sensitization behavior of nanocrystalline Al 5083

alloy (grain size:80-200 nm) and traditional commercial Al 5083 alloy, and associated ASTM G-67 mass loss results indicated that the nanocrystalline Al 5083 alloy is more susceptible to IGC. However, Kus *et al.* [186] reported that nanocrystalline Al 5083 alloy was not susceptible to IGC as determined from the results of NAMLT. Further research by Birbilis *et al.* [48] and A.J. Davenport *et al.* [12] reveals that mass loss is not only related to grain size, but is also affected by the fraction of high-angle grain boundaries (HAGB). According to previous research, [133] the grain thicknesses of Al 5083 H131, H116, and Al 5456 H116 used in this study are 21.3, 32.5, and 13.8 μm as obtained from EBSD. Fig. 6.10 shows the grain boundary misorientation angle distribution, where high-angle is defined as misorientation that is larger than 15 degrees, low-angle is defined as misorientation that is smaller than 5 degrees, and medium angle misorientation is selected for the range between 5 and 15 degrees. For Al 5456 H116, the fraction of HAGB is larger than it is for Al 5083 H116 and H131, and its grain size is the smallest among the three alloys. For Al 5083 H116, even though it has a slightly larger fraction of HAGB (0.19) compared with that of Al 5083 H131 (0.14), it has a larger grain size, which contributes to low DoS.

Table 6.1 Predicted time needed to different levels or degrees of sensitization for Al 5083 H116 and H131.

Aging temperature/(℃)	Time to 25 mg/cm^2 (month)		Time to 40 mg/cm^2 (month)	
	5083H116	5083H131	5083H116	5083H131
40	103.8	44.1	177.4	73.1
50	31.5	9.6	54.1	29.7
60	8.1	5.3	28.5	17.2
70	3.3	1.8	12.6	11.7
40-45	50.5	30.7	76.1	38.8
30-70	7.1	3.8	16.3	14.5
50-70	5.3	2.6	13.9	12.6

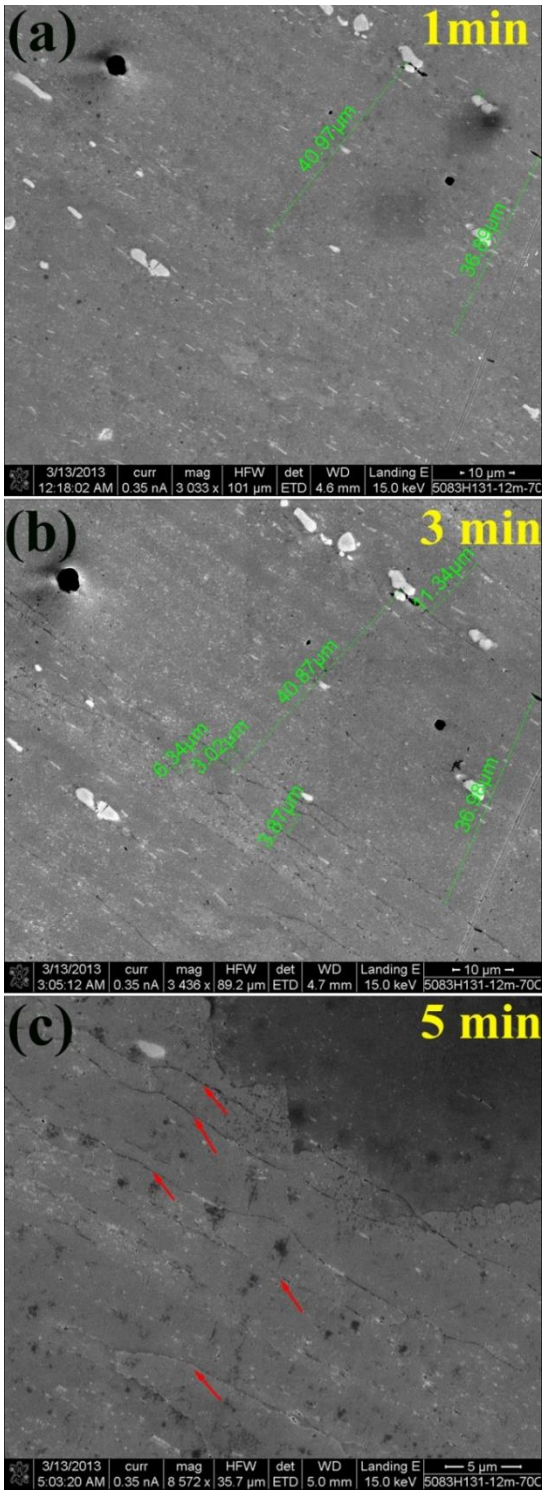

Figure 6.1 SEM image of Al 5083 H131 (aged at 343 K for 12 months) etched by HNO_3 for (a) 1 min, (b) 3 min, and (c) 5 min.

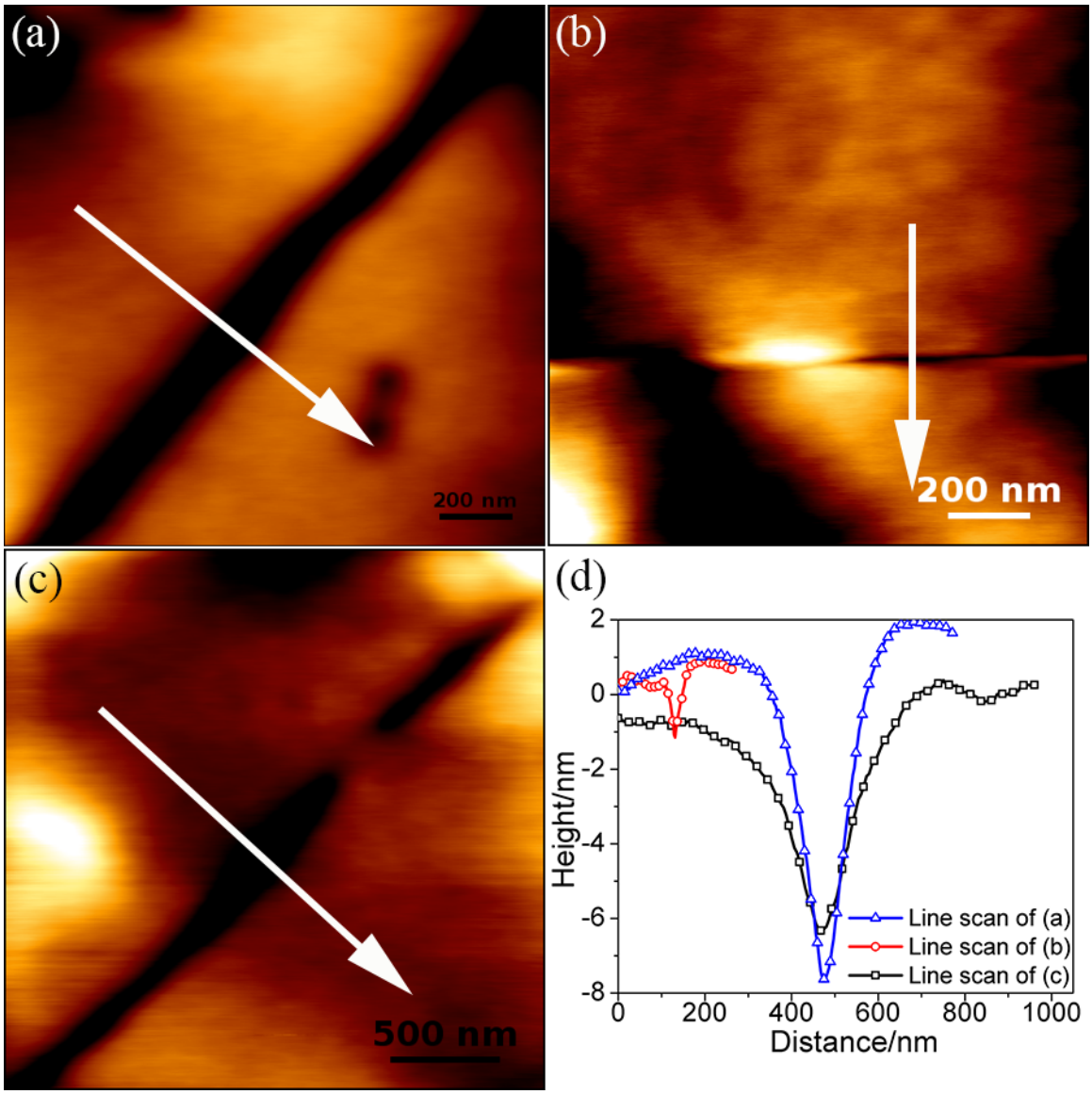

Figure 6.2 Height trace image of grain boundaries (Al 5083 H131 aged at 70°C for 30 months) etched using 10 vol.% H_3PO_4 for 2 minutes and the corresponding height distribution results.

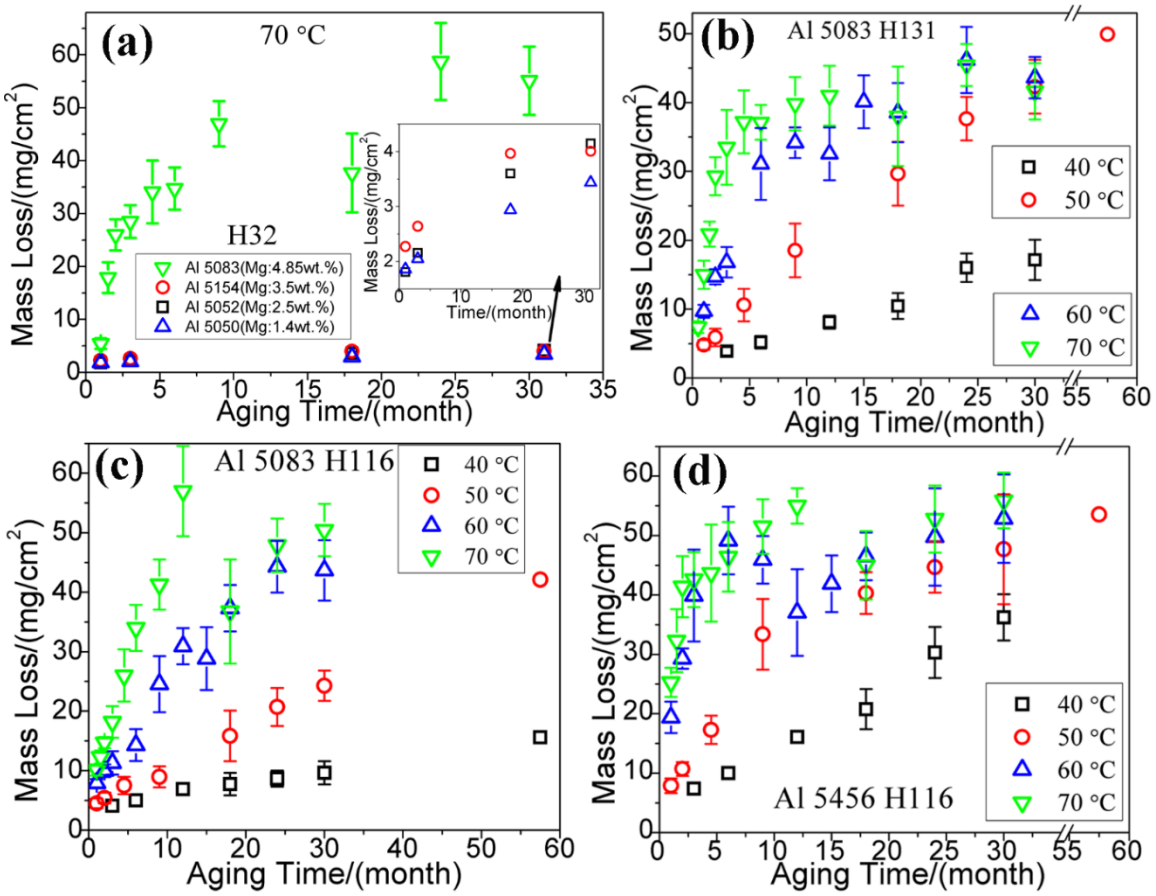

Figure 6.3 Results of ASTM G-67 nitric acid mass loss tests for (a) Al 5050, Al 5052, Al 5154, and Al 5083 H32, (b) Al 5083 H131, (c) Al 5083 H116, and (d) Al 5456 H116 aged at different temperatures (40, 50, 60, and 70°C) for a long time.

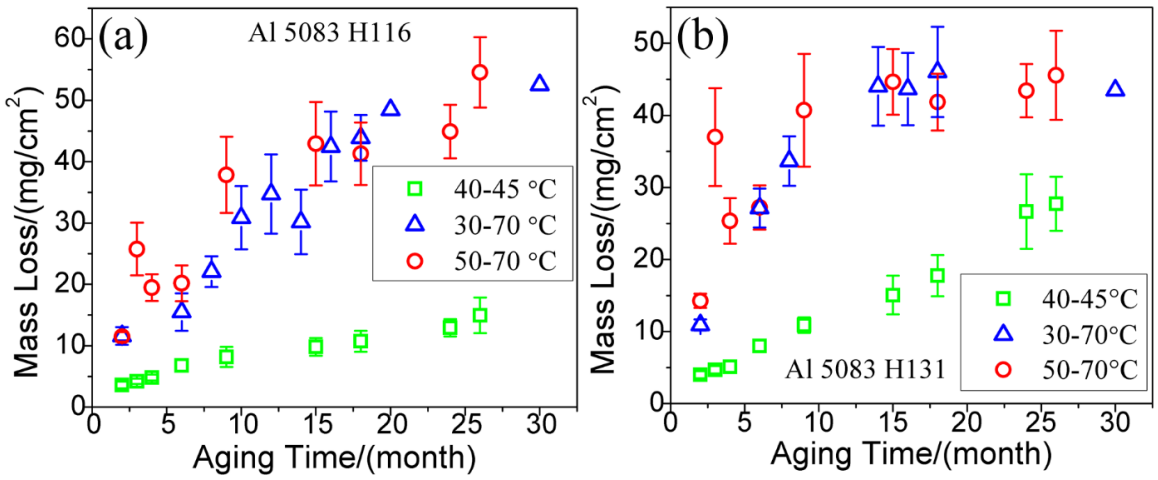

Figure 6.4 Mass loss of Al 5083 H116 aged at cyclic temperatures (40-45, 30-70, and 50-70℃) for different times.

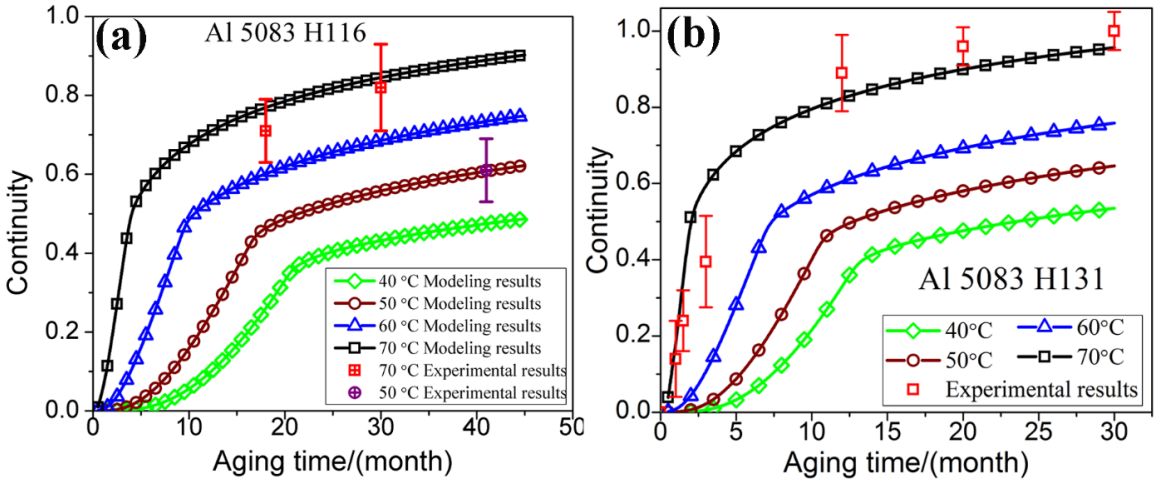

Figure 6.5 Experimental and modeling continuity results for (a) Al 5083 H116 and (b) Al 5083 H131 aged at constant temperatures (40, 50, 60, and 70°C) for different times.

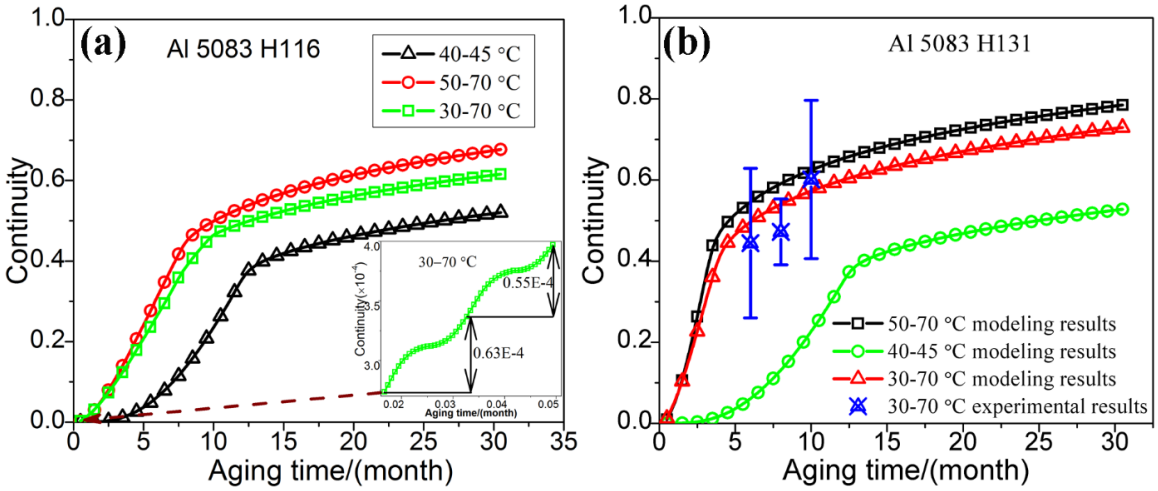

Figure 6.6 Experimental and modeling continuity results of Al 5083 H116 aged at different cyclic temperatures (40-45, 30-70, and 50-70℃) for different times.

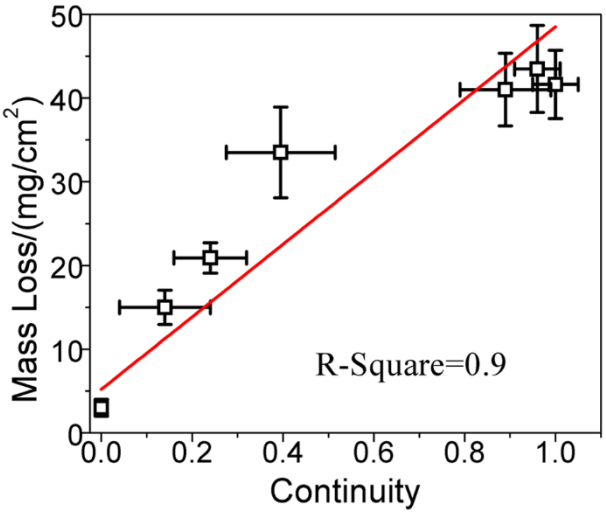

Figure 6.7 Experimental continuity results versus ASTM G-67 mass loss of Al 5083 H131 aged at 70 °C for different times.

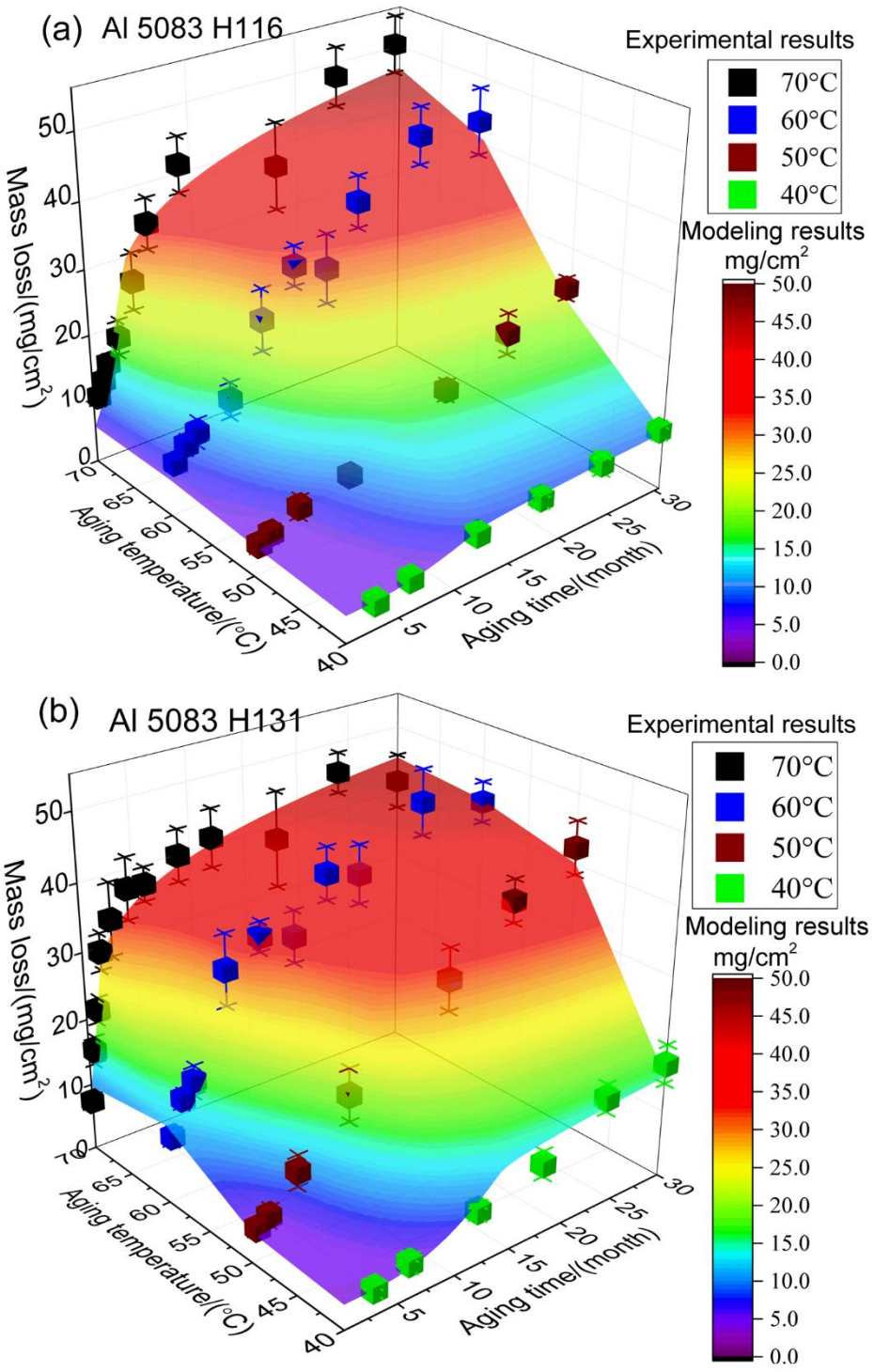

Figure 6.8 Experimental and modeling mass loss of (a) Al 5083 H116 and (b) Al 5083 H131 aged at constant temperatures (40, 50, 60, and 70°C) for different times.

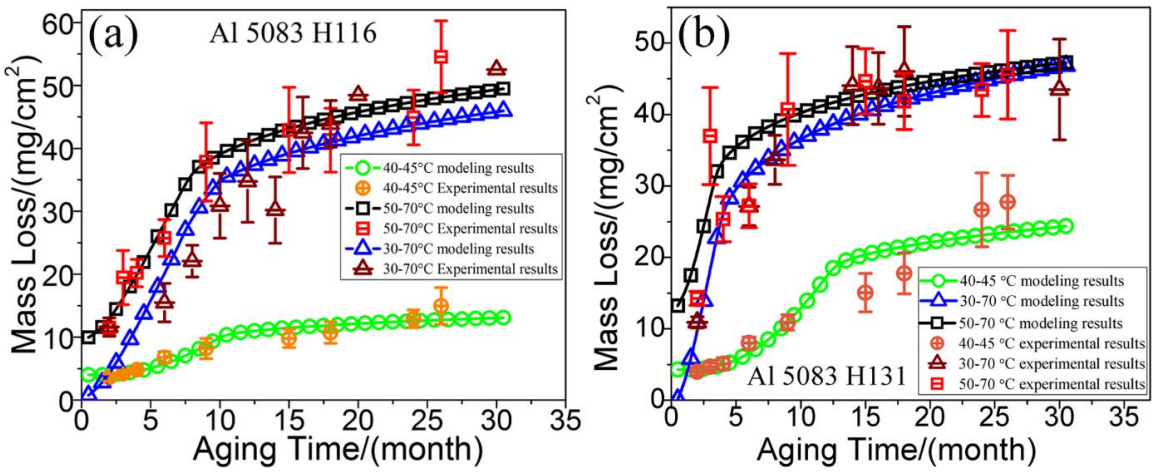

Figure 6.9 Experimental and modeling mass loss of (a) Al 5083 H1116 and (b) H131 aged at cyclic temperature (40-45, 30-70, and 50-70℃) for different times.

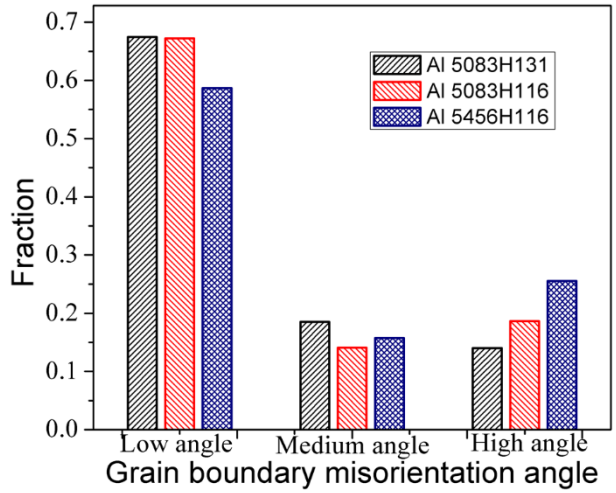

Figure 6.10 Grain boundary misorientation angle distribution of Al 5083 H116, H131 and Al 5456 H116.

CHAPTER 7

CONCLUSIONS

In this work, Al 5xxx alloys were aged at different temperatures for different times, and their microstructures were characterized by different techniques, such as SEM, EBSD, STEM, EDS, APT, and SANS. In addition, both an intragranular and intergranular precipitation model were developed to predict the nucleation density and size of Mg-rich precipitates. Moreover, ASTM G67 mass loss tests were conducted to evaluate the sensitized degrees for Al 5xxx alloys of different aging states. A summary of accomplishments and conclusions drawn from this work are described below:

1. EBSD results show that Al 5083 H131 has smaller grain size and higher GND density than that of Al 5083 H116. STEM and SANS results reveal that both size and concentration of Mg-rich precipitates formed in Al 5083 H131 and H116 aged at 70℃ increase with aging time, while the precipitate number density decreases with time. Mg concentration of precipitate increases with aging time, indicating a phase transformation from GP zones to β'/β phases occurs in Al 5083 aged at 70℃. APT results of Al 5083 H116 aged at 50℃ for 24 months demonstrate that ellipsoid GP zones and laminar β" phases have formed in the matrix and at the matrix-pre-existing particle interface, respectively.

2. Al 5083 alloy of temper H131 has more and larger precipitates than Al 5083 H116 when aged at 70℃ for the same time, and the phase transformation from GP zones to β phase in H131 is faster than that in Al 5083 H116, which is explained by the higher dislocation density in Al 5083 H131.
3. A higher aging temperature leads to more and larger precipitates, and much faster phase transformation in Al 5083 H116.
4. Mg-rich precipitates are found to form heterogeneously on pre-existing particles and grain boundaries in Al 5456 H116 sample aged at 70℃ for 1.5, 9, 18, and 30 months. Mg-rich precipitates are found on pre-existing particles of Al 5456 H116 samples aged for 1.5, 9, and 18 months. GP zones, β'' and β' phases are observed to form within the matrix of Al 5456 H116 aged at 70℃ for 30 months. The average radius of Mg-rich precipitates is 18.5 nm, and their total volume fraction is 1.39% for Al 5456 aged at 70℃ for 30 months. β' phase is found to form at the grain boundaries of the navy ship sample, and no intragranular Mg-rich precipitates are observed using STEM. Continuity results of intergranular precipitates combined with ASTM G-67 mass loss data reveal that continuity is more critical to IGC of Al 5456 H116 alloy than thickness of intergranular precipitates.
5. The overall nucleation, growth, and coarsening of Mg-rich precipitates predicted by the model agree well with experimental results. In addition, the dissolution of metastable phases (GP zones and β'' phases) was also observed in the modeling results. The PSD results of different precipitates were able to reveal the phase transformation stages of different aging states.

6. A collector plate-based nucleation, growth, and coarsening model was developed to predict the evolution of thickness and continuity of intergranular precipitates. In this model, an equivalent average Mg concentration at the grain boundary was derived, and three modified coarsening mechanisms, the classical LSW and Kirchner's coarsening mechanism and a mechanism combining these two mechanisms, were adopted. The modeling results match generally well with experimental results extracted from STEM images of Al 5083 H131 alloys aged 70℃ for different times. In addition, the Kirchner mechanism model will break down when the value of R_c/R is close to 1. Both the coarsening fraction value (about 10%) and the precipitate size distribution obtained from the new model indicate that coarsening is not dominant at the grain boundary even though the aging time is as long as 40 months at 70℃. Moreover, the model was also applied to a high temperature (180℃), and the modeling results agree well with previous results. Coarsening of intergranular precipitates was observed at high temperature.
7. For Al 5083 H116, H131 and Al 5456 H116, ASTM G-67 mass loss will increase with aging time as well as aging temperature until they become fully sensitized. 5083 H116 is found to be more corrosion resistant than Al 5083 H131 for both the isothermal and the nonisothermal aging experiments.
8. For Al 5050 H32, 5052 H32, and 5154 H32 alloy, ASTM G-67 mass loss levels increase very slowly when aged at 50 and 60℃. However, a more rapid sensitization trend was observed for these three alloys when aged at 70℃.
9. Mass loss of Al 5050 H32, 5052 H32, 5154 H32 and Al 5083 H32 indicated that Mg concentration plays a critical role in the sensitization of Al 5xxx alloys. In

addition, for Al 5083 H131 and H116, DoS could be affected by grain size and fraction of HAGB.

10. A collector plate mechanism-based β phase nucleation, growth and coarsening model was used to predict the continuity of intergranular β phase, and the mass loss was assumed to be linearly related to continuity. The modeling results fit well with the experimental results for both the isothermal and nonisothermal cases.

APPENDIX

A.l STEM EDS results for Al 5456 H116

Fig. A.1 is the EDS line scan results of precipitates formed at the interface of the pre-existing particle and matrix, as shown in Fig. 4.12 (a). Fig. A.2 is the EDS maps of elements Al, Mg, and Si for precipitate in Fig. 4.14(b). Fig. A.3 is the EDS line scan results for precipitates in Fig. 4.15 (a), and these precipitates are highlighted by number "1", "2", "3", "4", and "5".

A.2 Calculation of chemical potential for Mg-rich precipitates

The matrix of Al 5083 alloys (simplified as Al-Mg binary system) is treated as substitutional solution, [147] and the Gibbs free energy is expressed as

$$G_m = X_{Al}\,{}^0G_{Al}^{fcc} + X_{Mg}\,{}^0G_{Mg}^{fcc} + R_C T\left(X_{Al}\ln X_{Al} + X_{Mg}\ln X_{Mg}\right) + X_{Al}X_{Mg}\sum_{i=0}^{2} L_i (X_{Al} - X_{Mg})^i \qquad \text{(A.1)}$$

where ${}^0G_{Al}^{fcc}$ and ${}^0G_{Mg}^{fcc}$ stand for the molar Gibbs free energy of pure Al and Mg, [187] R_C is the gas constant, and L_i is the ith binary interaction parameter (see Table A1).

β" phase (Al_3Mg) is reported to have a $L1_2$-type structure, and its molar Gibbs energy can be calculated using the following equation: [188]

$$G_{Al_3Mg} = G^{dis}_{Al_3Mg}(X_{Mg}) + G^{ord}_{Al_3Mg}(Y^s_{Mg}) \quad \text{(A.2)}$$

where $G^{dis}_{Al_3Mg}(X_{Mg})$ and $G^{ord}_{Al_3Mg}(Y^s_{Mg})$ represent the molar Gibbs free energy of the disordered and the ordered state. $G^{dis}_{Al_3Mg}(X_{Mg})$ can be obtained using Eq. (A.1), and $G^{ord}_{Al_3Mg}(Y^s_{Mg})$ is defined as

$$G^{ord}_{Al_3Mg}(Y^s_{Mg}) = G^{4ssl}_{Al_3Mg}(Y^s_{Mg}) - G^{4ssl}_{Al_3Mg}(Y^s_{Mg} = X_{Mg}) \quad \text{(A.3)}$$

where $G^{4ssl}_{Al_3Mg}(Y^s_{Mg})$ is the Gibbs free energy for one of the sublatttice structures (Al_3Mg, Al_2Mg_2, $AlMg_3$), and Y^s_{Mg} is calculated from the sublattice fraction of Mg. $G^{4ssl}_{Al_3Mg}(Y^s_{Mg} = X_{Mg})$ is calculated based on the average fraction of Mg in Al_3Mg, which is 0.25.

β' and β phases are stoichiometric compounds, and their Gibbs free energies [149] are given as

$$G_{stoi} = a_i {}^0G^{fcc}_{Al} + b_i {}^0G^{hcp}_{Mg} + A_i + B_iT \quad \text{(A.4)}$$

where a_i and b_i are the number of Al and Mg atom in the stoichiometric compounds, A_i and B_i are the formation enthalpy and entropy of the compound.

The Gibbs free energy of GP zone is calculated based on Eqs. (A.1) and (A.2)

$$G_{GPzone} = (1 - f_{Al_3Mg})G^{dis}(X_{Mg,G}) + f_{Al_3Mg}G_{Al_3Mg} \quad \text{(A.5)}$$

where f_{Al_3Mg} is the fraction of Al_3Mg in GP zone, and $X_{Mg,G}$ can be calculated based on the mass balance of Mg within GP zones.

A.3 Modified Kirchner's coarsening mechanism

In order to obtain the growth behavior of precipitates at grain boundaries, Kirchner [67] adopted the growth mechanism derived by Speight, [69] and followed Wagner's [68] method to couple solve the continuity, solute mass balance, and precipitates growth equation. In the paper, the continuity equation is given as

$$\frac{\partial f}{\partial t} = -\frac{\partial(f\dot{R})}{\partial R} \quad \text{(A.6)}$$

where f is the precipitate distribution function, $\dot{R}$ is equal to dR/dt, and the total number of precipitates is

$$N_{tot} = \int_0^\infty f(R,t)dR \quad \text{(A.7)}$$

During the coarsening stage, the number change of precipitates is mainly caused by the disappearing of precipitates of radius approach zero, which can be written as

$$-\frac{dN}{dt} = -\frac{d}{dt}\int_0^\infty f(R,t)dR = -\lim_{R\to 0}\left(f\dot{R}\right) \tag{A.8}$$

The total volume of the precipitates can be calculated as

$$V_{tot} = \int_0^\infty f_{PV} R^3 f(R,t)dR \tag{A.9}$$

The modified growth mechanism of Speight is [69]

$$\frac{dR}{dt} = \frac{2\pi}{9}\frac{D_b \delta_{eff} \nu_{at}^P C_{\alpha\beta}}{\left(f_{PV}^2 / f_{PA}\right)\ln\left(R_c/R\right)kTR^2}\left[\left(\frac{\overline{1}}{R}\right) - \frac{1}{R}\right] \tag{A.10}$$

where $\overline{\frac{1}{R}}$ is the average value of $\frac{1}{R}$. Differentiate Eq. (A.11), the critical radius, R^*, of precipitates (the radius at which precipitates neither grow nor dissolve) is obtained as

$$R^* = 1\Big/\left(\frac{\overline{1}}{R}\right) = \int_0^\infty f(R,t)dR \Big/ \int_0^\infty \left(f(R,t)/R\right)dR \tag{A.11}$$

An unitless variable, ρ, is defined to stand for the radius of precipitates

$$\rho = R/R^*(t) \tag{A.12}$$

The distribution function $f(R,t)$ is rewritten as a product of a time-dependent function, $g_B(t)$, a time-independent function, $h_B(t)$, and ρ^3

$$f(R,t) = g_B(t)\rho^3 h_B(\rho) \tag{A.13}$$

and

$$h_B(\rho = 0) = 1 \tag{A.14}$$

Using Eqs.(A.9),(A.12), and (A.13), g_B is expressed as

$$g_B(t) = \frac{V_{tot}}{f_{PV}\left[R^*(t)\right]^4 \int_0^\infty h_B(\rho)\rho^6 d\rho} \tag{A.15}$$

Submit Eqs.(A.10), (A.12), and (A.13) into the right side of Eq. (A.8) yields

$$\begin{aligned} -\lim_{R\to 0}\left(f\dot{R}\right) &= -\lim_{R\to 0}\left[h_B(\rho) g_B(t) \frac{2\pi}{9} \frac{D_b \delta_{eff} \gamma \nu_{at}^P C_{\alpha\beta}}{\left(f_{PV}^2 / f_{PA}\right)\ln\left(R_c/R\right)kTR^2} \frac{R^3}{R^{*3}}\left(\frac{1}{R^*} - \frac{1}{R}\right)\right] \\ &= g_B(t)\frac{2\pi}{9}\frac{D_b \delta_{eff} \gamma \nu_{at}^P C_{\alpha\beta}}{\left(f_{PV}^2 / f_{PA}\right)\ln\left(R_c/R\right)kT}\frac{1}{R^{*3}} \end{aligned} \tag{A.16}$$

And insertion of Eqs.(A.12), (A.13), and (A.15) into the left side of Eq.(A.8) gives

$$-\frac{d}{dt}\int_0^\infty f(R,t)dR = -\frac{d}{dt}\int_0^\infty g_B(t)\rho^3 h_B(\rho)dR$$
$$= 3\frac{V_{tot}}{f_{PV}\left[R^*(t)\right]^4\int_0^\infty h_B(\rho)\rho^6 d\rho}\left[\int_0^\infty \rho^3 h_B(\rho)d\rho\right]\frac{dR^*}{dt} \quad \text{(A.17)}$$

The final growth rate of critical radius is obtained as

$$\frac{dR^*}{dt} = \frac{2\pi}{27}\frac{D_b\delta_{eff}\gamma\nu_{at}^P C_{\alpha\beta}}{\left(f_{PV}^2/f_{PA}\right)\ln\left(R_c/R\right)\gamma_B kT}\frac{1}{R^{*3}} \quad \text{(A.18)}$$

where

$$\gamma_B = \int_0^\infty \rho^3 h_B(\rho)d\rho \quad \text{(A.19)}$$

Assume the distribution function $f(R,t)$ is valid from the very beginning (t=0), integration of Eq. (A.18) leads to

$$R^*(t) = R^*(t=0)\left[1+t/\tau_B^1\right]^{1/4} \quad \text{(A.20)}$$

With

$$\tau_B^1 = \frac{27\left(f_{PV}^2 / f_{PA}\right)}{8\pi} \frac{\ln\left(R_c / R\right)\gamma_B kT\left[R^*(t)\right]^4}{D_b \delta_{eff} \gamma v_{at}^P C_{\alpha\beta}} \tag{A.21}$$

If we write

$$A' = \frac{3}{\pi}\left(f_{PV}^2 / f_{PA}\right) \tag{A.22}$$

and

$$B = \ln\left(R_c / R\right) \tag{A.23}$$

Eqs. (A.18) and (A.20) will become the same form as the Eqs. (A.19) and (A.21) in Kirchner's paper, [67] therefore the solution of these equations will be the same, which will not be discussed here. And the ultimate precipitate growth rate is given as

$$\frac{dR}{dt} = \frac{9 D_b \delta_{eff} \gamma v_{at}^P C_{\alpha\beta}}{128 A' B k T} \frac{1}{R^3} \tag{A.24}$$

Multiply both sides of Eq. (A.24) by ($f_{PV}R^2$), the volume growth rate of precipitate can be given as

$$\left.\frac{dV}{dt}\right|_{Kc} = \frac{27 f_{PV} C_{\alpha\beta} \delta_{eff} \gamma v_{at}^{P}}{128\left(C_{\beta} - C_{\alpha\beta}\right) A' \ln\left(R_c / R\right) kT} \frac{D_b}{R} \tag{A.25}$$

A.4 Modified Lifshitz-Slyosov-Wagner (LSW) coarsening mechanism

If grain boundaries are almost fully covered by intergranular precipitates, the coarsening behavior of these precipitates can be described using the modified classical LSW theory as follow: [72]

$$\frac{dR}{dt} = \frac{f_{PA}}{3 f_{PV}} \frac{D_b}{R} \left(\Delta - \frac{\alpha}{R} \right) \tag{A.26}$$

where $\Delta = \overline{C}_{R_x} - C_{eq}$, and $\alpha = \left(2 f_{PA} \gamma / 3 f_{PV} kT\right) v_{at}^{P} C_{eq}$

The dimensionless format of Eq. (A.26) is

$$\frac{d\rho_c^3}{dt'} = \frac{f_{PA}}{f_{PV}} \left(\frac{\rho}{x} - 1 \right) \tag{A.27}$$

where $\rho_c = R / R_{cr0}$, $t' = t / T_c$, $R_{cr0} = \alpha / \Delta_0$, $T_c = R_{cr0}^3 / \alpha D_b$ and $x = \Delta_0 / \Delta$. Δ_0 is the initial supersaturation. The continuity equation is

$$\frac{\partial f(\rho_c^3, t)}{\partial t} + \frac{\partial \left[f(\rho_c^3, t) v_p \right]}{\partial \rho_c^3} = 0 \tag{A.28}$$

where $f(\rho_c^3,t)$ is the volume distribution function of intergranular precipitates within a factor of f_{PV}, and $v_p = d\rho_c^3/dt$ is the precipitate growth rate. Based on the solute mass balance, we can obtain

$$Q_0 = \Delta_0 + q_0 = \Delta + q \tag{A.29}$$

where Q_0 is the total supersaturation, and q_0 is the volume of the solute initially in the precipitate. And the volume of solute, q, in precipitates at certain time, t, is obtained as

$$q = f_{PV} R_{cr0}^3 \int_0^\infty f(\rho_c^3,t)\rho_c^3 d\rho_c^3 \tag{A.30}$$

Insert Eq.(A.30) into Eq. (A.29), and after some algebra, we can obtain

$$1 = \frac{\Delta_0}{Q_0}\frac{1}{x} + \kappa\int_0^\infty f\left(\rho_c^3,t\right)\rho_c^3 d\rho_c^3 \tag{A.31}$$

where $\kappa = \dfrac{f_{PV} R_{cr0}^3}{Q_0}$

The canonical form of Eqs. (A27), (A28), and (A.31) are given respectively as

$$\left.\begin{aligned} \frac{dz'}{d\tau} &= v(z',\tau) = \left(z'^{1/3} - 1\right)\mu(\tau) - z' \\ \mu(\tau) &= 3 f_{LS} \frac{dt}{dx^3} \end{aligned}\right\} \tag{A.32}$$

$$\frac{\partial \phi}{\partial \tau} + \frac{\partial}{\partial z'} \phi v(z', \mu) = 0 \tag{A.33}$$

$$\left.\begin{aligned} 1 &= \frac{\Delta_0}{Q_0} e^{-\tau/3} + \kappa e^{\tau} \int_0^{\infty} \phi(z',\tau) z' dz' \\ \phi\big|_{t=\tau=0} &= f_0(z'), z'\big|_{\tau=0} = \rho_c^3 \end{aligned}\right\} \tag{A.34}$$

where $z' = \rho_c^3 / x^3(t)$, $\tau = \ln x^3(t)$, $\phi(z',t)dz' = f(\rho_c^3, t)d\rho_c^3$. The asymptotic solution of the above equations are very similar to the classical LSW model, which can be found in Ref. [72]. Finally, the number of precipitates per unit volume is shown as

$$n(t) = \frac{Q_0}{f_{PV}(1.11)} \overline{R}^{-3} = \frac{Q_0}{f_{PV}(1.11)} \frac{f_{PV}}{f_{PA}} \frac{9}{4\alpha D_b} t^{-1} \tag{A.35}$$

where $\overline{R}$ is the average radius of precipitates. Therefore

$$\overline{R}^3 = \frac{4}{9} \frac{f_{PA}}{f_{PV}} \alpha D_b t \tag{A.36}$$

Table A.1 Thermodynamic parameters for Al-Mg binary system.

Phase	Thermodynamic value
Matrix [149]	$L_0 = 1593 + 2.149T$, $L_1 = 1014 - 0.66T$, $L_2 = -673$
Al_3Mg [150]	$\mu_{AlMg} = -500 + 0.45185T$, $G^{4ssl}_{Al2Mg2} = 4\mu_{AlMg}$,
	$G^{4ssl}_{Al_3Mg} = 3\mu_{AlMg} + \Delta G_{Al_3Mg}$,
	$G^{4ssl}_{AlMg_3} = 3\mu_{AlMg} + \Delta G_{AlMg_3}$, $\Delta G_{Al_3Mg} = \Delta G_{AlMg_3} = 0$,
	$L^{dis}_0 = G^{4ssl}_{Al_3Mg} + 1.5G^{4ssl}_{Al_2Mg_2} + G^{4ssl}_{AlMg_3} + 1.5L^{4ssl}_{rec} + 4L^{4ssl}_0$
	$L^{dis}_1 = 2G^{4ssl}_{Al_3Mg} - 4G^{4ssl}_{AlMg_3} + 4L^{4ssl}_1$,
	$L^{dis}_2 = G^{4ssl}_{Al_3Mg} - 1.5G^{4ssl}_{Al_2Mg_2} + G^{4ssl}_{AlMg_3} - 1.5L^{4ssl}_{rec} + 4L^{4ssl}_2$
	$L^{4ssl}_0 = 3305.25 - 2.4T$, $L^{4ssl}_1 = 56.25 - 0.025T$, $L^{4ssl}_2 = -325 + 0.17T$,
	$L^{4ssl}_{rec} = \mu_{AlMg}$
β' [20]	$\Delta H_{\beta' \to \beta} = -1.3J/g$
β [149]	${}^0G_{\beta - Al_{140}Mg_{89}} = 140\,{}^0G^{fcc}_{Al} + 89\,{}^0G^{hcp}_{Mg} - 803385 + 105.238T$

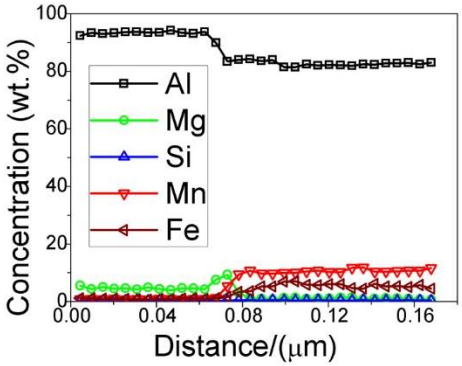

Figure A.1 EDS line scan results across the interface as indicated by the dark arrow in Fig. 4.12 (a).

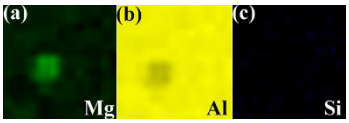

Figure A.2 EDS mapping results of the precipitate in Fig. 4.14(b).

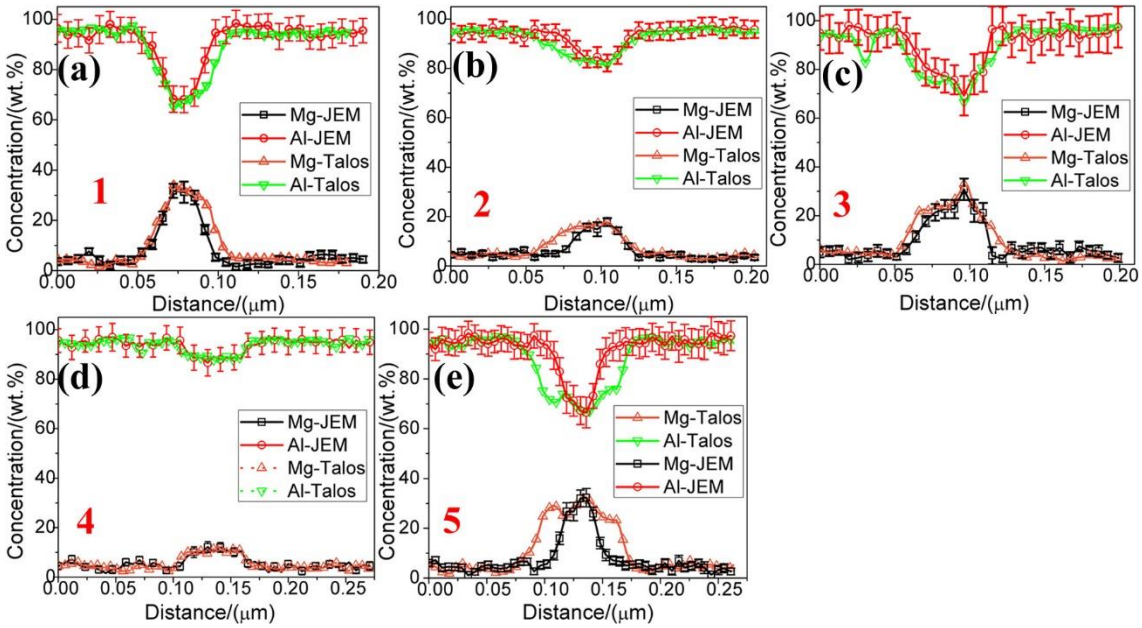

Figure A.3 EDS line scan results of intragranular precipitates in Fig. 4.15. (a) and (d) (identified by number (a)1, (b)2, (c)3, (d)4, and (e)5) obtained from JEM 2800 ultrafast EDS system and FEI Talos F200X STEM.

REFERENCES

[1] Robert A. Sielski: *Ships Offshore Struct.*, 2008, vol. 3, pp. 57–65.

[2] E.S.C Jonathan and S Montgomery: *Amcptiac Q*, 2004, vol. 8, p. 4.

[3] W.S Miller, L Zhuang, J Bottema, a.J Wittebrood, P De Smet, a Haszler, and a Vieregge: *Mater. Sci. Eng. A*, 2000, vol. 280, pp. 37–49.

[4] C. Hsu, K. A Q O'Reilly, B. Cantor, and R. Hamerton: *Mater. Sci. Eng. A*, 2001, vol. 304–306, pp. 119–24.

[5] Y. Chen, M. Weyland, and C. R. Hutchinson: *Acta Mater.*, 2013, vol. 61, pp. 5877–94.

[6] R. P. Garrett, J. Lin, and T. A. Dean: *Int. J. Plast.*, 2005, vol. 21, pp. 1640–57.

[7] Mala M. Sharma: *Mater. Charact.*, 2008, vol. 59, pp. 91–99.

[8] J L Searles, P I Gouma, and R G Buchheit: *Metall. Mater. Trans. A*, 2001, vol. 32, pp. 2859–67.

[9] R H Jones, D R Baer, M J Danielson, and J S Vetrano: *Metall. Mater. Trans. a-Physical Metall. Mater. Sci.*, 2001, vol. 32, pp. 1699–1711.

[10] R H Jones, J S Vetrano, and C F Windisch Jr.: *Corrosion*, 2004, vol. 60, pp. 1144–54.

[11] E H DIX, W A ANDERSON, and M BYRON SHUMAKER: *Corrosion*, 1959, vol. 15, pp. 19–26.

[12] Andreas Afseth, Geoff M Scamans, Rajan Ambat, Alison J Davenport, Martin Strangwood, Yudie Yuan, and Brian J Connolly: in *Alum. Alloy. 2006 - ICAA10*, Trans Tech Publications, 2006, pp. 641–46.

[13] N. Birbilis and R. G. Buchheit: *J. Electrochem. Soc.*, 2005, vol. 152, pp. B140–51.

[14] J.L. Searles, Pelagia Irene Gouma, and R.G. Buchheit: *Mater. Sci. Forum*, 2002, vol. 396–402, pp. 1437–42.

[15] Ramasis Goswami and Ronald L. Holtz: *Metall. Mater. Trans. A Phys. Metall.*

Mater. Sci., 2013, vol. 44, pp. 1279–89.

[16] Tatsuo Sato and Akihiko Kamio: *Mater. Sci. Eng. A*, 1991, vol. 146, pp. 161–80.

[17] S Kar: *Measuring and Modeling of Thermal Exposure Corrosion Damage Susceptibility of AA5083 Alloy*, Department of Metallurgical Engineering, University of Utah, 2012.

[18] Christian. Vargel: *Corrosion of Aluminium*, Elsevier, 2004.

[19] J R Davis, J R D Associates, and A.S.M.I.H. Committee: *Aluminum and Aluminum Alloys*, ASM International, 1993.

[20] JG Kaufman: *Introduction to Aluminum Alloys and Tempers*, 2000.

[21] Nikolay A. Belov, Dmitry G. Eskin, and Andrey A. Aksenov: *Multicomponent Phase Diagrams*, 2005, pp. 341–77.

[22] Y. Zuo and Y.A. Chang: *Calphad*, 1993, vol. 17, pp. 161–74.

[23] Yakun Zhu, David A. Cullen, Soumya Kar, Michael L. Free, and Lawrence F. Allard: *Metall. Mater. Trans. A Phys. Metall. Mater. Sci.*, 2012, vol. 43, pp. 4933–39.

[24] S Samson: *Acta Crystallogr.*, 1965, vol. 19, pp. 401–13.

[25] Andre. Guinier and Gerard Fournet: *Small-Angle Scattering of X-Rays*, Wiley, New York, 1955.

[26] M. Roth, J. M. Raynal, and IUCr: *J. Appl. Crystallogr.*, 1974, vol. 7, pp. 219–21.

[27] J. M. Raynal, M. Roth, and IUCr: *J. Appl. Crystallogr.*, 1975, vol. 8, pp. 535–37.

[28] C. Gault, A. Dauger, and P. Boch: *Acta Metall.*, 1980, vol. 28, pp. 51–60.

[29] R; Nozato and S; Ishihara: *Trans. Japan Inst. Met.*, 1980, vol. 21, pp. 580–88.

[30] Y Kojima, T Takahashi, M Kubo, and T Morinaga: *Metall. Trans. A*, 1981, vol. 12, pp. 1113–17.

[31] T. Sato, Y. Kojima, and T. Takahashi: *Metall. Trans. A*, 1982, vol. 13, pp. 1373–78.

[32] Kozo Osamura and Tetsuzo Ogura: *Metall. Trans. A*, 1984, vol. 15, pp. 835–42.

[33] Masahiro Kubota: *Mater. Trans.*, 2005, vol. 46, pp. 241–50.

[34] M. J. Starink and A. -M. Zahra: *Acta Mater.*, 1998, vol. 46, pp. 3381–97.

[35] Michael Feuerbacher, Carsten Thomas, and Et Al.: *Zeitschrift Fur Krist.*, 2007, vol. 222, pp. 259–88.

[36] R Goswami, G Spanos, P S Pao, and R L Holtz: *Mater. Sci. Eng. A*, 2010, vol. 527, pp. 1089–95.

[37] D. Scotto D'Antuono, J. Gaies, W. Golumbfskie, and M. L. Taheri: *Scr. Mater.*, 2014, vol. 76, pp. 81–84.

[38] Yifu Zhao, Mikhail N. Polyakov, Matthew Mecklenburg, Michael E. Kassner, and Andrea M. Hodge: *Scr. Mater.*, 2014, vol. 89, pp. 49–52.

[39] Jianfeng Yan, Nathan M. Heckman, Leonardo Velasco, and Andrea M. Hodge: *Sci. Rep.*, 2016, vol. 6, p. 26870.

[40] M. C. Carroll, P. I. Gouma, M. J. Mills, G. S. Daehn, and B. R. Dunbar: *Scr. Mater.*, 2000, vol. 42, pp. 335–40.

[41] Chunyan Meng, Di Zhang, Hua Cui, Linzhong Zhuang, and Jishan Zhang: *J. Alloys Compd.*, 2014, vol. 617, pp. 925–32.

[42] Shi'ang Zhou, Zhen Zhang, Ming Li, Dejiang Pan, Hailin Su, Xiaodong Du, Ping Li, and Yucheng Wu: *Mater. Des.*, 2016, vol. 90, pp. 1077–84.

[43] E. A. Marquis and D. N. Seidman: *Acta Mater.*, 2005, vol. 53, pp. 4259–68.

[44] Ana Alil, Miljana Popović, Tamara Radetić, Milorad Zrilić, and Endre Romhanji: *J. Alloys Compd.*, 2015, vol. 625, pp. 76–84.

[45] P Ratchev, B Verlinden, P De Smet, and P van Houtte: *Acta Mater.*, 1998, vol. 46, pp. 3523–33.

[46] John E. Hilliard: in *Am. Soc. Met.*, H.I. Aaronson, ed., American Society of Metal, 1970, p. 497.

[47] Kim N. Tran and Lourdes Salamanca-Riba: *Adv. Eng. Mater.*, 2013, vol. 15, pp. 1105–10.

[48] R. Zhang, R. K. Gupta, C. H J Davies, A. M. Hodge, M. Tort, K. Xia, and N. Birbilis: *Corrosion*, 2016, vol. 72, pp. 160–68.

[49] Clarence Zener: *J. Appl. Phys.*, 1949, vol. 20.

[50] H B Aaron and H I Aaronson: *Acta Metall.*, 1968, vol. 16, pp. 789–98.

[51] Math Hillert: *Jernkontorets Ann.*, 1957, vol. 141, pp. 757–89.

[52] J C Fisher: *J. Appl. Phys.*, 1951, vol. 22.

[53] Paul G Shewmon: *J. Appl. Phys.*, 1963, vol. 34.

[54] W W Mullins: *J. Appl. Phys.*, 1957, vol. 28.

[55] F A Nichols and W W Mullins: *J. Appl. Phys.*, 1965, vol. 36.

[56] A D Brailsford and H B Aaron: *J. Appl. Phys.*, 1969, vol. 40.

[57] R G Faulkner and J Caisley: *Met. Sci.*, 1977, vol. 11, pp. 200–207.

[58] R A Carolan and R G Faulkner: *Acta Metall.*, 1988, vol. 36, pp. 257–66.

[59] R G Faulkner and H Jiang: *Mater. Sci. Technol.*, 1993, vol. 9, pp. 665–71.

[60] H Jiang and R G Faulkner: *Acta Mater.*, 1996, vol. 44, pp. 1857–64.

[61] H Jiang and R G Faulkner: *Acta Mater.*, 1996, vol. 44, pp. 1865–71.

[62] Marc de Haas, S.M. van Scherpenzeel, and Jeff Th.M. de Hosson: *Mater. Sci. Forum*, 2006, vol. 519–521, pp. 467–72.

[63] J B Zeldovich: *ACTA Physicochim. URSS*, 1943, vol. 18, pp. 1–22.

[64] K C Russell: *Acta Metall.*, 1968, vol. 16, pp. 761–69.

[65] K C Russell: *Acta Metall.*, 1969, vol. 17, pp. 1123–31.

[66] V V Slyozov: *Fiz. Tverd. Tela*, 1967, vol. 9, pp. 1187–91.

[67] H O K Kirchner: *Metall. Trans.*, 1971, vol. 2, pp. 2861–64.

[68] C Wagner: *Elektrochem*, 1961, vol. 65, p. 581.

[69] M V Speight: *Acta Metall.*, 1968, vol. 16, pp. 133–35.

[70] A J Ardell: *Acta Metall.*, 1972, vol. 20, pp. 601–9.

[71] P P Bansal and A J Ardell: *Metallography*, 1972, vol. 5, pp. 97–111.

[72] I.M. Lifshitz and V.V. Slyozov: *J. Phys. Chem. Solids*, 1961, vol. 19, pp. 35–50.

[73] J J Hoyt: *Acta Metall. Mater.*, 1991, vol. 39, pp. 2091–98.

[74] J A Marqusee and John Ross: *J. Chem. Phys.*, 1983, vol. 79.

[75] Yongfeng Zhang, Paul C Millett, Michael Tonks, Liangzhe Zhang, and Bulent Biner: *J. Phys. Condens. Matter*, 2012, vol. 24, p. 305005.

[76] L Yang, F Gao, R J Kurtz, and X T Zu: *Acta Mater.*, 2015, vol. 82, pp. 275–86.

[77] Y Gao, N Zhou, D Wang, and Y Wang: *Acta Mater.*, 2014, vol. 68, pp. 93–105.

[78] Yuhki Tsukada, Yuki Beniya, and Toshiyuki Koyama: *J. Alloys Compd.*, 2014,

vol. 603, pp. 65–74.

[79] Mattias Slabanja and Göran Wahnström: *Acta Mater.*, 2005, vol. 53, pp. 3721–28.

[80] Zugang Mao, Chantal K Sudbrack, Kevin E Yoon, Georges Martin, and David N Seidman: *Nat Mater*, 2007, vol. 6, pp. 210–16.

[81] Lynda Amirouche and Mathis Plapp: *Acta Mater.*, 2009, vol. 57, pp. 237–47.

[82] E Clouet, C Hin, D Gendt, M Nastar, and F Soisson: *Adv. Eng. Mater.*, 2006, vol. 8, pp. 1210–14.

[83] Frédéric Soisson: *J. Nucl. Mater.*, 2006, vol. 349, pp. 235–50.

[84] D A Porter and K E Easterling: *Phase Transformations in Metals and Alloys Third Edition*, 2014.

[85] M. Perez, M. Dumont, and D. Acevedo-Reyes: *Acta Mater.*, 2008, vol. 56, pp. 2119–32.

[86] M Volmer and A Weber: *Z. Phys. Chem*, 1926, vol. 119, pp. 277–301.

[87] R Becker and W Döring: *Ann. Phys.*, 1935, vol. 416, pp. 719–52.

[88] R. Kampmann and R. Wagner: in *Decompos. Alloy. Early Stages*, 1984, pp. 91–103.

[89] J W Gibbs, H A Bumstead, R G Van Name, and W R Longley: *The Collected Works of J. Willard Gibbs*, Longmans, Green and Co., 1902.

[90] James Thomson: *Trans. R. Soc. Edinburgh*, 2013, vol. 16, pp. 575–80.

[91] James Thomson: *Proc. R. Soc. London*, 1860, vol. 11, pp. 472–81.

[92] Carl Wagner: *Berichte Der Bunsengesellschaft Für Phys. Chemie*, 1961, vol. 65, pp. 581–91.

[93] S P Ringer and K Hono: *Mater. Charact.*, 2000, vol. 44, pp. 101–31.

[94] A. Deschamps and Y. Brechet: *Acta Mater.*, 1998, vol. 47, pp. 293–305.

[95] D. Bardel, M. Perez, D. Nelias, S. Dancette, P. Chaudet, and V. Massardier: *Acta Mater.*, 2015, vol. 83, pp. 256–68.

[96] O. R. Myhr and Ø Grong: *Acta Mater.*, 2000, vol. 48, pp. 1605–15.

[97] J. Svoboda, F. D. Fischer, P. Fratzl, and Ernst Kozeschnik: *Mater. Sci. Eng. A*, 2004, vol. 385, pp. 166–74.

[98] L. Onsager: *Phys. Rev.*, 1931, vol. 37, pp. 237–41.

[99] Peter Lang, Tomasz Wojcik, Erwin Povoden-Karadeniz, Ahmad Falahati, and Ernst Kozeschnik: *J. Alloys Compd.*, 2014, vol. 609, pp. 129–36.

[100] G. Stechauner and E. Kozeschnik: *Acta Mater.*, 2015, vol. 100, pp. 135–46.

[101] Qing Chen, Johan Jeppsson, and John Ågren: *Acta Mater.*, 2008, vol. 56, pp. 1890–96.

[102] R. Rettig and R. F. Singer: *Acta Mater.*, 2011, vol. 59, pp. 317–27.

[103] Luc Rougier, Alain Jacot, Charles Andre Gandin, Paolo Di Napoli, Pierre Yvan Thery, Damien Ponsen, and Virginie Jaquet: *Acta Mater.*, 2013, vol. 61, pp. 6396–6405.

[104] Long-Qing Chen: *Annu. Rev. Mater. Res.*, 2002, vol. 32, pp. 113–40.

[105] Guomin Han, Zhiqiang Han, Alan A Luo, Anil K Sachdev, and Baicheng Liu: *Scr. Mater.*, 2013, vol. 68, pp. 691–94.

[106] Y Gao, H Liu, R Shi, N Zhou, Z Xu, Y M Zhu, J F Nie, and Y Wang: *Acta Mater.*, 2012, vol. 60, pp. 4819–32.

[107] G Kresse and J Furthmüller: *Comput. Mater. Sci.*, 1996, vol. 6, pp. 15–50.

[108] E Vincent, C S Becquart, C Pareige, P Pareige, and C Domain: *J. Nucl. Mater.*, 2008, vol. 373, pp. 387–401.

[109] G. Sha and A. Cerezo: *Acta Mater.*, 2005, vol. 53, pp. 907–17.

[110] David Molnar, Rajdip Mukherjee, Abhik Choudhury, Alejandro Mora, Peter Binkele, Michael Selzer, Britta Nestler, and Siegfried Schmauder: *Acta Mater.*, 2012, vol. 60, pp. 6961–71.

[111] Z Szklarska-Smialowska: *Corros. Sci.*, 1999, vol. 41, pp. 1743–67.

[112] R. T. Foley: *Corrosion*, 1986, vol. 42, pp. 277–88.

[113] Monica Trueba and Stefano P. Trasatti: *Mater. Chem. Phys.*, 2010, vol. 121, pp. 523–33.

[114] L. Guan, Y. Zhou, B. Zhang, J. Q. Wang, E. H. Han, and W. Ke: *Corros. Sci.*, 2015, vol. 103, pp. 255–67.

[115] N. Birbilis and R. G. Buchheit: *J. Electrochem. Soc.*, 2005, vol. 152, p. B140.

[116] Shuangqing Sun, Shenghui Chen, Yunfei Ma, Qifei Zheng, and Songqing Hu: *Corrosion*, 2014, vol. 70, pp. 1064–73.

[117] Ren Yu Chen and Cheng Chyuan Lai: *J. Mar. Sci. Technol.*, 2014, vol. 22, pp. 450–

54.

[118] J. Seong, F. Yang, F. Scheltens, G. S. Frankel, and N. Sridhar: *J. Electrochem. Soc.*, 2015, vol. 162, pp. C209–18.

[119] Mary Lyn C Lim, Robert G Kelly, and John R Scully: *Corrosion*, 2015, vol. 72, pp. 198–220.

[120] N Birbilis, R Zhang, M L C Lim, R K Gupta, C H J Davies, S P Lynch, R G Kelly, and J R Scully: *Corrosion*, 2012, vol. 69, pp. 396–402.

[121] S. Jain, M. L C Lim, J. L. Hudson, and J. R. Scully: *Corros. Sci.*, 2012, vol. 59, pp. 136–47.

[122] D A Jones: *Principles and Prevention of Corrosion*, Prentice Hall, 1996.

[123] Cortney B Crane and Richard P Gangloff: *Corrosion*, 2015, vol. 72, pp. 221–41.

[124] M.K. Miller, K.F. Russell, K. Thompson, R. Alvis, and D.J. Larson: *Microsc. Microanal.*, 2007, vol. 13, pp. 428–36.

[125] George D. Wignall, Kenneth C. Littrell, William T. Heller, Yuri B. Melnichenko, Kathy M. Bailey, Gary W. Lynn, Dean A. Myles, Volker S. Urban, Michelle V. Buchanan, Douglas L. Selby, and Paul D. Butler: *J. Appl. Crystallogr.*, 2012, vol. 45, pp. 990–98.

[126] M. K. Miller and R. G. Forbes: *Mater. Charact.*, 2009, vol. 60, pp. 461–69.

[127] Michael Miller: *Microsc. Microanal.*, 2003, vol. 9, pp. 1558–59.

[128] JPK: *NanoWizard Series - User Manual*, 2012.

[129] G Binnig, C F Quate, and Ch. Gerber: *Phys. Rev. Lett.*, 1986, vol. 56, pp. 930–33.

[130] P Eaton and P West: *Atomic Force Microscopy*, OUP Oxford, 2010.

[131] P.D. Littlewood, T.B. Britton, and A.J. Wilkinson: *Acta Mater.*, 2011, vol. 59, pp. 6489–6500.

[132] Gaosong Yi, Yakun Zhu, Erik Sundberg, Alexander T Derrick, and Michael L Free: *Corrosion*, 2015, vol. 72, pp. 177–86.

[133] Gaosong Yi, David A Cullen, Alexander T Derrick, Yakun Zhu, and Michael L Free: in *TMS Light Met.*, Minerals, Metals and Materials Society, 2015, pp. 361–65.

[134] Olaf Engler, Zhenshan Liu, and Katrin Kuhnke: *J. Alloys Compd.*, 2013, vol. 560, pp. 111–22.

[135] I. Nikulin, A. Kipelova, S. Malopheyev, and R. Kaibyshev: *Acta Mater.*, 2012,

vol. 60, pp. 487–97.

[136] Y Birol and F Sertcelik: *Zeitschrift Fuer Met. Res. Adv. Tech.*, 1999, vol. 90, pp. 329–34.

[137] Gaosong Yi, Michael L. Free, Yakun Zhu, and Alexander T. Derrick: in *Metall. Mater. Trans. A Phys. Metall. Mater. Sci.*, 2014, vol. 45, pp. 4851–4862.

[138] Fang Li, Dan Xiang, Yexian Qin, Robert B Pond Jr., and Kyle Slusarski: *Ultrasonics*, 2011, vol. 51, pp. 561–70.

[139] M. Kubota and B.C. Muddle: *Mater. Trans.*, 2005, vol. 46, pp. 2968–2974.

[140] D Blavette, E Cadel, A Fraczkiewicz, and A Menand: *Science (80-.).*, 1999, vol. 286, pp. 2317–19.

[141] Gaosong Yi, Alexander T. Derrick, Yakun Zhu, and Michael L. Free: *Metall. Mater. Trans. A Phys. Metall. Mater. Sci.*, 2015, vol. 46, pp. 5393–5406.

[142] Katharina Teichmann, Calin D Marioara, Sigmund J Andersen, and Knut Marthinsen: *Mater. Charact.*, 2013, vol. 75, pp. 1–7.

[143] T. Hu, K. Ma, T.D. Topping, J.M. Schoenung, and E.J. Lavernia: *Acta Mater.*, 2013, vol. 61, pp. 2163–78.

[144] Varley F Sears: *Neutron News*, 1992, vol. 3, pp. 26–37.

[145] S K Sinha, E B Sirota, S Garoff, and H B Stanley: *Phys. Rev. B*, 1988, vol. 38, pp. 2297–2311.

[146] Michel Perez: *Scr. Mater.*, 2005, vol. 52, pp. 709–12.

[147] N Saunders and A P Miodownik: *CALPHAD (Calculation of Phase Diagrams): A Comprehensive Guide*, Elsevier Science, 1998.

[148] P Liang, H L Su, P Donnadieu, M G Harmelin, A Quivy, P Ochin, G Effenberg, H J Seifert, H L Lukas, and F Aldinger: *Zeitschrift Fur Met.*, 1998, vol. 89, pp. 536–40.

[149] Yu Zhong, Mei Yang, and Zikui Liu: *Calphad*, 2005, vol. 29, pp. 303–11.

[150] Erwin Povoden-Karadeniz, Peter Lang, Piotr Warczok, Ahmad Falahati, Wu Jun, and Ernst Kozeschnik: *Calphad*, 2013, vol. 43, pp. 94–104.

[151] B Sonderegger and E Kozeschnik: *Metall. Mater. Trans. A*, 2009, vol. 40, pp. 499–510.

[152] E Kozeschnik, J Svoboda, R Radis, and F D Fischer: *Model. Simul. Mater. Sci. Eng.*, 2009, vol. 18, p. 15011.

[153] J Gilbert Kaufman and a S M International: *Introduction to Aluminum Alloys and Tempers*, 2000.

[154] Marc Legros, Gerhard Dehm, Eduard Arzt, and T John Balk: *Science (80-.).*, 2008, vol. 319, pp. 1646–49.

[155] E.W. Hart: *Acta Metall.*, 1957, vol. 5, p. 597.

[156] R.C. Picu and D. Zhang: *Acta Mater.*, 2004, vol. 52, pp. 161–71.

[157] I N A Oguocha, O J Adigun, and S Yannacopoulos: *J. Mater. Sci.*, 2008, vol. 43, pp. 4208–14.

[158] Soon Gu Kwon, Galyna Krylova, Patrick J Phillips, Robert F Klie, Soma Chattopadhyay, Tomohiro Shibata, Emilio E Bunel, Yuzi Liu, Vitali B Prakapenka, Byeongdu Lee, and Elena V Shevchenko: *Nat Mater*, 2015, vol. 14, pp. 215–23.

[159] H Yildirim Erbil and R Alsan Meric: *J. Phys. Chem. B*, 1997, vol. 101, pp. 6867–73.

[160] H I Aaronson, K R Kinsman, and K C Russell: *Scr. Metall.*, 1970, vol. 4, pp. 101–6.

[161] F Perrard, A Deschamps, and P Maugis: *Acta Mater.*, 2007, vol. 55, pp. 1255–66.

[162] Gabriel M Novotny and Alan J Ardell: *Mater. Sci. Eng. A*, 2001, vol. 318, pp. 144–54.

[163] J. D. Robson: *Acta Mater.*, 2004, vol. 52, pp. 4669–76.

[164] P Gas, D L Beke, and J Bernardino: *Philos. Mag. Lett.*, 1992, vol. 65, pp. 133–39.

[165] Y Mishin and Chr. Herzig: *Mater. Sci. Eng. A*, 1999, vol. 260, pp. 55–71.

[166] Philippe Maugis and Mohamed Gouné: *Acta Mater.*, 2005, vol. 53, pp. 3359–67.

[167] Y Zhang, B Milkereit, O Kessler, C Schick, and P A Rometsch: *J. Alloys Compd.*, 2014, vol. 584, pp. 581–89.

[168] L K Berg, J Gjønnes, V Hansen, X Z Li, M Knutson-Wedel, G Waterloo, D Schryvers, and L R Wallenberg: *Acta Mater.*, 2001, vol. 49, pp. 3443–51.

[169] M Dixit, R S Mishra, and K K Sankaran: *Mater. Sci. Eng. A*, 2008, vol. 478, pp. 163–72.

[170] Yunlai Deng, Yunya Zhang, Li Wan, and Xinming Zhang: *Mater. Sci. Eng. A*, 2012, vol. 554, pp. 33–40.

[171] N Kamp, A Sullivan, and J D Robson: *Mater. Sci. Eng. A*, 2007, vol. 466, pp. 246–

55.

[172] Adrian Luis Garcia-Garcia, Ivan Dominguez-Lopez, Luis Lopez-Jimenez, and J D Oscar Barceinas-Sanchez: *Mater. Charact.*, 2014, vol. 87, pp. 116–24.

[173] M de Hass and J.Th.M. De Hosson: *Scr. Mater.*, 2001, vol. 44, pp. 281–86.

[174] J M Chaix, N Eustathopoulos, and C H Allibert: *Acta Metall.*, 1986, vol. 34, pp. 1589–92.

[175] Jianjun Yao, Y.-W. Cui, Huashan Liu, Hongchao Kou, Jinshan Li, and Lian Zhou: *Calphad*, 2008, vol. 32, pp. 602–7.

[176] Yong Du, Y A Chang, Baiyun Huang, Weiping Gong, Zhanpeng Jin, Honghui Xu, Zhaohui Yuan, Yong Liu, Yuehui He, and F.-Y Xie: *Mater. Sci. Eng. A*, 2003, vol. 363, pp. 140–51.

[177] M Mantina, Y Wang, L Q Chen, Z K Liu, and C Wolverton: *Acta Mater.*, 2009, vol. 57, pp. 4102–8.

[178] Gaosong Yi, Kenneth C Littrell, Jonathan D Poplawsky, David A Cullen, Erik Sundberg, and Michael L Free: *Mater. Des.*, 2017, vol. 118, pp. 22-35.

[179] M L C Lim, J R Scully, and R G Kelly: *Corrosion*, 2012, vol. 69, pp. 35–47.

[180] M A Steiner and S R Agnew: *Corrosion*, 2015, vol. 72, pp. 169–76.

[181] M A Steiner and S R Agnew: *Scr. Mater.*, 2015, vol. 102, pp. 55–58.

[182] Alexander Derrick: *A Predictive Model of Mass Loss in Sensitized 5xxx Aluminum Alloys*, 2016.

[183] Gaosong Yi, David A Cullen, Kenneth C Littrell, et al.: *Metall. Mater. Trans. A*, 2017, doi:10.1007/s11661-017-3992-2.

[184] Michael Schütze; Dietrich Wieser; Roman Bender; Deutsche Gesellschaft für chemisches Apparatewesen: *Corrosion Resistance of Aluminium and Aluminium Alloys : Corrosive Agents and Their Interaction with Aluminium and Ist [I.e. Its] Alloys*, Frankfurt (Main), Germany : [Wiley-VCH for] DECHEMA, 2010.

[185] E Sikora, X J Wei, and B A Shaw: *Corrosion*, 2004, vol. 60, pp. 387–98.

[186] E Kus, Z Lee, S Nutt, and F Mansfeld: *Corrosion*, 2006, vol. 62, pp. 152–61.

[187] A.T. Dinsdale: *Calphad*, 1991, vol. 15, pp. 317–425.

[188] A. Kusoffsky, N. Dupin, and B. Sundman: *Calphad*, 2001, vol. 25, pp. 549–65.